

ABSTRACT

Title of dissertation: STRUCTURAL CHANGES AND THE NATURE OF SUPERCONDUCTIVITY IN RARE-EARTH DOPED CaFe_2As_2

Tyler Drye
Doctor of Philosophy
Chemical Physics
2014

Dissertation directed by: Professor Johnpierre Paglione
Department of Physics
Center for Nanophysics and
Advanced Materials

Chemical substitution into iron-pnictide parent compounds (*e.g.* AFe_2As_2 where $\text{A}=\text{Ba}$, Sr , or Ca) has proven to be an effective means to induce bulk high-temperature superconductivity in these systems. By doping CaFe_2As_2 with rare-earth lanthanides (La , Ce , Pr , and Nd), we have observed a 47 K superconducting phase coexisting with a lattice distorting “collapse” transition. Both of these effects have important ramifications: the collapse transition occurs when interlayer As atoms form a bond, shrinking the c -axis lattice constant and simultaneously quenching the iron magnetic moment. This transition is further explored in context of a similar system, Sr-doped BaNi_2As_2 . The superconducting phase, given the right combination of conditions, appears with a critical temperature as high as 49 K, but always in a very small volume of the sample (as determined by shielding effects). This has led to interesting theories about the nature of this superconductivity. A recently posited idea of “interfacial superconductivity” has been ruled out by our tests. Additionally, increasing the concentration of rare-earth atoms does not increase the superconducting volume fraction, but, in fact lowers the transition temperature, excluding the hypothesis that rare-earth defects are responsible for the minority superconducting phase. New pressure measurements have shown that the superconducting phase is stabilized when antiferromagnetic order is fully suppressed.

STRUCTURAL CHANGES AND THE NATURE OF
SUPERCONDUCTIVITY IN RARE-EARTH DOPED CaFe_2As_2

by

Tyler Drye

Dissertation submitted to the Faculty of the Graduate School of the
University of Maryland, College Park in partial fulfillment
of the requirements for the degree of
Doctor of Philosophy
2014

Advisory Committee:
Professor Johnpierre Paglione (chair)
Professor Richard Greene
Professor Steven Anlage
Professor Efrain Rodriguez
Professor Bryan Eichhorn
Professor Ichiro Takeuchi

© Copyright by
Tyler Drye
2014

Dedication

To JP for letting me be wrong and helping me be right, to Zulya for always encouraging me, and to my family for their constant support.

Acknowledgments

Science is no longer done by individuals secluded in basements; it is a collaborative effort that requires many people working together. Good science requires people critiquing your arguments and looking for faults in your logic. The following work was done over a five year period with the help of many great people. I would like to acknowledge these contributions, without which this work would never have been completed:

I would first like to thank my advisor, Johnpierre Paglione, for giving me the opportunity to pursue both research and coursework that fit my vision for my education; this freedom was the principal reason I chose Maryland, and I will always appreciate JP allowing me to develop my own strengths as a researcher. He has always entertained whatever crazy theories I had on our work and allowed me to pursue a range of projects.

I would also like to thank the former post-docs in our group, Shanta Saha and Nicholas Butch, who helped refine my abilities and acquaint me with the methodology of the group. I would also like to acknowledge the work of collaborators like Peter Zavalij from the Chemistry department and Jeffrey Lynn at NIST, whose expertises in X-ray and neutron diffraction, respectively, were paramount to many of the successes of my research.

In addition, the groups of Rick Greene and Ichiro Takeuchi have been amazing in keeping our equipment running, even when I have tried my best to break it. Numerous post-docs, including Kui Jin, Xiaohang Zhang, Rongwei Hu, Xiangfeng

Zhang, Jie Yong, and Yasuyuki Nakajima have kept the laboratory running so that I could continue working. To that end, I would also like to express my appreciation of the CNAM technical staff: Doug Benson and Brian Straughn, who taught me how to fix nearly everything you could think of breaking.

I was also fortunate enough to visit other laboratories in pursuit of this work, and I would like to thank those collaborators as well. Visiting the group of Paul Canfield, at Ames Laboratory, was very important to my growth as a scientist, and the work of Valentin Taufour was invaluable to the pressure growth experiments at the end of this thesis. And although the relevant work is not presented here, I would like to thank Tatsuya Yanagisawa and Hiroshi Amitsuka for hosting me at Hokkaido University.

I would also like to thank our former student, Kevin Kirshenbaum, for his leadership and support during my early years in the Paglione group. I have been very fortunate to share the laboratory with an excellent group of fellow students: Steve Ziemak, Paul Syers, Richard Suchoski, Renxiong Wang, Connor Roncioli, and Christopher Eckberg have been supportive co-workers and good friends during my time at Maryland. It has been my privilege to enjoy work because of the people I see everyday. I have also been lucky to have the assistance of several talented undergraduate students who have made my work easier and made me a better teacher: Jeffrey Magill, Uneeb Qureshi, and Alex Hughes.

Finally, I would like to thank my family; without them I would have never made to the finish line. I have been fortunate to have a lot of people who care about me and support me, starting with my parents, Charles and Lynne Drye, who have

supported me in all my efforts. I would also like to thank Nancy Drye for getting me interested in science as a child and pushing me to learn about the world around me. In addition, my brothers, Andrew and Joseph, have always built me up and made me believe in myself, while keeping me grounded and humble (or as close as possible). Last, but not least, I have an excellent group of friends that have pushed me to work hard, if for no other reason than to be able to brag that I graduated first.

Foreword

Much of the work presented in this thesis has been published, and thus portions of this thesis are represented in the following published works:

S.R. Saha, N.P. Butch, T. Drye, J. Magill, S. Ziemak, K. Kirshenbaum, P. Y. Zavalij, J. W. Lynn, and J. Paglione, “Structural collapse and superconductivity in rare-earth-doped CaFe_2As_2 .” *Physical Review B* **85**, 024525 (2012) (Ref. [1]).

M. Long, J. Gao-Feng, D. Jia, S.R. Saha, T. Drye, J. Paglione, and Y. Wei-Qiang, “Quenched Fe moment in the collapsed tetragonal phase of $\text{Ca}_{1-x}\text{Pr}_x\text{Fe}_2\text{As}_2$.” *Chinese Physics B* **22** 057401 (2013) (Ref. [2]).

S.R. Saha, T. Drye, S.K. Goh, L.E. Klintberg, J.M. Silver, F.M. Grosche, M. Sutherland, T.J.S. Munsie, G.M. Luke, D.K. Pratt, J.W. Lynn, and J. Paglione, “Segregation of antiferromagnetism and high-temperature superconductivity in $\text{Ca}_{1-x}\text{La}_x\text{Fe}_2\text{As}_2$.” *Physical Review B* **89** 134516 (2014) (Ref. [3])

T.B. Drye, S.R. Saha, J. Paglione, and P.Y. Zavalij, “Rare earth substitution in lattice-tuned $\text{Sr}_{0.3}\text{Ca}_{0.7}\text{Fe}_2\text{As}_2$ solid solutions.” *Superconductor Science and Technology* **25** 084014 (2012) (Ref. [4]).

T. Drye, S.R. Saha, P.Y. Zavalij, and J. Paglione, “Chemical pressure effect and superconductivity in $\text{Ba}_{1-x}\text{Sr}_x\text{Ni}_2\text{As}_2$ solid solutions.” (Pre-print)

T. Drye, V. Taufour, U. Kaluarachchi, S. Ran, P. Canfield, and J. Paglione, “High pressure synthesis and properties of $(\text{Ca},\text{Pr})\text{Fe}_2\text{As}_2$.” (Pre-print)

T. Dye and J. Paglione, “Current-dependent tests of interfacial superconductivity in $\text{Ca}_{1-x}\text{R}_x\text{Fe}_2\text{As}_2$.” (Pre-print)

Table of Contents

List of Figures	x
List of Abbreviations	xii
1 Background	1
1.1 Superconductivity	1
1.2 Iron Pnictide Superconductors	13
1.3 Furthering the Iron-pnictices	20
1.3.1 Chemical Comparison	21
1.3.2 Physics	22
1.3.3 New Materials and Investigations	23
2 Experimental Methods	25
2.1 Single Crystal Growth	25
2.1.1 Molten Metal Flux Method	26
2.1.2 Self Flux Method	27
2.1.3 Thermal Treatments	28
2.2 Chemical and Structural Characterization	30
2.2.1 Energy-dispersive and Wavelength-dispersive X-ray Spectroscopy	30
2.2.2 X-ray Crystallography	31
2.3 Physical Properties Characterization	33
2.3.1 Electronic Transport Measurements	33
2.3.2 Magnetic Susceptibility	38
2.3.3 Heat Capacity	40
3 Structural Collapse and Superconductivity in Rare-Earth doped CaFe_2As_2	43
3.1 Methods	46
3.2 Chemical and Structural Characterization	46
3.2.1 X-ray Diffraction Analysis	47
3.2.2 Neutron Diffraction Data	49
3.3 The Collapsed Tetragonal State	53
3.3.1 Origin and Occurrence	53
3.3.2 Consequences of the Collapsed-Tetragonal Transition	57
3.4 Superconducting Phase	61
3.4.1 Electrical Transport and Magnetic Susceptibility	62
3.4.2 Evidence of Intrinsic SC	67
3.5 Phase Diagram and Discussion	73
4 Enhanced Superconducting Transition Temperature in $(\text{Ba,Sr})\text{Ni}_2\text{As}_2$ Solid Solutions	79
4.1 Methods	80
4.2 Chemical and Structural Properties	81
4.3 Physical Properties	83

4.3.1	Electrical Transport and Magnetic Susceptibility	83
4.4	Summary	87
5	Rare earth substitution in lattice-tuned $\text{Sr}_{0.3}\text{Ca}_{0.7}\text{Fe}_2\text{As}_2$ solid solutions	90
5.1	Methods	91
5.2	Chemical and Structural Properties	92
5.3	Transport and Magnetization	95
5.4	Summary and Phase Diagram	98
6	High-Pressure Synthesis and Characterization of Pr-doped CaFe_2As_2	101
6.1	Methods	102
6.2	Chemical and Structural Characterization and Annealing Effects . . .	103
6.3	Superconductivity	106
6.4	The Collapse Transition	110
6.5	Extended Phase Diagram and Discussion	113
7	Current-dependent tests of Interfacial Superconductivity in $\text{Ca}_{1-x}\text{R}_x\text{Fe}_2\text{As}_2$	116
7.1	Methods	117
7.2	$\text{Ca}_{1-x}\text{Pr}_x\text{Fe}_2\text{As}_2$	119
7.3	$\text{Ca}_{1-x}\text{La}_x\text{Fe}_2\text{As}_2$	125
7.4	Summary	126
8	Summary and Outlook	129
8.1	Summary	129
8.2	Theoretical Work	132
8.3	Outlook and Further Work	134
A	Summary of Compounds	136

List of Figures

1.1	Basic Properties of Superconductors	2
1.2	Maximum T_c Through the Years	4
1.3	Superconducting Pairing Symmetries	8
1.4	H_{c2} behaviors of conventional and unconventional superconductors	9
1.5	Prototypical crystal structure of the cuprate materials—YBCO	11
1.6	Generic transition temperature vs. doping phase diagram for cuprate superconductors	12
1.7	The five different families of iron-pnictide superconductors, showing the active FeAs planes	14
1.8	Electron and magnetic schemes of the iron-based superconductors	16
1.9	Generic pressure and doping phase diagrams of iron-pnictide superconductors	19
1.10	Possible Fermi surfaces and pairing schemes in iron-based superconductors	20
2.1	General growth cycle for iron-122 materials and pictures of single crystals	29
2.2	X-ray diffraction pattern of CaFe_2As_2	32
2.3	Wire configurations for resistance measurements	35
2.4	Susceptibility of superconducting compound with a T_c of 25 K.	39
2.5	Specific heat capacity of the Co-doped BaFe_2As_2 series	42
3.1	Nominal vs. actual concentrations of dopants in $\text{Ca}_{1-x}\text{R}_x\text{Fe}_2\text{As}_2$	47
3.2	Lattice parameters vs. rare earth concentration for $\text{Ca}_{1-x}\text{R}_x\text{Fe}_2\text{As}_2$	48
3.3	Raw Neutron Diffraction data for Nd-doped CaFe_2As_2	49
3.4	Neutron diffraction contour plots of $\text{Ca}_{1-x}\text{R}_x\text{Fe}_2\text{As}_2$ lattice parameters	50
3.5	Summary of Diffraction data and unit cell parameters for $\text{Ca}_{1-x}\text{R}_x\text{Fe}_2\text{As}_2$	51
3.6	Effect of the collapse transition on the structure of $\text{Ca}_{1-x}\text{R}_x\text{Fe}_2\text{As}_2$	54
3.7	Pressure-induced collapse transition in $\text{Ca}_{1-x}\text{R}_x\text{Fe}_2\text{As}_2$	56
3.8	^{75}As NMR spectra vs frequency for collapsed-tetragonal $\text{Ca}_{1-x}\text{R}_x\text{Fe}_2\text{As}_2$ crystals.	58
3.9	NMR Central peak and Knight shifts of $\text{Ca}_{1-x}\text{R}_x\text{Fe}_2\text{As}_2$ crystals.	60
3.10	Resistivity and Susceptibility of $\text{Ca}_{1-x}\text{R}_x\text{Fe}_2\text{As}_2$ single crystals.	63
3.11	Hall effect through the collapse transition in $\text{Ca}_{1-x}\text{R}_x\text{Fe}_2\text{As}_2$	64
3.12	Summary of superconductivity in the $\text{Ca}_{1-x}\text{R}_x\text{Fe}_2\text{As}_2$ system	65
3.13	Effect of Annealing on SC in $\text{Ca}_{1-x}\text{R}_x\text{Fe}_2\text{As}_2$ crystals	70
3.14	Effect of surface oxidation on SC in $\text{Ca}_{1-x}\text{R}_x\text{Fe}_2\text{As}_2$ crystals	71
3.15	Full Phase Diagram of the $\text{Ca}_{1-x}\text{R}_x\text{Fe}_2\text{As}_2$ system	74
4.1	Chemical Composition of $\text{Ba}_{1-x}\text{Sr}_x\text{Ni}_2\text{As}_2$ single crystals	82
4.2	C -axis lattice parameters of $\text{Ba}_{1-x}\text{Sr}_x\text{Ni}_2\text{As}_2$ single crystals	84
4.3	Electrical transport in $\text{Ba}_{1-x}\text{Sr}_x\text{Ni}_2\text{As}_2$ single crystals	86

4.4	Superconducting Characteristics of $\text{Ba}_{1-x}\text{Sr}_x\text{Ni}_2\text{As}_2$ single crystals . . .	87
4.5	Phase diagram of the $\text{Ba}_{1-x}\text{Sr}_x\text{Ni}_2\text{As}_2$ system	88
5.1	EDS analysis of $(\text{Sr}_{1-y}\text{Ca}_y)_{1-x}\text{La}_x\text{Fe}_2\text{As}_2$ single crystals	93
5.2	Unit cell parameters of $(\text{Sr}_{1-y}\text{Ca}_y)_{1-x}\text{La}_x\text{Fe}_2\text{As}_2$ single crystals	94
5.3	Resistivity measurements of $(\text{Sr}_{1-y}\text{Ca}_y)_{1-x}\text{La}_x\text{Fe}_2\text{As}_2$ single crystals . . .	95
5.4	Magnetic Susceptibility of $(\text{Sr}_{1-y}\text{Ca}_y)_{1-x}\text{La}_x\text{Fe}_2\text{As}_2$ single crystals . . .	97
5.5	Phase Diagram of the $(\text{Sr}_{1-y}\text{Ca}_y)_{1-x}\text{La}_x\text{Fe}_2\text{As}_2$ system	99
6.1	C -axis vs Pr concentration for $\text{Ca}_{1-x}\text{Pr}_x\text{Fe}_2\text{As}_2$ crystals grown under high pressure	105
6.2	Resistivity data of $\text{Ca}_{1-x}\text{Pr}_x\text{Fe}_2\text{As}_2$ grown under high pressure	107
6.3	Low temperature resistivity data on $\text{Ca}_{1-x}\text{Pr}_x\text{Fe}_2\text{As}_2$ crystals grown under high pressure	108
6.4	H_{c2} of a $\text{Pr}_{0.3}\text{Ca}_{0.7}\text{Fe}_2\text{As}_2$ crystal grown under high pressure	109
6.5	High field magnetization data on $\text{Ca}_{1-x}\text{Pr}_x\text{Fe}_2\text{As}_2$ crystals grown under high pressure	111
6.6	Hall Effect of $\text{Ca}_{1-x}\text{Pr}_x\text{Fe}_2\text{As}_2$ crystals grown under high pressure . . .	112
6.7	Phase diagram over the full range of Pr doping is $\text{Ca}_{1-x}\text{Pr}_x\text{Fe}_2\text{As}_2$. . .	114
7.1	Resistivity behavior of $\text{NdFeAsO}_{0.88}\text{F}_{0.12}$	118
7.2	R vs. $1/T$ for $\text{Pr}_{0.15}\text{Ca}_{0.85}\text{Fe}_2\text{As}_2$	120
7.3	Excitation Current vs. T^* for $\text{Ca}_{1-x}\text{Pr}_x\text{Fe}_2\text{As}_2$ samples	122
7.4	Normalized Current vs. Reduced Temperature for $\text{Ca}_{1-x}\text{Pr}_x\text{Fe}_2\text{As}_2$ samples	123
7.5	V-I characteristics of $\text{Ca}_{1-x}\text{Pr}_x\text{Fe}_2\text{As}_2$ materials	124
7.6	R vs. $1/T$ for $\text{Ca}_{1-x}\text{La}_x\text{Fe}_2\text{As}_2$ samples	126
7.7	Normalized Current vs. Reduced T for $\text{Ca}_{1-x}\text{La}_x\text{Fe}_2\text{As}_2$ crystals . . .	127

List of Abbreviations

CNAM	Center for Nanophysics and Advanced Materials
FeSC	Iron-based superconductor
TM	Transition metal
T_c	Superconducting transition temperature
T_N	Neél temperature
AFM	Antiferromagnetism
122	Materials with the chemical formula AT_2As_2 (A = Ca, etc. T=Fe,etc.)
EDS	Energy dispersive x-ray spectroscopy (also called EDX)
WDS	Wavelength dispersive x-ray spectroscopy (also called WDX)
k_b	The Boltzmann constant

Chapter 1

Background

1.1 Superconductivity

In 1911, Heike Kamerlingh Onnes published a paper reporting a sudden drop in the electrical resistivity of mercury at 4.2 Kelvin. Between 1911 and the 1950s, this phenomenon, dubbed “Superconductivity” by Onnes, would be discovered in a host of materials once they were cooled to extremely low temperatures [5, 6]. Superconductivity has since been defined as a state of matter in which the resistivity of a material drops to exactly zero and the material begins to show diamagnetic behavior, as shown in Figure 1.1. This behavior arises at a critical transition temperature (T_c) and defines the ground state of these materials. In 1956, the BCS theory of superconductivity (named for John Bardeen, Bob Schrieffer, and Leon Cooper) was published, presenting a microscopic theoretical model for superconductors [7]. More recently, new superconductors with extremely high critical temperatures have been discovered, renewing interest in superconductor research.

Following the success of the BCS theory in explaining the behavior of the known superconductors at the time, it was assumed that physicists had gained a firm grasp on understanding superconductivity. But, in 1986, Johannes Bednorz and Karl Müller discovered a new type of superconductor: a Ba-La-Cu-O system with a T_c of 35 K [9]. A flurry of work followed, with published critical temperatures as

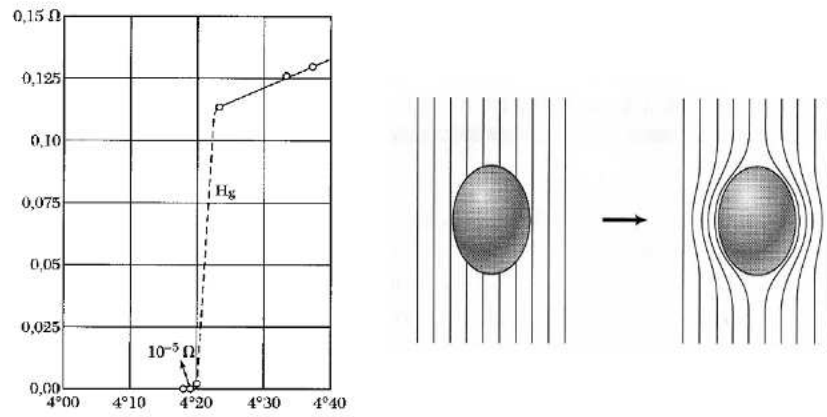


Figure 1.1: **(Left)** Onnes' original findings upon measuring the resistivity of Hg, with an abrupt drop to zero at 4.2 K. **(Right)** Diagram of the Meissner effect with magnetic field lines indicated. Upon cooling below T_c , all magnetic field lines are expelled from the material. Taken from ref. [8]

high as 138 K [10]. Figure 1.2 shows a graph of the highest known T_c as a function of the year of discovery [11]. However, these newly discovered superconductors (nicknamed the cuprates, because they all involve copper-oxygen bonds) were found to have properties which made experiments difficult, as will be discussed later in detail. More importantly, it was found that these new superconductors did not follow the predictions of BCS theory. These cuprates defined a new class of unconventional high-temperature superconductors; materials of this class will be discussed in this paper.

Conventional Superconductivity

Before discussing the behavior of unconventional superconductors, it is important to establish the behavior of conventional superconductors. From there, we can then examine how the unconventional superconductors differ from this expected behavior. BCS theory explains conventional superconductors as normal metals with a Fermi Sphere of electron energy levels in momentum space (or k -space). As the metal is cooled, the electrons begin to interact more strongly with the vibrations of the crystal lattice. These lattice vibrations are able to cause an attractive potential to form between electrons, which normally repel each other due to the Coulomb interaction. According to the theory, any net attractive interaction between electrons will result in pairing between the electrons—that is to say that the electrons will pair up into Cooper pairs as a result of phonon interactions.

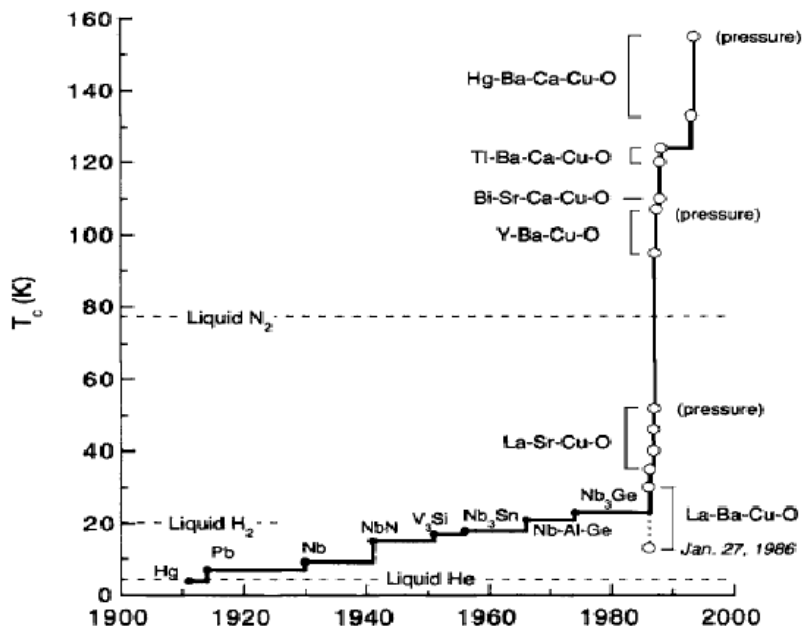


Figure 1.2: Highest recorded superconducting transition temperature by year. Tl-Ba-Ca-Cu-O is the highest recorded T_c under ambient pressure conditions, while the Hg-Ba-Ca-Cu-O system achieves the highest known T_c of 153 K at a pressure of 150 kbar [12]. Taken from ref. [11]

This pairing leads to the formation of a lower energy state, a Bose condensate state, leading to an energy gap opening between the paired state and the non-paired electron states so that

$$\Delta(0) = 1.76 \cdot k_b \cdot T_c \tag{1.1}$$

where Δ is the energy difference between the states at zero temperature [13]. According to BCS theory, this energy gap will be perfectly isotropic as a function of momentum, so that the superconducting order parameter is constant (known as *s*-wave pairing symmetry). [14]

According to BCS theory, the magnetic properties of a conventional superconductor can be explained by the presence of supercurrents of Cooper pairs, which are able to instantaneously respond to and oppose an applied magnetic field, resulting in perfect diamagnetism—displaying a negative magnetic susceptibility in an applied magnetic field (known as the Meissner Effect) [15, 16]. The phenomenological Ginzburg-Landau and London equations were the first equations to describe the intricacies of this complex behavior, providing two experimentally measurable quantities: the coherence length (ζ), which determines the characteristic length scale for paired electrons, and the London penetration depth (λ), which measures the distance that a magnetic field is able to penetrate into a superconducting material. For BCS superconductors, the values of ζ and λ under an applied magnetic field will determine the type (I or II) of the superconductor [17].

Under a large enough applied field, called the critical field (H_c), the superconductor will be forced into its normal state via either the Pauli pair-breaking effect or the orbital effect. The Pauli effect is rather straight-forward and involves breaking the Cooper pairs by overcoming the superconducting energy gap with Zeeman energy. The orbital effect, on the other hand, involves penetration of the applied field into the superconductor by overcoming the supercurrent, which results in two different behaviors: Type I superconductors return to the normal state at a critical field H_c . Type II superconductors show increasing diamagnetism up to a certain critical field H_{c1} , at which point the diamagnetism decays until a second critical field, H_{c2} . At H_{c2} , the type II superconductor returns fully to the normal state [18].

Unconventional Superconductivity

BCS theory explains superconductivity by invoking the idea of Cooper pairs created via an electron-phonon interaction and the creation of a phase-coherent state to explain the observed properties of superconductors [19]. However, there is also a large category of materials for which there is increasing evidence that the electron-phonon pairing mechanism does not explain everything [20]; these materials are referred to as unconventional superconductors [21]. While the pairing mechanism for these materials remains unknown, they do exhibit many of the properties of BCS superconductors: Cooper pairs, zero resistivity, T_c , and Type II behavior. Thus, it is generally agreed that it is not the nature of the superconductivity that difference but rather the underlying pairing interaction[22].

More precisely, we can define unconventional superconductors as those which break an additional symmetry (above the usual gauge symmetry breaking) at the

phase transition; typically, this broken symmetry is represented as a change in the order parameter $[\Delta]$ of the wave function. The superconducting wave-function can be approximated as

$$\Psi = A \cdot e^{i\phi} \tag{1.2}$$

where A is an amplitude related to the energy gap Δ , and ϕ represents a phase [14]. In the case of s -wave pairing (see Figure 1.3a), A and ϕ remain constant in momentum space. However, any other pairing symmetry requires that both A and ϕ vary; specifically, the energy gap will develop nodes where it decreases to zero. The presence of these nodes forces a sign change in the superconducting phase at each node. Thus, the phase of the wave-function in the presence of nodes is depicted with “+” and “-” signs, showing the change of phase across the node. Figure 1.3b depicts a d -wave pairing symmetry in k -space.

The presence (or absence) of these nodes makes pairing an important detail when studying superconductors because the presence of nodes in the energy gap implies the presence of low energy quasiparticle states (phonons, electrons, holes, etc.) which are normally gapped out in an s -wave symmetry. Experiments such as thermal conductivity and tunneling spectroscopy, which can probe the presence of quasiparticle states, are thus able to provide information about the structure of the energy gap. [24]

In many unconventional superconductors, H_{c2} —the magnetic critical field where a superconductor is completely returned to the normal state—shows a strong up-

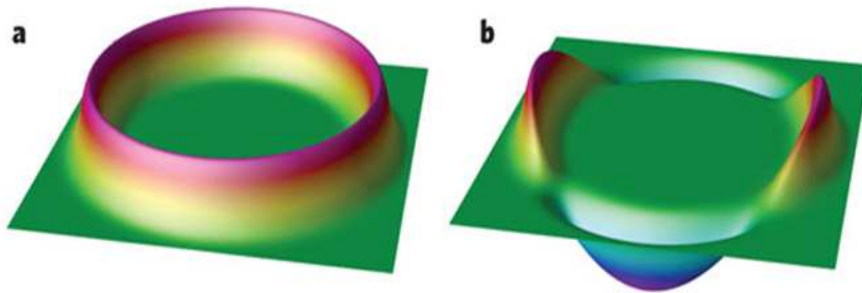


Figure 1.3: **Possible Superconducting Pairing Symmetries.** In these plots, the green plane represents the 2-dimensional k_x and k_y momentum space. The magnitude of the energy gap is plotted in the z-direction. **(a)** Momentum space representation of the energy gap for an *s*-wave superconductor. Both the amplitude and the phase of the gap remain constant in k -space. **(b)** Similar representation of a *d*-wave superconducting energy gap. The four points where the gap goes to zero are nodes, and the phase of the wave function changes sign going across those nodes. The “*d*” designation is in analogy with the shape of atomic *d*-orbitals, which show a similar shape. Taken from ref. [23]

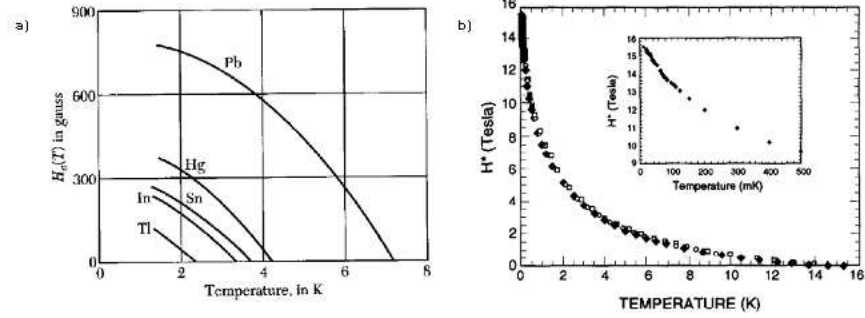


Figure 1.4: Comparison of H_{c2} behaviors of Type I conventional superconductors (a) [8], versus the behavior of an unconventional superconductor (b) [21].

wards curvature as temperature decreases towards 0 K (Figure 1.4). This is in stark contrast to the leveling-off of H_{c2} as T approaches 0 K in conventional superconductors [8]. This leads to an extremely high upper critical field value, which results in experimental difficulties when trying to achieve the normal state through the application of magnetic fields. For some superconductors, the upper critical field lies above the range of even the most powerful magnets available [21].

Often, unconventional superconductors (*i.e.* the cuprates and organic superconductors) also feature an unusually low carrier concentration. Conventional superconductors are typically metals with carrier concentrations on the order 10^{23}

carriers/cm³. However, unconventional superconductors may have carrier concentrations substantially below this number. [21]

Finally, the resistivity of unconventional superconductors shows a far more interesting range of behaviors than what is seen in conventional superconductors. Conventional superconductors, being metals, show simple, monotonically decreasing resistivity with decreasing temperatures to some residual value ρ_0 . However, unconventional superconductors tend to have much more anomalous normal state properties. They can show higher room temperature resistivities, closer to the semi-conducting range. Many families, such as the cuprates, show resistivity linearly decreasing with decreasing temperature, rather than the expected cubic behavior, while other families show metallic or poor metal behaviors. Complicated chemistries and strong electronic interactions are thought to be the basis for this behavior. [21]

Cuprates

Of the various unconventional superconductors, the most prominently studied group has been the cuprate family. While this is certainly justified due to their extremely high critical temperatures and unconventional behavior, understanding these materials has proven to be challenging over the last couple of decades. Attempts at establishing a theoretical understanding of this large category of materials, which features insulating parent compounds doped into a metallic state, antiferromagnetic ordering, and nearly two dimensional crystal structures, have so far been unsuccessful.

The cuprate superconductors are a class of materials based on layers of copper and oxygen (CuO₂) running through the material and separated by layers that

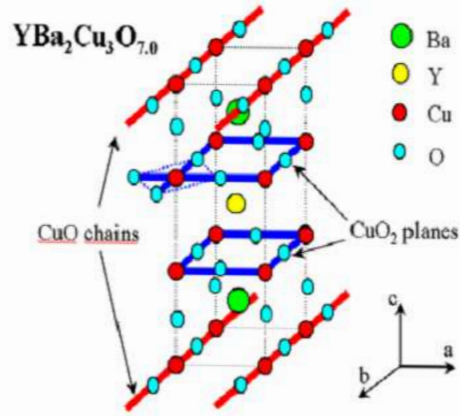


Figure 1.5: Crystal structure of YBCO. Taken from ref. [26]

donate charge (either electrons or holes) to the copper-oxide layers [Figure 1.5]. The spacer layers can range from single atoms (such as Ba and Y) to large molecular structures (such as in the perovskite structures), but their main function appears to always be to donate charge to the copper-oxide layers. In the CuO_2 layer, each copper atom bonds with four bridging oxygen atoms in a square planar arrangement. The result is that copper oxidizes to a +2 state, and each oxygen atom goes to a -2 state. This leaves the copper ion with a d^9 electron configuration. This leads to the Cu $d_{x^2-y^2}$ orbital and the O $2p_x$ and $2p_y$ orbitals becoming the most active orbitals for determining the electronic characteristics of the material [25].

The layers in between the CuO_2 layers play a crucial role in determining the behavior of these compounds. The CuO_2 layers are left with half-filled electron

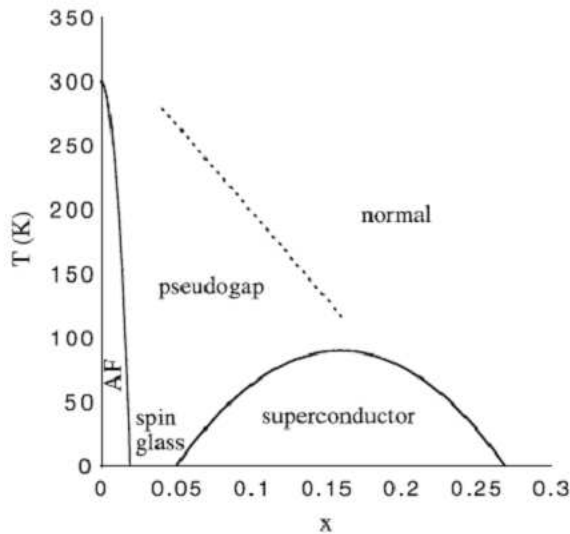


Figure 1.6: Generic cuprate phase diagram. Antiferromagnetism is suppressed and superconductivity appears as a result of increased charge doping [25].

bands from the Cu-O antibonding molecular orbitals, which should result in metallic behavior. Strong Coulomb interactions between electrons, however, result in a so-called “Mott insulating state with an energy gap of ~ 2 eV [27], which can then be doped toward a conducting state via charge donation from the buffer layers, leading to semiconducting or metallic behavior in the doped materials [28]. However, charge doping these materials turns out to play an even bigger role, by controlling the physics of the system. Figure 1.6 shows a typical cuprate phase diagram, illustrating the suppression of antiferromagnetic (AFM) order with increased charge doping and, eventually, the onset of superconductivity.

A striking difference between conventional superconductors and the cuprates is that these unconventional superconductors tend to show a very short coherence length. While measurements on conventional superconductors indicate typical coherence lengths on the scale of 1000 Å, cuprate superconductors show coherence lengths on the order of 100 times smaller. This suggests that the pairing mechanism responsible for this unconventional behavior acts on a much shorter scale than the scale set by phonon interactions. [21]

All together, the investigation of the cuprate family of superconductors represents work on at least twelve different subfamilies, which, when broken down by stoichiometry, encompass hundreds of different materials [24]. Unfortunately, after more than two decades of work, it is still not possible to draw definitive conclusions about the pairing mechanism and physical nature of the cuprates. Fortunately, a new family of superconductors, the iron pnictides, present another opportunity to study high- T_c superconductivity and, hopefully, to elucidate the nature of the high- T_c pairing mechanism.

1.2 Iron Pnictide Superconductors

Chemical and Magnetic Structure

The iron-arsenide superconductors can be separated into five different families based on their crystal structure (Figure 1.7). All of these families share the basic building blocks of layers of iron covalently bonded to either pnictide or chalcogenide atoms. The other elements in the chemical formula contribute to the spacing be-

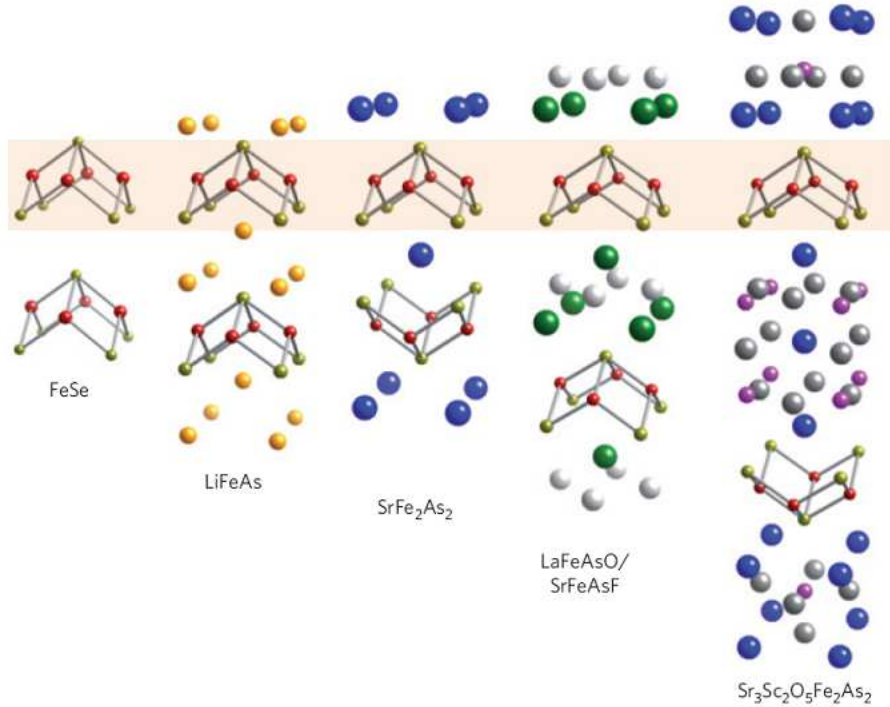


Figure 1.7: The five families of iron based superconductors. Each material consists of layers of iron and arsenic with different elements creating a spacer layer. Notice that the 122 and 32522 families are the only two to display inversion symmetry, due to the inverted second layer of Fe-As [24].

tween these iron layers, acting as charge donors; however, these spacer layers play an important role in determining the physics of the material. [24]

The true importance of the spacer layers is understood by looking at the chemistry of the iron ions. In each of these materials, iron is in a tetrahedral bonding environment, surrounded by four arsenic (or chalcogenide) atoms. Arsenic requires three electrons to reach a closed shell and satisfy its bonding. However, thanks to the charge donation from the spacer layers, which almost universally donate one electron per Fe-As unit, iron is only required to give up two of its valence electrons

to the arsenic atoms. This leaves iron with a d^6 metal electron configuration. In the iron-chalcogenides, the iron only gives up two electrons to the chalcogenide atoms, thus reaching the same configuration without requiring a charge-donor layer [29].

An important point in understanding the chemistry of these systems is in understanding their band structure; specifically, how the five iron d -orbitals split. The tetrahedral arrangement of (pnictide or chalcogenide) atoms about the iron causes splitting of the iron d -orbitals into a scheme with two degenerate orbitals for the ground state (Figure 1.8a). Here, the d^6 configuration becomes important because this leaves one electron and two unfilled states, meaning one electron sees two degenerate states which it can occupy. This is known as a “Jahn-Teller instability.

The Jahn-Teller instability requires a change in the unit cell (a tetragonal to orthorhombic distortion), which lifts the degeneracy from the e_g orbitals and leaves one orbital with a slightly lower energy. This may be the mechanism behind the emergence of antiferromagnetic ordering in these materials, although this is a question still under investigation (Figure 1.8b). All of the iron based superconductors show an antiferromagnetic ordering. Although the transition temperature into this ordering depends on the parent material (*e.g.* BaFe_2As_2 is the parent material of $\text{BaFe}_{2-x}\text{Co}_x\text{As}_2$), the trend of suppressing this ordering temperature is universal to these materials.

It is inconclusive at this point as to the specific nature of the antiferromagnetism that occurs in these materials. This arises from the idea that the magnetic interaction responsible for antiferromagnetic order likely plays a role in the pairing mechanism in these materials [24]. One possible scenario is that localized iron

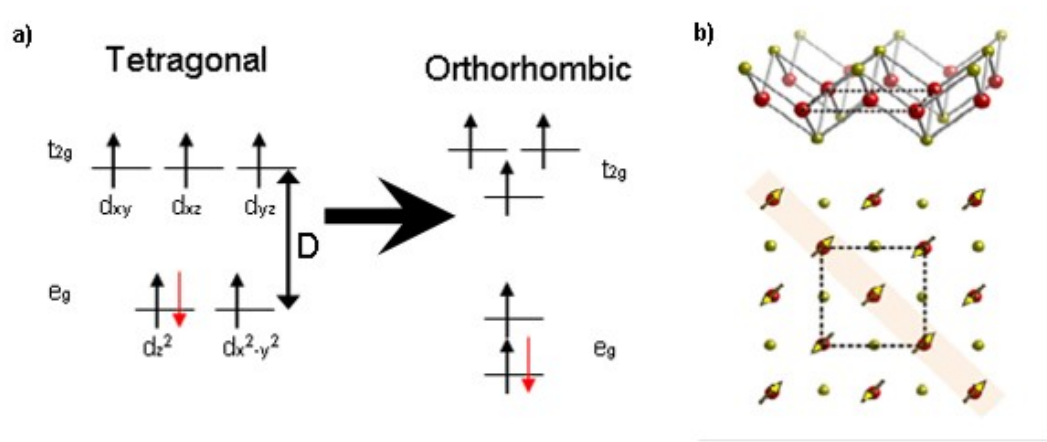


Figure 1.8: (a) Diagram depicting the energy leveling splitting and electron filling of the iron $3d$ orbitals before and after resolution of the Jahn-Teller instability. It is evident after the orthorhombic distortion that the sixth d electron is no longer in a degenerate orbital. (b) Diagram of the antiferromagnetic ordering scheme observed in the iron-pnictide materials [24]. The red atoms represent iron, the yellow represent arsenic, and the arrows represent the direction of magnetic moment. The arrangement shown is stripe antiferromagnetism.

moments create a striped antiferromagnetic ordering (as shown in Figure 1.8b). However, another popular notion is that a spin density wave is responsible for the magnetic behavior observed in these materials. Such a spin density wave would establish itinerant antiferromagnetic order throughout the material, with the spin probability amplitudes of the iron ions moving through the material [30]. A spin density wave could lead to more electronic correlations (in comparison to a local moment picture wherein the magnetic moments are localized to the iron atoms and interact antiferromagnetically), perhaps similar to what is seen in the heavy fermion class of superconductors. Both mechanisms bear further investigation.

Phase Diagrams

The magnetic and structural ordering transition can be suppressed through the application of pressure to these materials or by charge doping them with holes or electrons, either in the iron layer or in the charge donation layer [31]; further doping or pressure induces superconductivity [32–34]. This leads to the construction of doping phase diagrams (Figure 1.9) as previously seen in the cuprates. The near-degeneracy of the Fe orbitals means more electronic bands are likely to be involved in the superconductivity seen in these systems, and most theorists agree that the iron pnictides are multiband superconductors, involving holes and electrons from different bands.

The idea of electron correlations in these materials leads to another interesting consideration: strong electron correlations in the iron-pnictide materials may arise from the existence of a quantum critical point in these phase diagrams. A quantum critical point can be thought of as a zero temperature phase transition that occurs

as the density of carriers in a system grows larger. Quantum fluctuations in such a system eventually require a reordered ground state in order to minimize energy. Experiments so far have been unable to probe the required energy levels to determine whether this truly is the case, in part because of the existence of the superconducting state and an extremely large H_{c2} (up to 60 Tesla in some of these materials), which makes probing any other properties of the material at very low temperatures very difficult without the use of large magnetic fields. [24, 35]

Pairing Mechanism and Gap Symmetry

As mentioned above, one of the most important characteristics of an unconventional superconductor is the symmetry of the pairing order parameter. The definition for an unconventional superconductor requires the breaking of a symmetry. In the case of cuprates, this is easily understood as a d -wave pairing symmetry, which breaks the four-fold rotational symmetry of the Fermi surface. However, the pairing symmetry for the iron pnictides remains an open and intriguing question, and thus the question of broken symmetry also remains undetermined.

Three popular models exist for the multi-band gap symmetry for the iron pnictide materials: s_{++} , s_{\pm} , and d -wave (Figure 1.10). In s_{++} pairing, the phase would be the same everywhere in the gap, regardless of the existence of any accidental (not induced by order parameter symmetry) nodes, while s_{\pm} symmetry would require a change in the phase of the gap between different pockets. Experimental evidence currently leans toward the case of s_{\pm} symmetry on the strength of several phase-sensitive experiments[36–38]. Nonetheless, the evidence fails to be conclusive, mainly owing to the fact that no one experiment so far has been able distinguish s_{\pm}

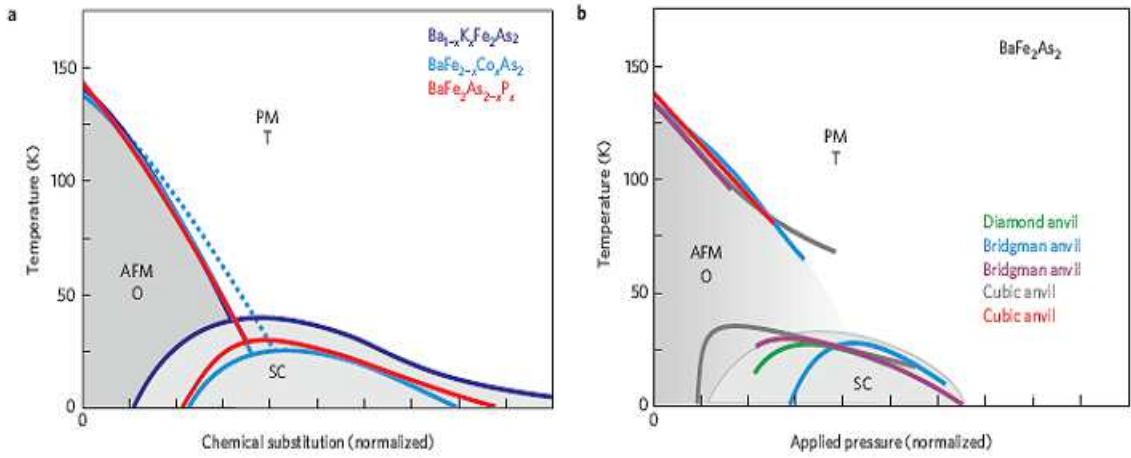


Figure 1.9: Example phase diagrams of iron-arsenide materials. **a** shows the effects of hole-doping (with K), electron-doping (with Co), and isovalent-doping (with P) on $BaFe_2As_2$. **b** shows the effects of pressure, applied using different experimental devices, on the same material. In all cases, it is clear that T_N is suppressed before the onset of superconductivity. [24].

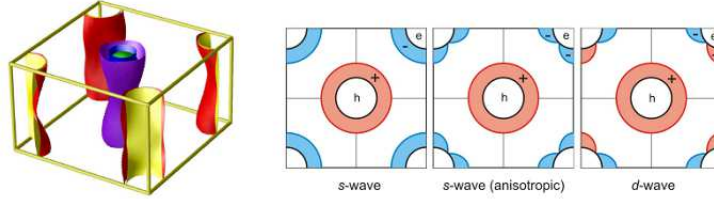


Figure 1.10: **(Left)** A possible three-dimensional Fermi surface corresponding to isotropic s -wave pairing in a quasi-two-dimensional system (suggested for the s_{++} scenario in iron-pnictides). **(Right)** Two-dimensional Fermi surfaces representing isotropic s -wave, anisotropic s -wave, and d -wave pairing symmetries. Taken from ref. [24]

from both s_{++} and d -wave. Fortunately, the depth of knowledge on these experiments is rapidly increasing, and more measurements run on more samples continue to point to a sign-changing order parameter [24].

1.3 Furthering the Iron-pnictices

The lack of a strong understanding of the physics involved in high-temperature superconductivity makes it impossible to predict which materials will be superconductors and which ones will not. This would tend to devolve a search for superconductivity into growing a random potluck of materials and hoping for a good result. However, by deepening our understanding of the known high- T_c unconventional super-

conductors, we might hope to gain insight into the fundamental underpinnings of this complex behavior. In order to do this, a long-view of high- T_c superconductors must find the similarities, as well as the differences, between the well-studied cuprate superconductors and the new iron-based superconductors. Chemical and structural similarities provide a starting point for the investigation of new materials; just as importantly, differences help point out the incidental nature of some characteristics of these two systems. The physics of these two systems then provide basic tests for new materials in order to guide the researcher.

While it is difficult to believe that these two systems, and the similarities between them, present the only possible manifestations of high-temperature superconductivity, the periodic table presents an enormous sample space; making all possible ternary, quaternary, or even higher constituent compounds is not a feasible goal. However, using the cuprate systems as a guide gives both direction and context to the growing iron-pnictide knowledge base.

1.3.1 Chemical Comparison

Chemically, the cuprates and iron-arsenides have a great deal in common. Both are constructed of transport-active layers of atoms, ionically bonded to charge doping layers. In both systems, the charge doping layers have a crucial effect on the observed properties of the materials. Furthermore, both systems require a d -metal atom bonded to nonmetal p -block elements. It is important to note that both the metal and nonmetal are always bridging to other atoms (a rare situation for both

copper and oxygen), and superconductivity is induced in both systems through charge doping. But this is where the similarities appear to end.

Iron is in a d^6 tetrahedral electron configuration, where degenerate e_g orbitals share an electron, while copper is in a d^9 square-planar configuration, where the t_{2g} orbitals are split so that there is no degeneracy. This means that while iron superconductors are subject to a Jahn-Teller instability, cuprate superconductors are not. However, the cuprates do require the resolution of an electronic Mott instability to become superconducting. Additionally, the iron superconductors have a large number of half-filled d -orbitals while the cuprates have only one band that is not completely filled. And many iron superconductors are metallic in the normal state, whereas the cuprates are insulating until doped.

1.3.2 Physics

As both of these systems display high- T_N antiferromagnetic ordering, we begin to expect that this magnetism plays a crucial role in high- T_c superconductivity. Furthermore, the highest transition temperatures in these systems are only observed once the magnetic ordering has been completely suppressed, leading to the belief that, although fundamentally important to the superconducting state, the presence of a magnetically ordered state appears to be antagonistic to the pairing of electrons into a different state. Although well studied in the cuprates, this problem still requires clarification in the iron-pnictides: can high- T_c superconductivity coexist with magnetic ordering in the iron-based superconductors, or are they exclusionary?

Additionally, the presence of structural instabilities in both materials cannot be ignored. In the cuprates, the instability in question is a reordering of the electronic structure. However, the iron-based superconductors generally display a structural transition commensurate with magnetic ordering. One consequence of structural phase transitions is the softening of vibrational phonons modes throughout the lattice. This begs the question as to the nature of the pairing mechanism in these materials: are the iron-based superconductors truly magnetically mediated superconductors, or is there some interplay between the phonons and magnetic excitations? Can these parameters be adjusted to increase T_c ?

Finally, as mentioned previously, it is widely held that a quantum critical point exists in the iron-based superconductors[24]. It is expected that this point exists at the point where the magnetic ordering has been fully suppressed in temperature to 0 K. However, the superconducting dome in the iron-pnictide materials makes it impossible to observe this quantum critical point, since the properties of the superconducting state shield the signatures of any other low-temperature state. Direct evidence of this quantum critical point would provide theorists a way to narrow the plausible models and provide an explanation for the observed superconductivity.

1.3.3 New Materials and Investigations

This thesis will focus on the questions raised here and attempt to provide answers to as many of those questions as possible. In the following chapters, I will discuss a new iron-based superconductor and many of the unique traits that

differentiate it from any other known iron-pnictide. Chapter 3 will present the results of substituting rare-earth atoms into the alkaline earth site in CaFe_2As_2 , resulting in a very high temperature superconducting state that raises many questions about its nature and origins.

One of those questions is the role of the “Collapsed Tetragonal” state. I explore this state in the context of another superconducting compound in Chapter 4. In Chapters 5 and 6, I report on attempts to increase the rare-earth content of our original system. Chapter 7 turns the focus back to the initial materials in question, with a renewed focus on the nature of the observed superconductivity. Finally, Chapter 8 will present a summary of the knowledge gained from these experiments and a theoretical model that helps explain some of these observations. Lastly, an appendix, tabulating the unsuccessful attempts made at discovering new superconducting compounds, is included, as our failures must be reported along with our victories in the search for new superconducting materials.

Chapter 2

Experimental Methods

Like all materials, the iron pnictides are sensitive to the conditions used to create the material. However, the iron pnictides display a remarkable sensitivity to growth conditions that make it very difficult to compare materials grown using different techniques [1, 39, 40]. In this chapter, I will present some of the techniques used to grow these crystals, as well as the methods used to characterize the resulting materials, both chemically and physically.

2.1 Single Crystal Growth

The importance of single crystals to the study of superconductors cannot be overstated. Growing large single crystals allows us to study materials in their purest state, without the added complications that arise from domain boundaries, granular regions, and phase separations that can all have dramatic effects in polycrystalline materials. Generally, the 122 iron pnictide crystals are grown using various flux growth techniques, each of which has varying benefits and pitfalls; therefore, an understanding of these potential problems is necessary. Unfortunately, synthesizing polycrystalline samples of the 122 family of materials has proven surprisingly difficult, given the ease with which single crystals form, so most experiments employ single crystals and the requisite characterization techniques.

2.1.1 Molten Metal Flux Method

The most basic method for growing single crystals of iron pnictide 122 materials is to dissolve the elemental materials (*i.e.* Ca, Fe, and As) into some other lower melting point material, such as Sn, which is called the “flux”. This is accomplished by using comparatively large molar amounts of Sn with smaller amounts of Ca, etc., (all in solid form) The mixture is put in a crucible that can withstand very high temperatures—typically alumina is used, with a melting point of over 2000°C. The crucible and mixture are sealed in a quartz ampoule under vacuum, to eliminate oxygen (quartz is a specific type of glass with a softening point of about 1250°C). [41]

The ampoule is then placed in a furnace and heated to very high temperatures. This allows more of the elemental materials to dissolve into the Sn flux, since solubility increases with temperature. As the ampoule is slowly cooled, the solubility will decrease, and the elemental materials will look to exit the flux and solidify, thus forming a crystal. Because of the low melting point of the flux, it remains a liquid and can be spun out of the crucible at lower temperatures ($\sim 400^\circ\text{C}$) by placing the ampoule in a centrifuge. Ideally, all that remains in the original crucible are the solid crystals of 122 superconductors. [42]

An early improvement, at least in the case of the FeAs-based materials, on this method was the creation of a precursor material; that is, sintering the Fe and As together to create FeAs. This precursor is then placed in the crucible along with the Sn flux and the Ca, etc. The benefits of this procedure are that FeAs has a lower

melting point than pure Fe and a much lower vapor pressure than elemental As. This one step makes the resulting growth process both better (larger crystals) and safer (virtually no toxic As vapor is produced).

The main drawback to this method is the inclusion of Sn within the resulting single crystals. Small amounts of Sn are trapped in the forming crystal. These inclusions can be seen in resistivity drops and diamagnetism at 3.5 K, the superconducting transition temperature of elemental Sn.

2.1.2 Self Flux Method

An alternative to using Sn flux to grow these crystals is using FeAs as the flux. Since the resulting 122 crystals are thermodynamically more stable than FeAs, they will form at higher temperatures, above the melting point of FeAs. Pure FeAs freezes at 1030°C; however, the mixture will also contain some amount of the other starting elements (*i.e.* Ca, etc.), which will lower the freezing point of the FeAs flux. Typically, liquid FeAs can still be spun out of the crucible at 950°C, leaving only the 122 crystals in the crucible.

Unfortunately, there are two drawbacks to this method, with important ramifications. First, quenching from such high temperatures naturally stresses the sample, which may change the measured properties. Second, this method has been shown to produce FeAs inclusions of varying degree. At high temperatures, these inclusions are distributed throughout the material, causing additional strain on the crystal structure. This can be relieved through annealing, discussed below [40].

An alternative is to allow the sample to “furnace cool” from high temperatures. The result is that the flux will solidify around the 122 crystals, creating a solid ingot. Afterwards, this ingot can be broken open and the crystals extracted using a razor blade to cleave the samples away from the flux. Although this technique shows many of the advantages of annealing, extraction of the fragile crystals is much more difficult. Crystal growers use both of these techniques with varying degrees of success. Figure 2.1 illustrates a typical heating schedule for growing iron-pnictide crystals as well as examples of freshly grown crystals.

2.1.3 Thermal Treatments

The importance of proper annealing and treatment of 122 crystals has become obvious, thanks to several studies. First, it was shown that applying pressure to a sample could induce superconductivity at (comparatively) low critical temperatures, which could be relieved through annealing at proper temperatures [39]. More recently, it has been shown that CaFe_2As_2 , which is the focus of many of the following studies, is particularly sensitive to post-growth thermal treatments [40].

For all annealing processes in these studies, already-grown single crystals are again placed in an alumina crucible and sealed in quartz under vacuum. The ampoule is then heated to a specified temperature and held at that temperature for a specified amount of time. Afterwards, the ampoules are removed from the furnace and quenched from the annealing temperature, locking in the desired crystal structure.

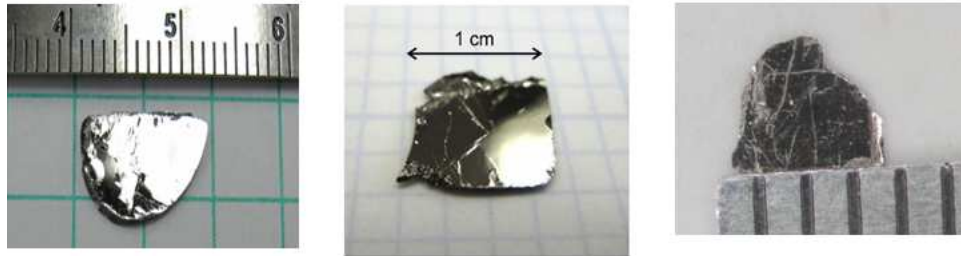
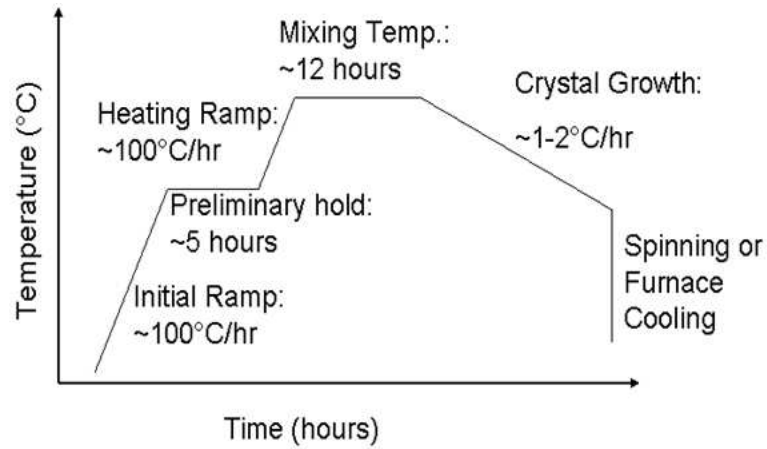


Figure 2.1: (**top**) A generic heating schedule for the growth of iron pnictide crystals. The growth process can take up to two weeks and require temperatures in excess of 1200°C , with spinning temperatures at times around 1000°C . (**bottom**) Pictures of crystals grown using the discussed techniques. From left to right, $\text{Ca}_{0.8}\text{La}_{0.2}\text{Fe}_2\text{As}_2$, $\text{BaFe}_{1.9}\text{Pt}_{0.1}\text{As}_2$, and $\text{Sr}_{0.32}\text{Ca}_{0.47}\text{La}_{0.21}\text{Fe}_2\text{As}_2$. Crystals grow naturally as plates with dimensions of $> 1\text{mm} \times > 1\text{mm} \times \sim 0.1\text{mm}$. The largest crystals can be as large as the crucible used to contain the material during heating.

2.2 Chemical and Structural Characterization

Once single crystals of the desired material are successfully synthesized, we must determine their chemical and structural properties. Energy-dispersive (EDS) and Wavelength-dispersive (WDS) X-ray spectroscopy techniques allow us to determine very accurately which elements are present in a given sample, and the atomic ratios of those elements. X-ray crystallography allows us to determine the structure of the material and the associated lattice constants of the unit cell. Together, these techniques give us a very precise idea of the chemistry of our materials.

2.2.1 Energy-dispersive and Wavelength-dispersive X-ray Spectroscopy

EDS and WDS are very similar techniques, used almost interchangeably, with only differences in precision and accuracy. In either case, we begin by placing the sample into a Scanning Electron Microscope (SEM), which bombards the sample with high-energy (keV range) electrons. For EDS, a special analyzer is placed directly over the sample which measures the characteristic X-rays emitted by the sample in response to the impinging electron beam: the electron beam scatters core electrons from the atoms in the sample, which release X-rays as they leave the atom. For EDS, the full range of X-ray energies is measured at one time, allowing us to determine which elements are present and which are not.

In the case of WDS, the set-up is exactly the same as above. However, instead of an EDS analyzer, a monochromator is inserted into the SEM. This selects out only one wavelength to be analyzed. By using monochromators of several wavelengths,

we can select which few elements are analyzed. WDS allows us to determine very accurately the atomic ratio of the constituent atoms in a given sample. However, due to the necessity of the monochromators, WDS is often performed by specialists with their own equipment. Thus, we often use EDS as a preliminary measurement and send samples for WDS only when accuracy is very important.

2.2.2 X-ray Crystallography

For X-ray crystallography of single crystals, there are two measurements of great importance. The first, reflective crystallography, is the easier and more commonly used. In this measurement technique, a single crystal is placed on a sample and placed into the X-ray machine. Our group uses a Bruker D-5000 diffractometer equipped with a Cu $K\alpha$ source. The X-ray source and analyzer move in conjunction to produce the 2-theta diffraction pattern. Because we are using single crystals, only lattice constants perpendicular to the growth plane can be measured [43]. For 122 crystals, the growth plane is ab -plane, so only $(00l)$ reflections are seen, allowing us to determine only the c -axis lattice constants. Figure 2.2 shows a typical diffraction pattern for a 122 material.

A more intricate technique can allow us to determine the full structure of any single crystal: transmission single crystal X-ray diffraction. For our studies, this technique is usually employed by P. Zavalij in the Chemistry Department, who uses a Bruker Apex2 diffractometer. For a full description of the technique, see reference [43]. This technique will be important in chapters 3 and 4.

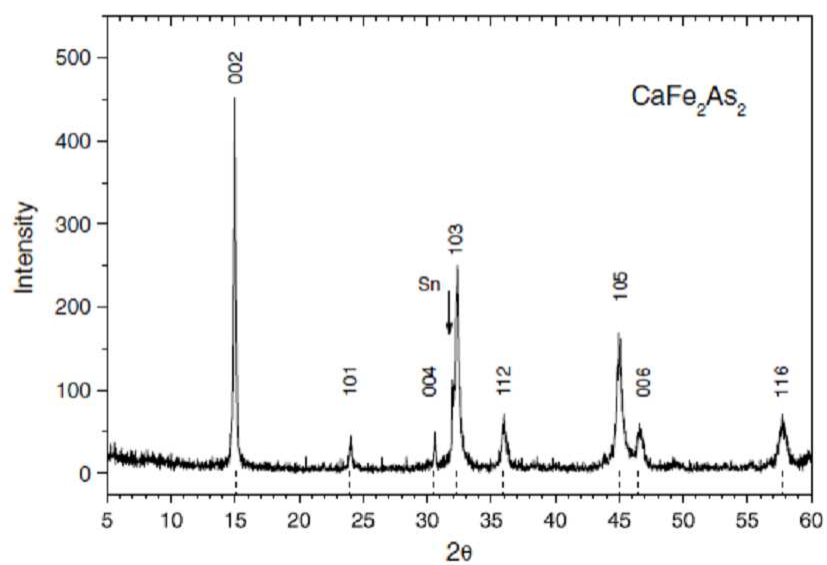


Figure 2.2: Powder X-ray diffraction pattern of crushed CaFe_2As_2 single crystals. Notice the heightened intensity of the $00l$ peaks, resulting from the single crystals growing along the ab plane. Taken from ref. [44]

2.3 Physical Properties Characterization

Once we have established the chemical properties of our material, we can measure the physical properties. Being able to correlate the specific physical properties of samples with the exact chemical properties enables us to form a more complete picture of the roles of doping and pressure in determining the physical properties of these systems. Our group focuses on electrical transport, magnetic susceptibility, and heat capacity measurements in our characterization of superconductors.

2.3.1 Electronic Transport Measurements

Electronic transport measurements actually cover a wide range of measurements and are some of the most important measurements in determining the physical properties of our systems. First, I will cover the different measurements routinely used in our laboratory, including the physics of the measurements. Then, I will discuss the particulars of the measurements, including how we make contacts and the measurement apparatus.

2- and 4- wire Probe methods

We typically use two different configurations for determining the resistivity of samples. Figure 2.3 shows the different configurations for two-wire and four-wire techniques for both longitudinal and transverse resistance measurements.

When samples are especially small, or it is otherwise difficult to attach four wires, we use a two-probe method as shown in figure 2.3a. This technique is considered inferior in that the resistivity that is measured will include not only the

resistivity of the sample, but also the contact resistance of the wires. This is an especially important problem when the contact resistance is close in value to the resistance of the sample being measured, where it can account for a large portion of the measured value. Since most of the samples we measure are semi-metallic or metallic, we avoid this configuration except when we are only interested in corroborating T_c .

More commonly, we use the four probe method in both the longitudinal (figure 2.3b) and transverse (figure 2.3c) configurations. For longitudinal resistivity, a current is applied across the entire sample, and the voltage drop is measured in between the current leads. The voltage drop is measured in parallel with a voltmeter of sufficient impedance so that most of the current continues through the sample. This allows us to neglect the contact resistance. Furthermore, the current and voltage inputs can be switched, effectively cancelling thermoelectric effects.

Longitudinal resistivity is denoted as ρ_{xx} , and is obtained by measuring the resistance of the sample and multiplying by the geometric dimensions of the sample:

$$\rho_{xx} = \frac{V w \cdot t}{I \delta V} \quad (2.1)$$

where V is the sample voltage, I is the current through the sample, w is width of the sample, t is the thickness of the sample, and δV is the distance between the voltage leads.

Transverse resistance (R_{xy}) allows us to determine the Hall coefficient and the carrier concentration of a sample. The voltage is measured across the sample, perpendicular to the current. In addition, a magnetic field is applied perpendicular

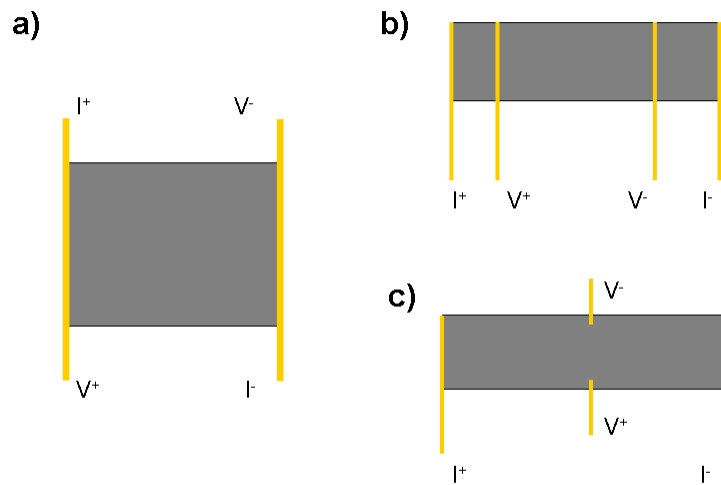


Figure 2.3: Wiring configurations for different resistance measurements. (a) 2-wire configuration for measuring small or problematic samples. (b) Typical 4-wire configuration for measuring longitudinal resistivity. The measurement only occurs between the voltage probes. (c) 4-wire configuration for measuring transverse resistance. A magnetic field is applied perpendicular to the current and voltage paths.

to both the current and voltage. The magnetic field (\mathbf{B}) will induce a Lorentz force (\mathbf{F}) on the charge carriers (q) with velocity (\mathbf{v}) such that

$$\mathbf{F} = q\mathbf{v} \times \mathbf{B} \quad (2.2)$$

resulting in a voltage developing across the sample (R_{xy}). According to Ashcroft and Mermin [13], this is related to the Hall coefficient (R_H) by the thickness (t) and the applied magnetic field (H) such that

$$R_H = R_{xy} \frac{t}{H} \quad (2.3)$$

The Hall coefficient can then be related to the carrier concentration since

$$R_H = \frac{\rho_{xy}}{B} = \frac{1}{ne} \quad (2.4)$$

where n is the charge carrier concentration and e is the elementary charge. This relation holds rigorously for single carrier (electron or hole) systems.

Making Electrical Contacts

Perhaps the most important aspect of the electronic transport measurement is making the contact between the gold wire and the sample. Good contacts not only minimize the contact resistance, they also do not leave stray capacitances that can change the characteristics of the contact. For this reason, we use two primary methods of making electrical contacts: silver paste and solder.

For the silver paste technique, we combine Dupont 4929 paint with a special solvent to make a liquid paste. The gold wires are covered with the paint, then placed on the sample. As the solvent dries, the liquid paint forms a solid paste, adhering the wire to the sample. Mistakes can be erased easily as acetone dissolves the paste, leaving the wire and sample clean. Done properly, this technique is quick and good for samples of all sizes. However, it also has two flaws: the paste is relatively weak so that wires falling off is a common problems, and as the paste dries, it can leave areas for stray capacitances to form, which cannot always be fully driven out.

To combat both of these problems, we also form contacts using solder. A Pb-Sn solder is melted onto the tip of a soldering iron, run at low temperature. The gold wire is painted with a bit of soldering flux appropriate to the solder and the sample. The wire is placed on the sample, and the solder is quickly applied. The advantages here are that the solder joints are very strong, and there are no stray capacitances. However, this method is not suitable for extremely small samples as the solder is more difficult to control. In addition, once the solder is on the sample, it is nearly impossible to remove. For this reason, we use both techniques interchangeably based on the particular samples we are measuring.

Measurement Apparatus

Once ready, our transport measurements are run in a Physical Properties Measurement System (PPMS) designed by Quantum Designs. This machine allows for precise control of sample temperature, electrical fields, and magnetic fields. In the ordinary set-up, temperature is controlled down to 1.8 K by pumping liquid

^4He into a sample pot. By precisely balancing the cooling power of the liquid helium with the heat being supplied through a resistor, the PPMS is able to stabilize temperatures from 1.8 K to 320 K with 0.01 K accuracy. In a more advanced set-up, the temperature can be controlled down to 0.4 K by changing the cryogenic liquid to ^3He in a closed-system environment; the cooling power is dispersed through a coldhead.

The user interface is the main advantage to the PPMS. Samples are simply mounted on interchangeable PPMS pucks and then inserted into the bottom of the PPMS dewar. We have two PPMS set-ups capable of applying fields of up to 14T or 9T, respectively.

2.3.2 Magnetic Susceptibility

In addition to zero resistance, a superconductor must also demonstrate diamagnetism as a result of the Meissner effect as it goes into the superconducting state. In order to observe this, we measure the magnetic susceptibility of our samples. Then, using the appropriate dimensions, we can convert a raw magnetic signal into a superconducting volume fraction (especially important in chapter 3).

Our instrument of choice for these measurements is the Magnetic Properties Measurement System (MPMS) by Quantum Design. The sample is lowered into a helium-cooled dewar with two magnetic coils. One coil applies a magnetic field of up to 7T to the sample space while the other coil measures the magnetic field of the system and the sample. This applied field generates a voltage in the coil, which

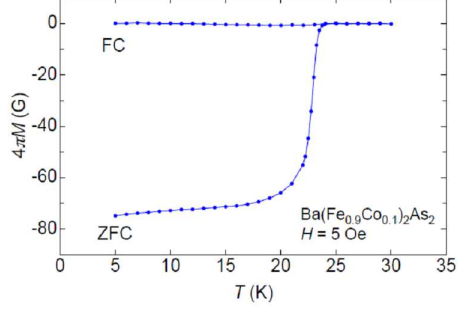


Figure 2.4: Magnetic susceptibility of $\text{Ba}(\text{Fe}_{0.9}\text{Co}_{0.1})_2\text{As}_2$. The large drop in the ZFC at T_c is characteristic of a bulk superconductor. Taken from ref. [45]

corresponds to a given magnetic field. The magnetic response is given in terms of emu.

In order to fully see the magnetic characteristics of a superconductor, we need both field-cooled (FC) and zero-field-cooled (ZFC) measurements. To this end, the sample is inserted into the MPMS and cooled to the base temperature of 1.8 K. A magnetic field is applied, and the sample is slowly warmed up while taking measurements. Once the sample goes into the normal state, it is cooled back down to 1.8 K with the field still applied. A typical diamagnetic curve is shown in figure 2.4. By seeing the FC data as well as the ZFC data, we can understand the roles of effects such as flux trapping and vortex pinning in type-II superconductors.

2.3.3 Heat Capacity

In classifying a superconductor, the most important characteristic is observed in the heat capacity. Heat capacity is the amount of heat required to realize a change in the temperature of a material. More importantly, phase changes are always associated with a change in the heat capacity of the material. Since superconductivity is defined as a phase change in the electronic structure of a material, it also requires a noticeable change in the electronic specific heat. This is manifest as a peak in the specific heat, as shown in Figure 2.5.

In order to precisely measure the specific heat of our samples, we use the heat capacity option on our 14T PPMS. The sample is mounted on a specific heat puck, containing several thermometers. Once inserted into the PPMS, heat is injected into the puck and the decay constant for that heat is recorded. By subtracting the heat capacity of the puck alone from the heat capacity of the puck and sample, we can get an accurate measurement of the heat capacity of our sample. The heat capacity jumps of the Co-doped series of BaFe_2As_2 are shown in figure 2.5.

In addition, heat capacity can also give us information about the ground state of our system. The specific heat capacity of a metal can be fit to the expression

$$C = \gamma \cdot T + \alpha \cdot T^3 \quad (2.5)$$

$$\frac{C}{T} = \gamma + \alpha \cdot T^2 \quad (2.6)$$

where C is specific heat capacity, T is temperature, γ is the electronic portion of the specific heat, and α is the phonon contribution. The relation

$$\frac{\gamma}{\gamma_0} = \frac{m}{m_e} \quad (2.7)$$

gives the relationship between γ and the effective mass of the electron in the system.

Thus, specific heat capacity also serves as a tool to find electron masses that differ from the free electron mass. Such behavior may be seen near quantum critical points, as discussed in the introduction.

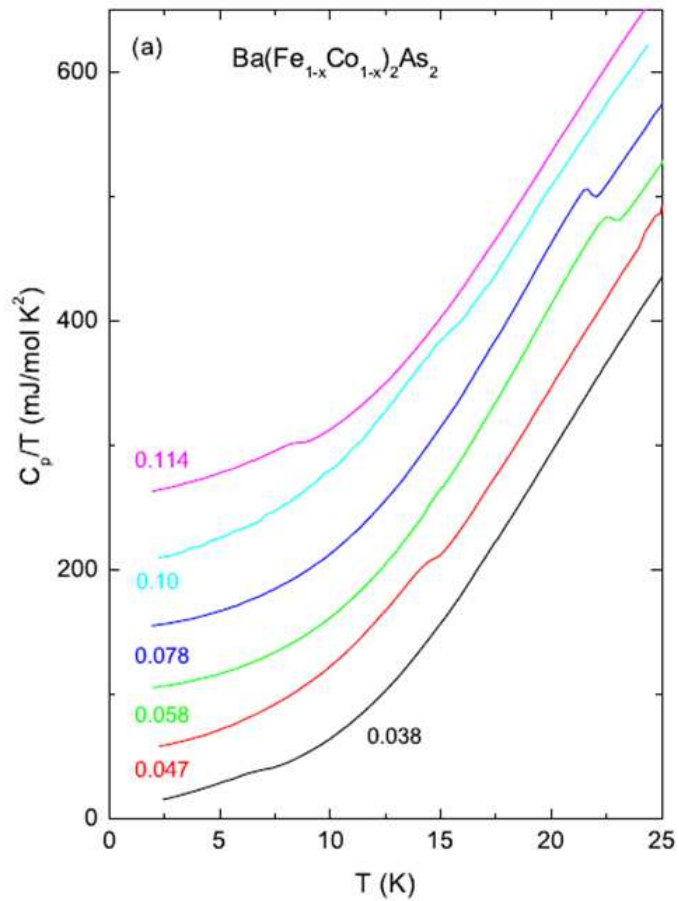


Figure 2.5: Specific heat capacity measurements on the Co-doped BaFe_2As_2 series of compounds. The jumps in heat capacity are especially evident for the 0.058 and 0.078 compounds, near 20 K. Taken from ref. [46]

Chapter 3

Structural Collapse and Superconductivity in Rare-Earth doped

CaFe₂As₂

Portions of this chapter have been summarized or paraphrased from several of my publications, Refs. [1–3]

As mentioned in Chapter 1, the discovery of high-temperature superconductivity in the iron-pnictides has re-energized research in superconducting materials[47]. By providing a new class of high-temperature superconductors which share remarkably similar phase diagrams with cuprates and other superconductors, they present physicists with unique insights into the mechanism of high-temperature superconductivity and its underpinnings [23, 24].

The realm of iron-based superconductors is quite extensive, covering five different structural families[48–50]; however, the “122” family is particularly promising given the large crystal sizes produced through well-known synthesis techniques. These materials crystallize in the ThCr₂Si₂ crystal structure, with over 700 other compounds known to take this same form [51]. This phase, composed of materials

with the chemical composition $A\text{Fe}_2\text{As}_2$ (where A can be Ca, Sr, or Ba), displays T_c as high as 39 K when doped [52–54]. Previously, it has been established that replacing iron with the transition metals Co, Ni, Ru, Rh, Pd, and Ir induces superconductivity between 10 and 20 K, depending on the choice of A [32, 39, 55–64].

The peculiarities of this particular structure, with generic chemical formula AB_2X_2 are further complicated by the ability of the X atoms to achieve inter-layer covalent bonds. As calculated by R. Hoffmann[65], when the separation of the different planar BX layers becomes small enough, the X atoms dimerize. The resulting structure, referred to as a “collapsed” tetragonal structure, undergoes a large ($\sim 10\%$) contraction along the c -axis compared to the length of the “uncollapsed” tetragonal unit cell. Previous studies[66] on the $A\text{Fe}_2\text{As}_2$ materials have found that despite a large change in the c -axis in the substitution series from Ba to Sr to Ca, it remains in the uncollapsed state even down to the pure Ca case. Yet, the application of small pressures and low temperatures to the pure CaFe_2As_2 phase can drive the c -axis into the collapse regime, creating a large reduction in the tetragonal unit cell volume[67, 68].

Furthermore, this application of (non-hydrostatic) pressure to the CaFe_2As_2 system simultaneously gives rise to a 10 K superconducting phase that exists on the boundaries of this collapse[69–71]. However, when similar hydrostatic pressure is applied, no superconductivity is found to occur [72], giving rise to the notion that this 10 K phase is the result of a strain within the crystal. Further experiments involving P-doping on the As site corroborate this picture [73], finding no superconductivity to exist within the “collapsed” tetragonal (cT) state. Calculations also

predict an abrupt quenching of the iron magnetic moment through this transition and a large reordering of the electronic structure[73, 74].

Another important idea is hinted at by the inducing of the collapse transition via P-doping[73]; namely, that chemical pressure resulting from elemental substitution may be a viable alternative to applying physical pressure, in order to coax this structural collapse at ambient pressures. In order to investigate, we synthesized a family of compounds, replacing Ca in CaFe_2As_2 with several rare earth elements[75]. Due to the relatively close 8-coordinate ionic radius of Ca (126 pm) and those of the lighter rare earths La, Ce, Pr, Nd (130, 128.3, 126.6, and 124.9 pm, respectively)[76], we are able to tune the structural parameters of the resulting materials, creating a chemical pressure in the unit cell related to the concentration of the chemical substitution. Furthermore, this aliovalent substitution is also responsible for electron doping the system by replacing the Ca^{2+} ion with the trivalent R^{3+} ions, which acts to suppress the antiferromagnetic (AFM) ordering temperature T_N by tuning the electronic structure. With sufficient suppression of T_N , a superconducting phase with T_c as high as ~ 47 K emerges.

In this chapter, I will detail the structural, electronic, and magnetic properties of the rare earth-doped CaFe_2As_2 system, documenting the structural, magnetic, and superconducting transitions as they evolve with La, Ce, Pr, and Nd doping. The result is a systematic method for controllably tuning the structural collapse of the material. I will present the analytical methods used to characterize the structural and chemical properties of these samples, including X-ray and neutron diffraction. I will document the origins and consequences of the collapsed tetragonal state within

these samples. In addition, I will present the superconducting properties of these materials, indicating both the promises and problems associated with the observed superconductivity. Finally, I will present a phase diagram for these materials that unifies the pressure and doping effects.

3.1 Methods

Using the self-flux method [77] described in Chapter 2, I grew single crystals of $\text{Ca}_{1-x}\text{R}_x\text{Fe}_2\text{As}_2$ with dimensions as large as $\sim 10 \times 10 \times 0.1 \text{ mm}^3$. I then obtained chemical analysis using both EDS and WDS X-ray spectroscopy, finding 1:2:2 stoichiometry for $(\text{Ca},\text{R})\text{Fe}_2\text{As}_2$ as well as the Ca and R concentrations. For neutron scattering, samples were sent to the group of Jeffrey Lynn at the NIST Center for Neutron Research. Single crystal X-ray diffraction was carried out by Peter Zavalij in the Department of Chemistry at the University of Maryland. I performed resistivity and susceptibility measurements using the previously mentioned techniques (Chapter 2).

3.2 Chemical and Structural Characterization

Chemical analysis of the $\text{Ca}_{1-x}\text{R}_x\text{Fe}_2\text{As}_2$ substitution series is presented in Fig. 3.1. At low substitution levels, the measured concentration of rare earth matches very closely with the nominal (pre-reaction) concentration. However, each rare earth species independently reaches an asymptotic behavior, illustrating a solubility limit. Above the solubility limit for each rare earth, no further substitution

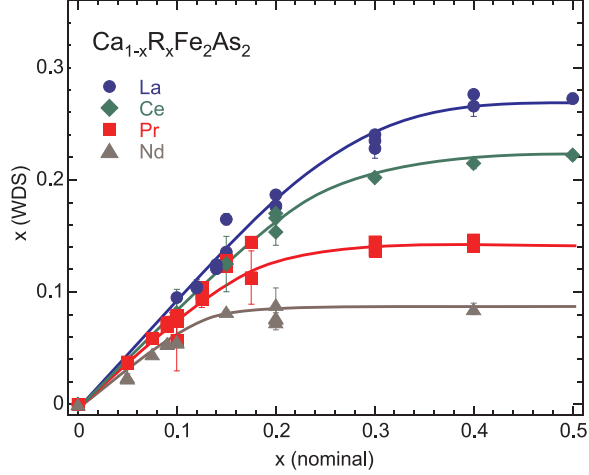


Figure 3.1: Rare earth concentration x in $\text{Ca}_{1-x}\text{R}_x\text{Fe}_2\text{As}_2$ versus the nominal starting rare earth element concentration, as measured by WDS chemical analysis.

occurs, despite nominal concentrations in excess of 50%. La shows the largest solubility limit, nearly 30%, while Nd has the lowest solubility limit at $\sim 9\%$. Naively, Pr should be the best match for Ca in ionic radius size, as shown above, but it has the second lowest solubility limit at only 15%; the solubility limit decreases with decreasing ionic size. A similar effect has been studied in the case of La-substitution for Sr in SrFe_2As_2 , in which the ionic radius of La prevented its substitution for Sr at ambient pressures[78].

3.2.1 X-ray Diffraction Analysis

The a -axis and c -axis lattice parameters, as determined by single crystal X-ray and neutron diffraction experiments at 250 K, are shown in Fig. 3.2. With increasing rare earth, the a -axis lattice constant expands at a nearly uniform rate

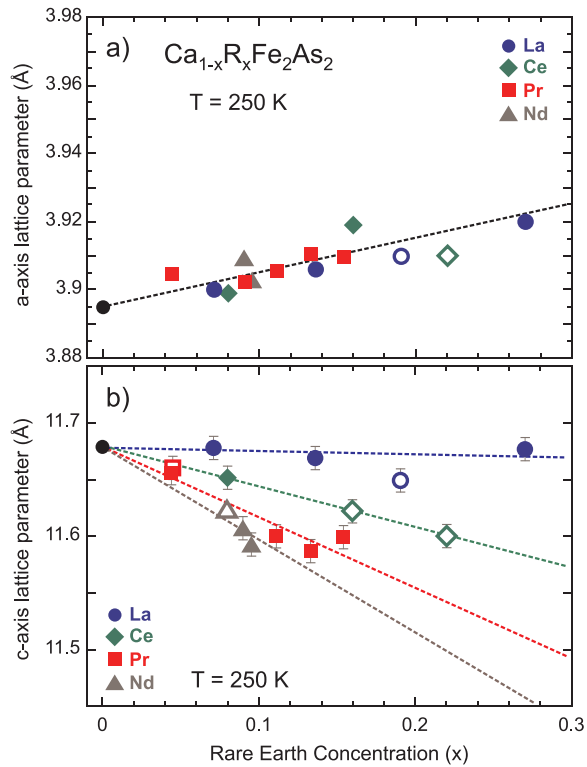


Figure 3.2: Lattice parameters along the a -axis (a) and the c -axis (a) as determined by single crystal diffraction experiments. X-ray measurements are denoted by filled symbols while neutron data is denoted by open symbols. The dashed lines represent least-square fits to the data.

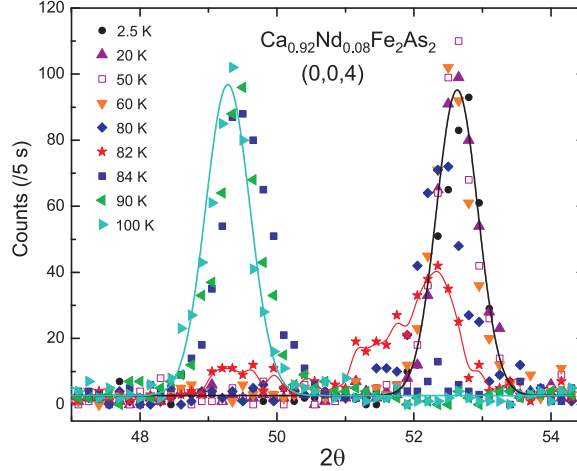


Figure 3.3: Selected raw data from neutron diffraction experiments for crystals of $\text{Ca}_{0.92}\text{Nd}_{0.08}\text{Fe}_2\text{As}_2$. $\theta : 2\theta$ scans at a range of temperatures indicate a sudden shift of the structural (004) Bragg reflection at approximately 82 K upon warming, showing an abrupt transition from the collapsed to the uncollapse tetragonal phase.

regardless of the rare earth species (Fig. 3.2a). However, the c -axis lattice constant (Fig. 3.2b) shows a strong dependence on the rare earth being doped; doping La up to $\sim 30\%$ creates no change in the c -axis, while doping Pr and Nd lead to a strong contraction of the c -axis at much lower concentrations. The scatter and error bars are due to a number of factors including systematic variations in WDS measurements, temperature control fluctuations from maintaining 250 K, sample sizes, and movement between measurement techniques (*i.e.*, X-ray vs. neutron).

3.2.2 Neutron Diffraction Data

Neutron diffraction scans on a single crystal of $\text{Nd}_{0.08}\text{Ca}_{0.92}\text{Fe}_2\text{As}_2$ with a mass of 3 mg (Fig. 3.3) evidence a dramatic structural transtion at ~ 82 K upon

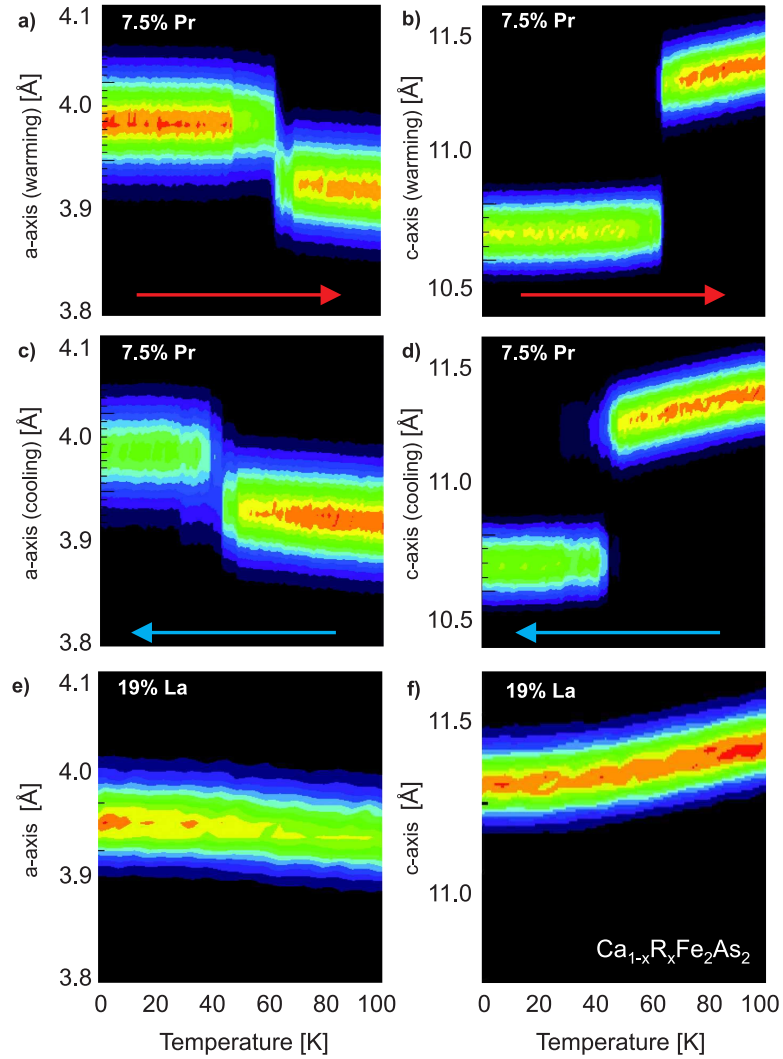


Figure 3.4: False-color plots of the intensity of neutron diffraction reflections of the (110), corresponding to the a -axis, and (006), corresponding to the c -axis, structural Bragg peaks. **a-d** show the collapse transition in the a -axis and c -axis for a sample of $\text{Ca}_{0.925}\text{Pr}_{0.075}\text{Fe}_2\text{As}_2$. Strong first-order jumps in both lattice parameters occur simultaneously upon cooling down and warming up. In the case of $\text{Ca}_{0.81}\text{La}_{0.19}\text{Fe}_2\text{As}_2$ (**e-f**), no such jumps are seen, indicating that La-doped samples do not exhibit the collapse transition.

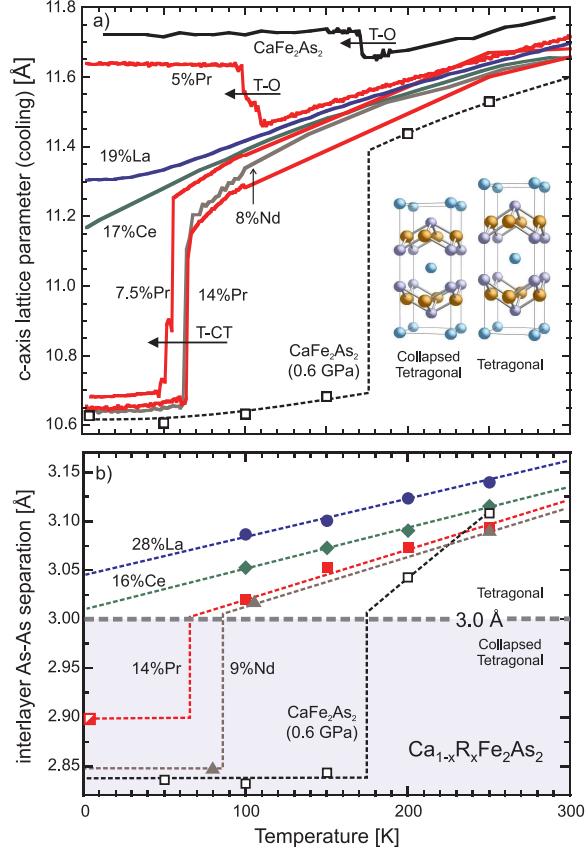


Figure 3.5: Diffraction data for $\text{Ca}_{1-x}\text{R}_x\text{Fe}_2\text{As}_2$ for La (blue), Ce (green), Pr (red), and Nd (brown) substitutions. Data on CaFe_2As_2 under applied pressure (0.6 GPa, black open squares) is included for comparison [67]. (a) *c*-axis lattice constants for a variety of $\text{Ca}_{1-x}\text{R}_x\text{Fe}_2\text{As}_2$ single crystals as determined by neutron diffraction, upon cooling, of the structural (006) Bragg reflection. Here, we can trace the evolution of the various structural phase transitions. (b) Interlayer As-As bonding distances as function of temperature, determined by single crystal X-ray diffraction.

warming—the peak makes a very sudden shift to smaller angles (the peak shift between base temperature and this transition temperature is due to the large thermal expansion of this material). Above the transition, the sample continues with normal, albeit very large, thermal expansion as the peak continues to gradually shift to lower angles.

This dramatic change in the (004) Bragg peak and, correspondingly, the decrease in the c -axis occurs with only 8% Nd substituted for Ca. As shown in Fig 3.4, a similar effect is evident when Pr is substituted for Ca. On the other hand, no such dramatic change occurs in La-doped samples, even up to $\sim 30\%$ La for Ca. This reinforces the idea that the larger La ion does not lead to the same chemical pressure that the smaller Pr and Nd ions create.

The results of this effect on a varied sample population is summarized in Fig. 3.5a. For all samples, large changes in the c -axis lattice constant are evident; however, the sudden and dramatic collapse transition only occurs in Pr- and Nd-doped samples, with small amounts of each acting in a quantitatively similar manner. On the other hand, even large amounts of La and Ce are not able to shrink the c -axis enough to show the collapse transition.

Overall, it becomes clear that the progression of the c -axis lattice parameter with rare earth substitution presents a unique opportunity to controllably apply chemical pressure by choice of rare earth dopant. Next, I will present the nature of this collapse transition and its ramifications.

3.3 The Collapsed Tetragonal State

3.3.1 Origin and Occurrence

Table 3.1: Full single crystals X-ray diffraction data and refinements for a sample of $\text{Ca}_{0.91}\text{Nd}_{0.09}\text{Fe}_2\text{As}_2$ taken at several temperatures. 250 K corresponds to the Tetragonal (T) structure, 105 K is just above the collapse transition, and 80 K is in the collapsed tetragonal state.

Temperature	80 K	105 K	250 K
Structure	CT	T	T
Space group	I4/mmm	I4/mmm	I4/mmm
a (Å)	3.9822(16)	3.9202(15)	3.9025(7)
b (Å)	$=a$	$=a$	$=a$
c (Å)	10.684(4)	11.273(5)	11.591(2)
V (Å ³)	169.43(6)	173.24(5)	176.53(5)
Z	1	1	1
Density(g/cm ³)	6.096	5.964	5.865
Refl.collected	927	1128	1639
Independent refl.	96	99	100
R_{int} ^a (%)	3.38	3.69	3.93
wR_2 ^b , all refl.	2.25	5.74	6.61
R_1 ^c , $I \geq 2\sigma I$	5.11	2.58	3.15
Atomic parameters:			
Nd occupation factor	0.086(7)	0.091(7)	0.097(8)
Ca/Nd	2a(0,0,0)	2a(0,0,0)	2a(0,0,0)
Fe	4d(0,1/2,1/4)	4d(0,1/2,1/4)	4d(0,1/2,1/4)
As	4e(1/2,1/2,z)	4e(1/2,1/2,z)	4e(1/2,1/2,z)
	$z=0.13328(11)$	$z=0.13391(12)$	$z=0.13339(14)$
Atomic displacement parameters U_{eq} (Å ²):			
Ca1/Nd1	0.0089(8)	0.0110(9)	0.0173(10)
Fe1	0.0079(3)	0.0097(4)	0.0158(5)
As1	0.0074(3)	0.0094(3)	0.0158(4)
Bond lengths (Å):			
Ca/Nd-As	3.1554(12)×8	3.1563(12)×8	3.1631(9)×8
Fe-As	2.3494(10)×4	2.33568(7)×4	2.3736(10)×4
Fe-Fe	2.8158(11)	2.7720(11)	2.7595(5)
Bond angles (deg):			
As-Fe-As	115.88(6)×2	112.54(6)×2	110.58(7)×2
	106.37(3)×4	107.96(3)×4	108.92(3)×4
Fe-As-Fe	73.63(3)×4	72.04(3)×4	71.08(3)×4

^a $R_{int} = \Sigma[F_o^2 - F_c^2(\text{mean})] / \Sigma[F_o^2]$

^b $wR_2 = \Sigma[w(F_o^2 - F_c^2)^2] / \Sigma[w(F_o^2)^2]^{1/2}$

^c $R_1 = \Sigma \| |F_o| - |F_c| \| / \Sigma F_o$

Table 3.1 presents the full structural refinement data for a 9% Nd sample at temperatures above and below the collapse transition and is represented graphically

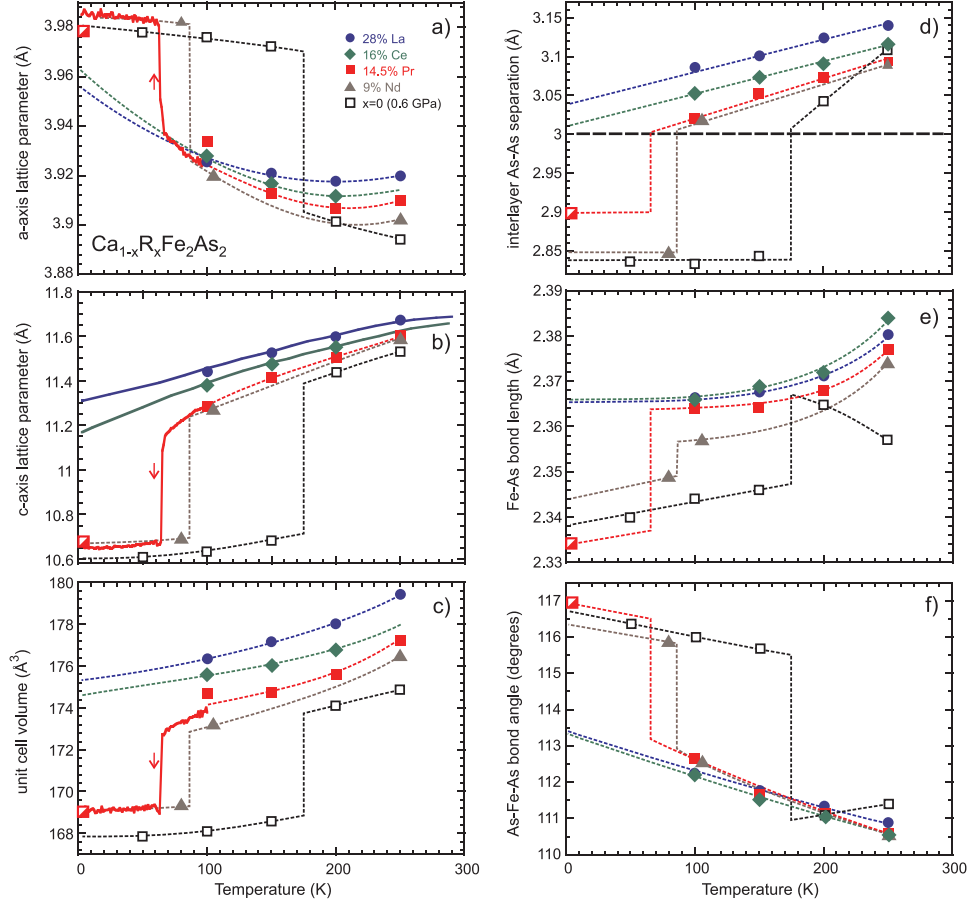


Figure 3.6: Unit cell and substructure parameters for several $\text{Ca}_{1-x}\text{R}_x\text{Fe}_2\text{As}_2$ samples. Solid lines denote single crystal neutron diffraction data; red open squares denote neutron powder diffraction, and solid squares denotes single crystal X-ray diffraction data. Solid black circles (X-ray on undoped CaFe_2As_2 samples) and open black squares (hydrostatic pressure study of CaFe_2As_2) are reproduced from Ref. [67].

in Fig. 3.2, along with several other characteristic samples. The data here are collected at fixed temperatures, providing a more systematic study of the structural parameters. In typical Fe-based compounds, the Fe-As bonding distance remains relatively rigid despite doping or pressure effects. However, in this material, it decreases significantly with temperature from 250 K down to 100 K for dopings of La 28%, Ce 16%, Pr 14.5% and Nd 9%, as shown in Fig. 3.6e. The Fe-As bond length contracts even more dramatically in samples undergoing the collapse transition, just as the a -axis plane is increasing. Perhaps even more importantly, the As-Fe-As tetrahedral bond angle displays an even stronger temperature dependence (Fig. 3.6f). Such a large change in this bond angle is indicative of the the large thermal expansion observed in this material.

Despite charge doping, the absolute value of the c -axis contraction through the collapse transition is similar to what is found in CaFe_2As_2 under pressure[67]. Thus, the dominant contribution to the bonding and the driving force of the collapse transition comes from the As-As bonds, which results in the very large c -axis thermal expansion observed in this region. Even without the collapse transition, a 22% Ce sample shows a 5.3% expansion of the c -axis between 0 and 300 K, resulting in a linear thermal expansion coefficient of $180 \times 10^{-6}/\text{K}$, one of the largest of any metal studied (*e.g.*, as compared to the largest known thermal expansion values of 97, 83 and $71 \times 10^{-6}/\text{K}$ for elemental Cs, K and Na, respectively, at 25°C [79]), and even rivals the largest known values for any solid as observed in molecular crystals [80].

The increasing overlap of interlayer As atoms, resulting from chemical pressure arising from the rare earth ions, drives the c -axis contraction and the resulting

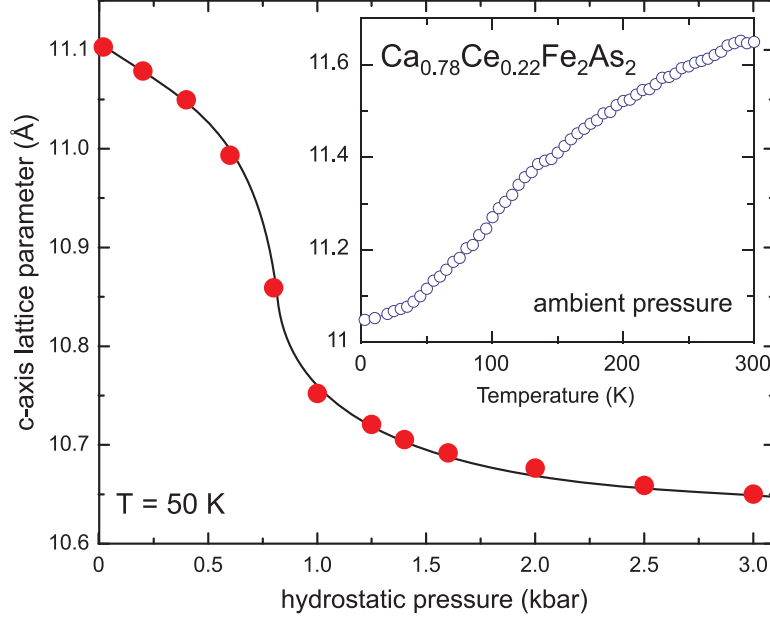


Figure 3.7: Neutron diffraction measurements of the c -axis of a 22% Ce sample placed under hydrostatic pressure (applied in He-gas cell). The sudden change between 0.5 and 1.0 GPa corresponds to the collapse transition.

collapse transition[65, 74]. At a critical distance of $\sim 3.0 \text{ \AA}$, this overlap leads to the formation of As-As bonds (dimerization) in Pr- and Nd-doped samples, just as when CaFe_2As_2 is placed under pressure[67]. On the other hand, La- and Ce-doped samples are never able to cross this threshold, even down to 0 K, and so never experience the collapse transition (Fig. 3.5b).

Accordingly, the highest-doped Ce compound should be just on the verge of collapse at ambient pressure and low temperatures; application of a small amount of external pressure to a 22% Ce crystal, whose As-As separation approaches 3.0 \AA at zero temperature, confirms this scenario. Using neutron diffraction, we are able

to study the c -axis lattice parameters as a function of applied pressure, using an Al-alloy He-gas pressure cell, as was used in a previous experiment[81].

As shown in Fig. 3.7, the collapse transition can be induced in this sample with less than 1.0 GPa of applied pressure. In the undoped CaFe_2As_2 compound, the pressure required to induce this transition is an order of magnitude greater, demonstrating the consequences of the c -axis contraction upon rare earth doping. Similar P-based materials SrRh_2P_2 and EuRh_2P_2 undergo the same collapse tetragonal transition upon crossing this same 3 Å threshold, despite the replacement of As for P[82]. This can be understood since 3 Å is also the average value between the Van der Waals and covalent radii for both As and P[79], suggesting that any system with such overlapping p -orbitals may be pulled into the collapsed tetragonal state at this critical interlayer separation.

3.3.2 Consequences of the Collapsed-Tetragonal Transition

The transition from uncollapsed-tetragonal to collapsed-tetragonal requires a strong reordering of the electronic structure [73]. In addition, theoretical predictions have claimed that the Fe magnetic moment should disappear in the collapsed tetragonal state[74]. I will next present NMR studies, performed by collaborators, probing the magnetic state of Fe, conducted on $\text{Ca}_{1-x}\text{R}_x\text{Fe}_2\text{As}_2$ crystals showing the uncollapsed to collapsed tetragonal transition.

For Nuclear Magnetic Resonance studies, two compositions ($x = 0.075$ and 0.15, determined by WDS) were chosen. NMR experiments, performed by Long Ma

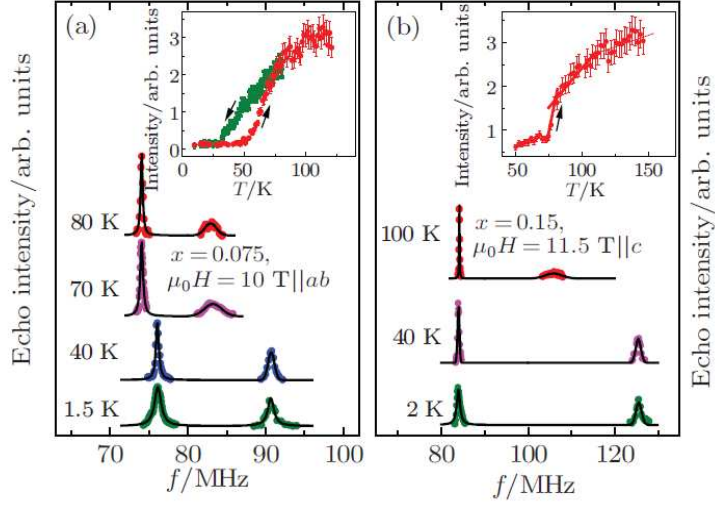


Figure 3.8: (a) ^{75}As NMR spectra for a 7.5% Pr single crystal with a 10 T field applied in the ab -plane. (b) ^{75}As NMR for a 15% Pr single crystal with an 11.5 T field applied along the c -axis. Inset: Spectral weight as a function of temperature, fixed at the central transition of the Tetragonal phase. Arrows indicate direction of warming or cooling.

and the group of Wei-Qiang Yu in the Department of Physics at Renmin University of China in Beijing, were carried out using the standard coherent pulse method. The sample was placed on a rotator (to allow for the changing of magnetic field orientation), and the frequency-swept NMR spectra were obtained by integrating the intensity of the Fourier transform of the spin echo signal. The spin-lattice relaxation rate $1/T_1$ is obtained by the inversion recovery method.

As shown in Fig. 3.8, the structural transition is evidenced by a large frequency shift of the satellite peak upon cooling. Due to the four-fold in-plane symmetry of ^{75}As , the electric field gradient lies along the c -axis and, therefore, the nuclear quadrupole resonance frequencies (ν_q) can be evaluated by the angular dependence of the satellite, $f = \nu_L(1 + K) \pm \nu_q(3\cos^2\theta - 1)/2$, where ν_L and K represent the

Larmor frequency and the Knight shift, and θ represents the angle from the field orientation to the crystalline c -axis. The structural collapse leads to an increase in ν_q , resulting in shifts to the high-frequency satellites. The ν_q increases through the structural transition from 20.4 MHz to 35.8 MHz for $x = 0.075$, and 21.6 MHz to 41.5 MHz for $x = 0.15$. The frequency of the central transition also changes as a result of the collapse (Figs. 3.8a and b), due to a second-order quadrupole correction $f = (1 + K)\nu_L + \frac{3\nu_Q^2}{16\nu_L}(1 - \cos^2\theta)(9\cos^2\theta - 1)$.

Further investigation of the high-temperature tetragonal phase shows an increase of ν_q with increasing Pr^{3+} , consistent with a chemical pressure effect. The ν_q is estimated to be ~ 20.4 MHz for $x = 0.075$ and ~ 21.6 MHz for $x = 0.15$. For comparison, the ν_q of CaFe_2As_2 increases with pressure from 11.8 MHz at $P = 0$ to 25 MHz at $P = 1.08$ GPa[83].

As shown in Fig. 3.9, the Knight shift hardly changes with decreasing temperature above the collapse transition. However, below the transition, it drops sharply with decreasing temperature. This drop is unlikely to be a paramagnetic effect because transport measurements suggest that the carrier density on the Fermi surface increases through the structure collapse[1], which in principle should not lead to a large decrease of ^{75}K from Pauli paramagnetic contributions. More likely, it is caused by a spin correlation effect: since the NMR Knight shift (K) is proportional to $\chi(q = 0)$, where $\chi(q = 0)$ is the electron susceptibility, the reduced $K(T)$ signifies a large suppression of local paramagnetic spin fluctuations of Fe upon the structural collapse. At 2 K, $K(T) \sim 0$, suggesting that the Fe moment has dropped nearly to zero in the cT phase. Similar logic applies to the Pr 15% sample.

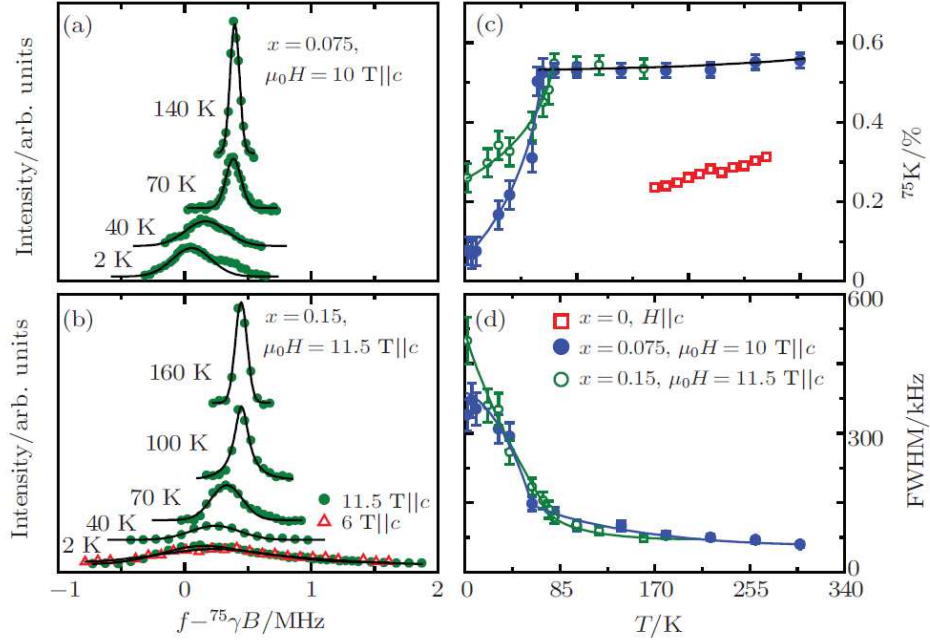


Figure 3.9: (a) The ^{75}As spectra of the Pr 7.5% sample (10 T field along the c -axis). (b) The ^{75}As spectra of the Pr 15% sample, with 6 T and 11.5 T field along the c -axis. (c) The Knight shift of the $\text{Ca}_{1-x}\text{Pr}_x\text{Fe}_2\text{As}_2$ samples as a function of temperature. The $x = 0$ data are adapted from Ref. [84]. (d) The FWHM of the ^{75}As central transition as a function of temperature for the two dopings.

This NMR study shows that the Fe magnetic moment is in fact quenched in the cT phase, as proposed by T. Yildirim[74]; the Fe remains paramagnetic in the tetragonal state[85, 86]. This constitutes the first experimental evidence that the Fe moment is quenched during the collapse transition, suggesting the Fe moment is sensitive to either the Fe-As-Fe bond angle or the pnictogen(As) height, both of which change dramatically through the collapse transition.

3.4 Superconducting Phase

Rare earth doping also presents another interesting effect: the replacement of Ca ions with rare earth ions introduces more charge carriers into the system, allowing us to measure the effects of chemical pressure and charge doping simultaneously. This presents an interesting mechanism for fine-tuning the structural and electronic parameters of a system known to be very sensitive to both of these effects. In the pure CaFe_2As_2 compound, a tetragonal (T) to orthorhombic (O) phase transition is commensurate with the onset of antiferromagnetism (AFM) at $T_N \sim 165$ K. As seen in other 122 systems, this transition temperature is suppressed with increasing rare earth doping, eventually driving to absolute zero.

In this section, electrical resistivity ρ and Hall effect R , measured with the standard four-probe ac method, and magnetic susceptibility χ , measured in a SQUID magnetometer, are used to track the evolution of both structural and electronic properties as a function of rare earth substitution.

3.4.1 Electrical Transport and Magnetic Susceptibility

The doping evolution of electrical transport measurements for $\text{Ca}_{1-x}\text{La}_x\text{Fe}_2\text{As}_2$ and $\text{Ca}_{1-x}\text{Pr}_x\text{Fe}_2\text{As}_2$ are shown in Fig. 3.10a and b, respectively. The sharp jump at $T_N = 165$ K in CaFe_2As_2 is due to a structural phase transition from tetragonal to orthorhombic phases and is known to coincide with the onset of antiferromagnetic order [44, 81, 87]. Substitution of La and Pr act to suppress T_N to lower temperatures. In the case of La-doping, it is fully suppressed (down to base temperature ~ 30 mK). In the $\text{Ca}_{1-x}\text{Pr}_x\text{Fe}_2\text{As}_2$ series, the appearance of the collapse transition truncates the suppression, eliminating any magnetic ordering, as discussed previously.

Similarly, magnetic susceptibility data (Fig. 3.10c and d) corroborate this trend. At concentrations near the critical concentration ($\sim 15\%$) for full suppression of the AFM phase in the La compound, the susceptibility is quite flat with decreasing temperatures. However, for larger La concentrations, the behavior becomes increasingly paramagnetic. Since La is nonmagnetic, this increasing magnetic moment must be attributed to the FeAs sublattice. On the other hand, $\chi(T)$ enhances strongly with Pr substitution due to the increasing concentration of Pr localized $4f$ electrons and their contribution of a Curie-like susceptibility. Although gradually depressing T_N the appearance of a first-order transition at the concentration of 7.5% Pr coincides with the cT transition.

The hysteresis of the collapse transition in all measurements (structural, magnetic, and transport) indicates the strong first-order nature of this transition. While

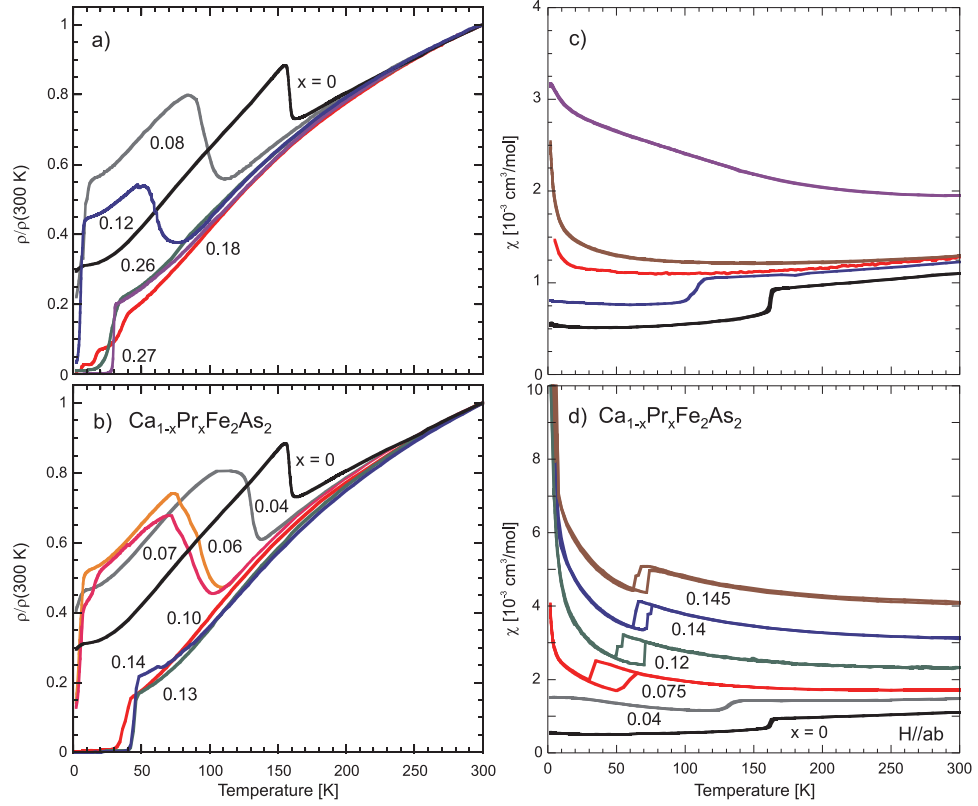


Figure 3.10: (a) Electrical resistivity of crystals from the $\text{Ca}_{1-x}\text{La}_x\text{Fe}_2\text{As}_2$ system, normalized to the value at 300 K. Increasing La content drives the AFM transition (seen as a sharp jump at 165 K in the $x = 0$ data) down in temperature, until it is no longer evident. At high La concentrations, superconductivity with a maximum T_c of 30 K is observed. (b) Electrical resistivity of crystals from the $\text{Ca}_{1-x}\text{Pr}_x\text{Fe}_2\text{As}_2$ system, normalized to the value at 300 K. Again, increasing Pr content drives down the AFM transition; however, T_c for this system reaches as high as 47 K. Note also the transition ~ 70 K in $x = 0.14$, indicating the collapse transition. (c,d) Magnetic susceptibility of $\text{Ca}_{1-x}\text{La}_x\text{Fe}_2\text{As}_2$ and $\text{Ca}_{1-x}\text{Pr}_x\text{Fe}_2\text{As}_2$ respectively. $\text{Ca}_{1-x}\text{La}_x\text{Fe}_2\text{As}_2$ shows paramagnetic behavior to low temperatures, as does $\text{Ca}_{1-x}\text{Pr}_x\text{Fe}_2\text{As}_2$. However, $\text{Ca}_{1-x}\text{Pr}_x\text{Fe}_2\text{As}_2$ also displays a hysteretic region in high Pr concentrations, indicating the collapse transition upon cooling and warming. Data are shifted for clarity.

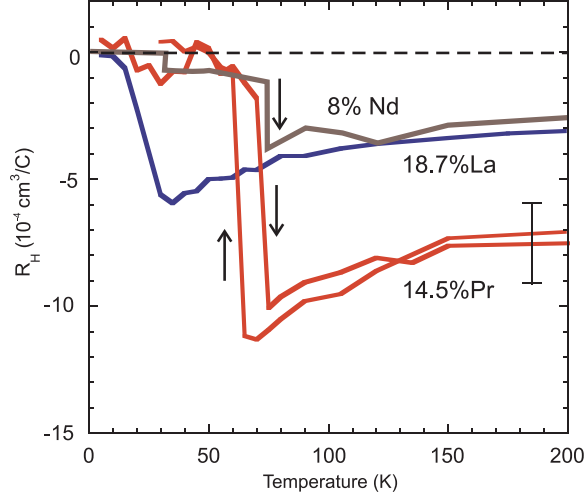


Figure 3.11: Hall Effect data for highly-doped $\text{Ca}_{1-x}\text{R}_x\text{Fe}_2\text{As}_2$ crystals. Both Pr 14.5% and Nd 8% show strong hysteretic transitions between 60 and 80 K, indicative of the collapsed tetragonal transition. However, even 18.7% La for Ca does not induce this transition. The black error bar denotes the resolution of the experiment.

the magnetic characteristics of this transition are not dependent on the rare-earth species being substituted (Pr- and Nd-doped crystals display remarkably similar behavior), the magnitude of the transition, as expressed in the electrical transport measurements, does seem to vary with rare earth concentration. Under applied pressures, this transition is nearly 10% between $\rho(300\text{ K})$ and $\rho(0\text{ K})$ in the undoped CaFe_2As_2 [72]; however, the magnitude of this transition is nearly 0 in Pr 14.5% crystals. This may be related to the electron doping effect: the magnitude of the transition decreases with increasing rare earth content.

Fig. 3.12 summarizes the superconducting properties for the full $\text{Ca}_{1-x}\text{R}_x\text{Fe}_2\text{As}_2$ series, exhibiting high-temperature superconductivity with a maximum T_c reaching 47 K. This value is much larger than any previously reported value in electron-

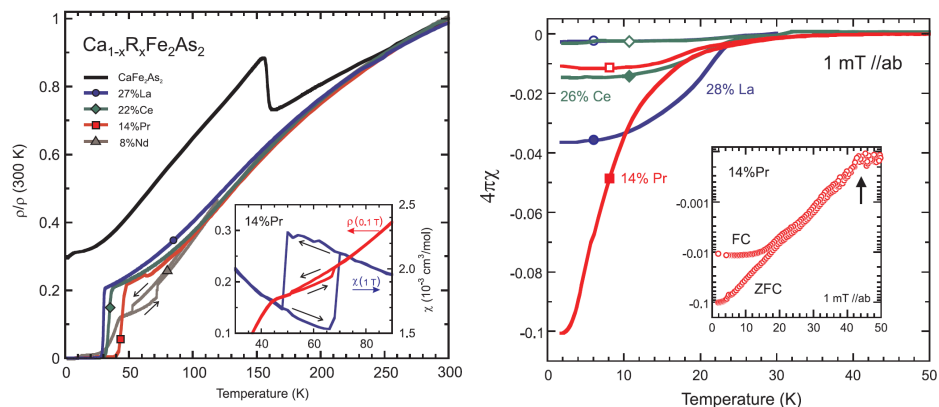


Figure 3.12: Summary of the superconducting characteristics of $\text{Ca}_{1-x}\text{R}_x\text{Fe}_2\text{As}_2$ as shown in resistivity (**left**) and susceptibility (**right**), covering the full range of rare earth ions that substitute for Ca, with R=La (blue), Ce (green), Pr (red) and Nd (brown), and compared to undoped CaFe_2As_2 (black). The left inset shows the hysteresis of the collapse transition in both resistivity and susceptibility. The right inset shows the onset of diamagnetism at $T_c = 44\text{ K}$, indicating superconductivity, in 14% Pr.

doped intermetallic FeAs based superconductors, including transition metal doped 122 systems as well as the only other reported case of rare earth substitution into a 122 system in $\text{Sr}_{1-x}\text{La}_x\text{Fe}_2\text{As}_2$ [78], even exceeding the previously reported high of 38 K found in $\text{Ba}_{1-x}\text{K}_x\text{Fe}_2\text{As}_2$ compounds[52]. In fact, it is approaching the highest reported T_c value for any iron-based superconductor, found in the (Ca,R)FeAsF materials[88].

The high T_c of these materials is consistent with the commonly accepted hypothesis that minimizing chemical disorder in the active FeAs layers should lead to higher temperature superconducting transitions. Substitution into the alkaline earth site rather than the FeAs plane suppresses T_N without introducing disorder effects (such as pair-breaking, as seen in the transition-metal doped 122 compounds[89]). Surprisingly, though, the high- T_c phase is seen to exist in both the uncollapsed phase and in the collapsed phase, which creates a strong reordering of the electronic structure. The appearance of this high- T_c phase may indicate an insensitivity of the pairing mechanism in the Fe orbitals to the configuration of the As p -orbitals, which would place strong constraints on a microscopic model of superconductivity in these materials.

Moreover, the prediction[74] and confirmation of a non-magnetic ground state in the cT phase is tantalizing in that it may suggest superconductivity originating in a phase without spin fluctuations. The long-held belief is that iron spin fluctuations are paramount to the superconductivity in these materials; evidence to the contrary could be pivotal in reaching an understanding of the pairing mechanism in the iron-

based superconductors. However, more investigations must take place before such a conclusion can be drawn.

3.4.2 Evidence of Intrinsic SC

Also evident in Fig. 3.12 is the small superconducting volume fraction measured in these materials. Regardless of the rare earth element chosen, the volume fraction remains at or below the 10% level, indicating that the superconductivity in these materials is not of a bulk nature. Naturally, this raises questions as to whether this superconducting phase is inherent to these materials, or the result of some strain, inhomogeneity, or impurity phase.

Experimental constraints make it impossible to rule out the possibility of a small amount of non-collapsed tetragonal phase in our single crystals, at or below the $\sim 1\%$ level. However, the dramatic difference in lattice constants between the cT and tetragonal phase, and the lack of any evidence for two distinct phases in both neutron scattering and single-crystal X-ray diffraction, make this an unlikely scenario. Yet, the ability to control the cT phase at ambient pressures and using temperature to tune the lattice in to and out of the collapsed phase allows for studying the magnetism of these compounds in a manner similar to the work that has been done for the undoped compound placed under pressure[68]. In this section, I will report on investigations to rule out extrinsic origins for the superconductivity found in the $\text{Ca}_{1-x}\text{R}_x\text{Fe}_2\text{As}_2$ series.

Although full volume fraction screening is not observed in these crystals (Fig. 3.12), the superconductivity does appear impervious to standard annealing, etching, and oxidation experiments, suggesting that the superconductivity in these materials is not the result of an obviously extrinsic phase. These experiments are reported in detail below.

Our first observation is the systematic nature of the appearance of superconductivity in all of these materials. T_c values in resistivity and magnetization between 30 K and 47 K are only found in samples which are highly-doped, thus strongly suppressing AFM order. Although a low- T_c phase (~ 10 K) does stubbornly appear in lower doped samples, it also shows traces in undoped CaFe_2As_2 [69–71] as a strain-induced transition resulting from non-hydrostatic pressure conditions. On the other hand, the high- T_c phase seems to be distinct and stabilized by the extra carriers coming from rare earth substitution, as isovalent substitution has been shown not to induce superconductivity[73].

The fact that higher- T_c transitions never occur in samples with rare earth concentrations still showing AFM ordering rules out the possibility of a randomly occurring impurity phase. Instead, it suggests that the pairing mechanism in this superconductivity is strongly related to the suppression of AFM. Additionally, such an impurity phase has not been evidenced in any of our structural measurements, and residual fitting factors on our X-ray diffraction measurements are consistently at or less than $\sim 3\%$, placing an upper threshold on the possibility of an impurity phase. The consistent absence of superconductivity in AFM samples makes a strong statistical argument against the possibility of an impurity phase.

The large T_c values in these systems are also much larger than the transition temperatures resulting from strained CaFe_2As_2 [69–71] or in the strained SrFe_2As_2 “20 K” phase [77], making it unlikely that strain-induced superconductivity is responsible for the high transition temperatures seen in the $\text{Ca}_{1-x}\text{R}_x\text{Fe}_2\text{As}_2$ materials. While strain may indeed be playing some role, the large change in lattice parameters associated with the collapse transition and a corresponding *lack* of this transition to influence such a strain mechanism, as well as the presence of superconductivity in collapsed or uncollapsed states, make for a difficult scenario in which strain is the key ingredient.

However, to rule out strain mechanisms as a concern we have performed annealing studies of superconducting samples, both with and without structural collapse conditions present. Starting with as-grown La- and Pr-substituted samples that exhibit Meissner screening, we first performed susceptibility measurements of each sample to characterize their as-grown properties and then subjected each sample to an annealing treatment. This consisted of sealing each sample in a separate quartz tube together with Ta foil for oxygen absorption under partial Ar gas pressure, heating to 700°C and holding at that temperature for 24 hrs before cooling to room temperature. Immediately after the annealing sequence, the susceptibility of each sample was measured following the same procedure as before.

Fig. 3.13 a and b present the results of the before- and after-annealing measurements. Although there are finite changes in the measured screening fractions, the main result is that both samples still exhibit Meissner screening after their annealing treatments. Furthermore, while the La-substituted sample shows a reduction in

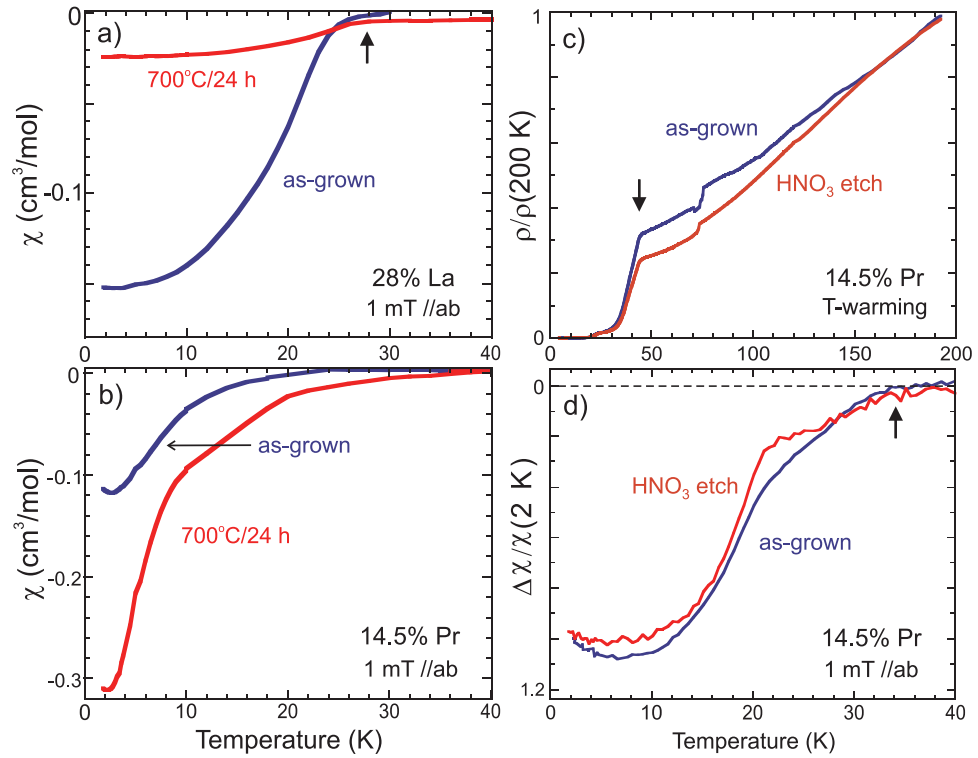


Figure 3.13: The effects of annealing and etching treatments on the superconductivity in $\text{Ca}_{1-x}\text{R}_x\text{Fe}_2\text{As}_2$. A 28% La crystal (a) and a 14.5% Pr crystal (b) are annealed for 24 hours at 700° K. (c) and (d) are the resistivity and magnetization, respectively, for a 14.5% Pr crystal, shown as-grown and after being etched vigorously in nitric acid. For clarity, only zero-field-cooled data is presented.

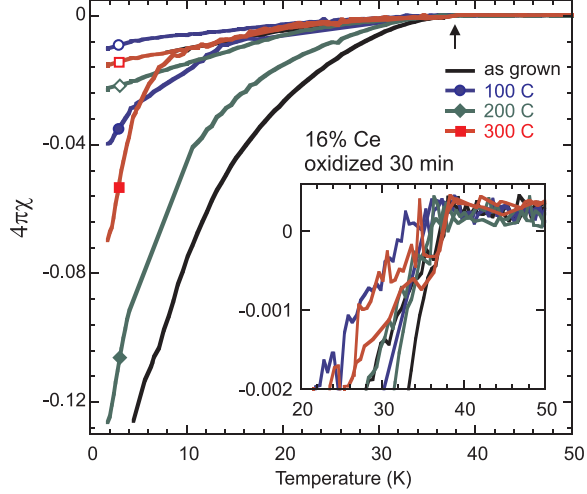


Figure 3.14: Effect of surface oxidation on a 16% Ce-doped sample of $\text{Ca}_{1-x}\text{R}_x\text{Fe}_2\text{As}_2$, shown for the as-grown sample and for repeated exposures to air under heated conditions. The inset demonstrates the onset of Meissner screening for all exposures at $T_c=35$ K

diamagnetic signal, the Pr-substituted sample in fact shows a small enhancement, reflective of the absence of any systematic trends to enhance or reduce Meissner screening under this heat treatment schedule. This is in stark contrast to what happens in stoichiometric SrFe_2As_2 , where annealing completely removes any signature of superconductivity [77].

Finally, to rule out the possibility that surface phases are responsible for partial Meissner screening, we have checked the effect of both etching and oxidation on the superconductivity in $\text{Ca}_{1-x}\text{R}_x\text{Fe}_2\text{As}_2$. With T_c values approaching those of the oxygen-based iron-pnictide superconductors, it is important to check for the possibility that oxygenated surface phases somehow achieve optimal oxygen doping for superconductivity and are providing the partial screening observed here. As shown in Figs. 3.13c-d, we have measured both resistivity and magnetic susceptibility of a

15% Pr sample both before and after etching the sample in concentrated HNO_3 for 30 sec, which removed $\sim 25\%$ of its mass. It is clear that superconductivity survives this harsh treatment, which results in no change in qualitative screening behavior, as well as very little change in resistivity signatures of both the collapse transition near 70 K and the superconducting transition that begins at 40 K.

To further verify that oxidation is not the cause of enhanced screening, the susceptibility of a 16% Ce-doped sample with $T_c=35$ K was measured first as-grown and then after subsequent exposures to air under heated conditions on a temperature-controlled hot plate. As shown in Fig. 3.14, there is again no systematic trend observed after repeated oxidations, with the onset of Meissner screening not changing significantly even after visible oxidation from 300°C exposure (volume fraction variations are likely due to uncertainty in mass changes due to handling, as well as damage to the sample from oxidation).

Together, these tests strongly reduce the likelihood of the observed high- T_c superconducting phase in $\text{Ca}_{1-x}\text{R}_x\text{Fe}_2\text{As}_2$ originating from extrinsic sources such as strain mechanisms, surface states or foreign phases including oxides or other contaminants. Yet, the consistently small superconducting volume fractions point to a phase that does not occupy the bulk of the material. This is extremely surprising, given the fact that all other FeAs-based superconducting compounds exhibit bulk superconductivity upon suppression of the AFM phase [24]. We can speculate on its origin as having a localized nature tied to the low percentage rare earth substitution, but further chemical and structural characterization is required to help elucidate the origin of this phase and its potential to be stabilized in bulk form.

3.5 Phase Diagram and Discussion

Because pressure [90] and doping [91] are both effective in suppressing the AFM transition, the temperature-doping phase diagrams of the $\text{Ca}_{1-x}\text{R}_x\text{Fe}_2\text{As}_2$ series appear qualitatively similar, but in fact evolve with different concentration rates that depend on rare earth ionic size. In the $\text{Ca}_{1-x}\text{R}_x\text{Fe}_2\text{As}_2$ systems, the suppression of the AFM phase with x is similar for each species, but progresses at noticeably different rates. Extrapolating a phenomenological fit of T_N as a function of x to $T = 0$ shows this explicitly: the resultant critical concentration x_c where T_N vanishes varies with rare earth. Given the known sensitivity of the lattice parameters to the choice of rare earth species as shown by the structural characterization above, this trend verifies that, in addition to electron doping, chemical pressure also plays a role in shaping the phase diagram of the $\text{Ca}_{1-x}\text{R}_x\text{Fe}_2\text{As}_2$ system.

To disentangle the doping and pressure effects, we utilize the observations noted above about the progression of lattice constants—in particular the strong and weak dependences of a - and c -axis lattice constants, respectively, on rare earth species (see Fig. 3.2)—to characterize chemical pressure by the measured change in the c -axis unit cell dimension. For instance, substitution of La into CaFe_2As_2 does not change the c -axis unit cell length for concentrations up to almost 30% La, while Nd substitution changes the c -axis very quickly. However, for all rare earth species the a -axis length increases on average at the same rate with substitution concentration regardless of ionic size. This is possibly due to an expansion of the Fe sublattice

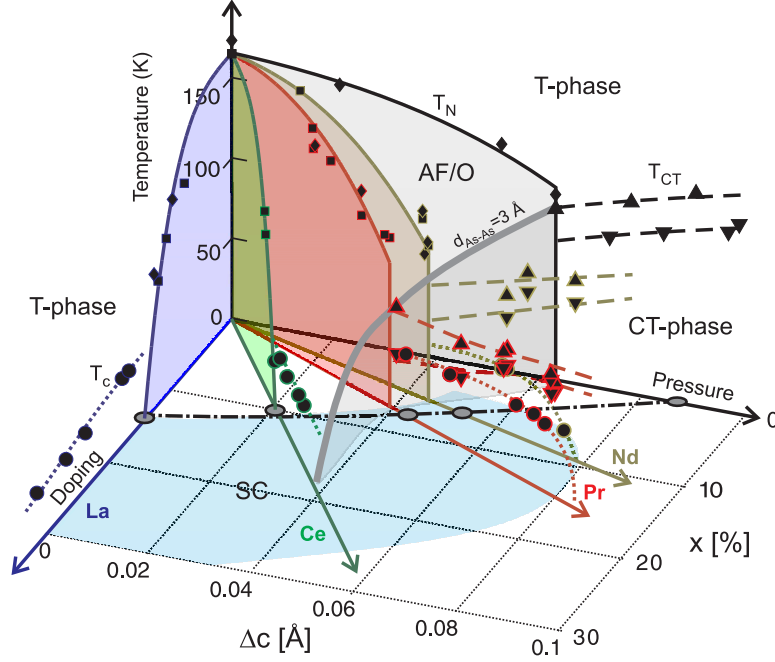


Figure 3.15: Phase diagram of $\text{Ca}_{1-x}\text{R}_x\text{Fe}_2\text{As}_2$ series showing the evolution of magnetostructural transition T_N , the appearance of superconductivity at T_c , and the isostructural collapse as a function of electron doping (x) and effective chemical pressure (Δc , the measured change in c -axis induced by doping relative to the value of undoped CaFe_2As_2 at ambient pressure). Data for $x = 0$ are taken from CaFe_2As_2 measurements under pressure [68]. Data points for the AFM transition are obtained from electrical resistivity (diamonds) and magnetic susceptibility (squares). Superconducting transitions are taken from resistivity data (circles), and collapse transitions (triangles) are from susceptibility data, indicating warming (up-triangle) and cooling (down-triangle) conditions. The solid grey line indicates the position where the interlayer As-As separation equals 3 Å, coinciding with the onset of the structural collapse for each rare earth series and for CaFe_2As_2 under pressure.

caused by charge doping with an effective adjustment of the Fe oxidation state, but such a conclusion requires verification from a core level spectroscopy experiment.

Therefore, we take the change in c -axis length as a measure of the true chemical pressure. The value of the c -axis lattice parameter at x_c for each R is then used to project the individual phase diagrams onto the x vs c -axis plane. This construction forms the basis for the universal phase diagram for $\text{Ca}_{1-x}\text{R}_x\text{Fe}_2\text{As}_2$ shown in Fig. 3.15, which extends the pressure-temperature phase diagram of CaFe_2As_2 [67, 69, 72] along a third charge-doping axis. In this manner, it is seen that the individual rare earth species phase diagrams nicely straddle the doping-pressure plane in a manner that allows access to distinct parts of the phase diagram.

Combining our transport, magnetic susceptibility and neutron scattering data enables us to trace the progression of the AFM, cT , and superconducting transitions as a function of the segregated parameters of electron doping and chemical pressure. In this way, it can be seen that the AFM phase is effectively suppressed by both doping and chemical pressure, similar to other established systems such as $\text{Ba}_{1-x}\text{K}_x\text{Fe}_2\text{As}_2$ and pressurized BaFe_2As_2 [91]. Furthermore, the AFM transition line exhibits continuity through the doping-pressure plane, demonstrating the symmetry between both methods of tuning. This is in line with ideas about band structure tuning, whereby nesting features of the Fermi surface that may stabilize the AFM phase in the parent compound are disrupted by either tuning parameter. However, the suppression of AFM order with electron doping at the alkaline earth site is in stark contrast to recent first-principles calculations that predict an

enhancement of magnetism [92], demonstrating the failure of a rigid band picture even at low charge doping.

As in undoped CaFe_2As_2 under pressure [68, 72], where the cT phase abruptly severs the continuous suppression of the AFM transition under applied pressure, the suppression of the AFM phase in $\text{Ca}_{1-x}\text{Pr}_x\text{Fe}_2\text{As}_2$ and $\text{Ca}_{1-x}\text{Nd}_x\text{Fe}_2\text{As}_2$ is also shown to be interrupted by the cT transition but at slightly lower temperatures and effective pressures. This is understood as due to the occurrence of the cT transition exactly at the 3 Å interlayer As-As separation, which follows both a pressure- and doping-dependent path through the phase diagram as marked by the solid grey line in Fig. 3.15. What is more unusual is the insensitivity of the observed high- T_c superconducting phase to this boundary, raising important questions regarding which elements of chemical, electronic and magnetic structure are important to Cooper pairing should this superconducting phase prove to be intrinsic to both the uncollapsed and collapsed structures that straddle this division.

Interestingly, high-temperature superconductivity in the $\text{Ca}_{1-x}\text{R}_x\text{Fe}_2\text{As}_2$ series appears to exist only exclusively from the AFM phase. This is strikingly similar to the segregation of SC and AFM phases found in 1111 materials doped with fluorine, such as in $\text{LaFeAsO}_{1-x}\text{F}_x$ [93] and $\text{CeFeAsO}_{1-x}\text{F}_x$ [94], and should be contrasted with the well-known coexistence shown to occur in $\text{BaFe}_{2-x}\text{Co}_x\text{As}_2$ [32, 57]. Further confirmation of the intrinsic nature of superconductivity in $\text{Ca}_{1-x}\text{R}_x\text{Fe}_2\text{As}_2$ will shed light on this interesting dichotomy, possibly providing an explanation for this distinction between phase diagrams in oxypnictide-based and intermetallic-based superconductors.

In conclusion, it has been shown that rare earth substitution into the iron-based superconductor parent compound CaFe_2As_2 provides for a rich playground of phases that will prove useful for studying various aspects of the physics of iron-based superconductivity. Depending on the choice of rare earth substituent, varying degrees of chemical pressure and electron doping can be utilized to tune both the electronic and structural phases of this system, resulting in a remarkable phase space.

It has also been shown that chemical pressure can drive CaFe_2As_2 through a structural collapse of the tetragonal unit cell that retains the crystal symmetry, but dramatically changes the bonding structure, dimensionality and electronic properties. The collapse is driven solely by the interlayer As-As p -orbital separation, which prefers to form a covalent bond when the separation is driven to less than 3 \AA by chemical substitution or applied pressure, or a combination of both. This results in an unprecedented thermal expansion of the unit cell due to this instability, and a controllable tunability of the crystal and electronic structure as a function of temperature.

Interestingly, an unprecedentedly high superconducting transition temperature was observed in all rare earth substitutions upon complete suppression of the antiferromagnetically ordered phase, with several extrinsic origins of this partial-volume-fraction phase systematically ruled out. The presence of this superconductivity, regardless of the structural collapse instability, raises important questions regarding the sensitivity of Cooper pairing in the iron-based materials to electronic structure, bonding and dimensionality, and access to this dramatic structural col-

lapse at ambient pressure conditions will provide ample opportunity to study these effects in further detail.

The following chapters will document further investigations into the nature of the superconductivity observed here. Chapter 6 is an exploration aimed at increasing the superconducting volume fraction of these materials by increasing the concentration of the rare earth ions beyond the above mentioned solubility limit. Chapter 7 investigates the nature of the superconducting phase in the light of interfacially enhanced superconducting transitions, as put forth by other investigations[95]. Finally, Chapter 8 presents a theoretical perspective on these materials invoking the breaking of ferro-orbital alignment to explain superconductivity in the collapsed phase.

Chapter 4

Enhanced Superconducting Transition Temperature in (Ba,Sr)Ni₂As₂ Solid Solutions

Although the Ca_{1-x}R_xFe₂As₂ system presents a new high- T_c class of materials, it also creates more questions than it answers. A key component of the physics of the iron-based superconductors is thought to be an electronic degeneracy[96], arising from two electrons spread out over three orbitals, which is resolved through a Jahn-Teller distortion (a tetragonal to orthorhombic transition[81, 87, 97]). In the case of the Ca_{1-x}R_xFe₂As₂ system, this is further complicated by the presence of the collapsed tetragonal state which, contrary to predictions, actually appears to coexist with high- T_c superconductivity.

Fortunately, the 122 superconductors crystallize in the ThCr₂Si₂ structure, which is shared by over 500 other materials, many of which superconduct in their own right. A similar electronic structure can be seen in the case of BaNi₂As₂ [98]. In this case, four electrons (instead of two for the iron compounds) are trying to occupy the same three electronic orbitals, resulting in a Jahn-Teller distortion from a tetragonal to a triclinic state[99, 100]. Additionally, BaNi₂As₂ is known to be a BCS-type

superconductor with a T_c of 0.7K[98]; reaching up to 3 K with the application of physical pressure[101] or chemical pressure (substituting P for As)[102].

In the same vein of materials, SrNi_2As_2 exists in the collapsed ThCr_2Si_2 structure at room temperature and ambient pressures, presenting metallic behavior and interlayer As-As bonds[103]. It also superconducts with $T_c = 0.6\text{K}$ [104]. Despite similar a -axis lattice parameters for these material, they have very different c -axis lattice parameters ($\sim 1 \text{ \AA}$ difference). Therefore, the substitution of Sr into BaNi_2As_2 on the Ba site should create a chemical pressure effect, shrinking the c -axis. According to Vegard's Law, the c -axis should continue shrinking with increasing Sr content until the interlayer As-As separation reaches the critical length for the As dimers to form, thus falling into the collapsed tetragonal state.

In this chapter, I use the endpoints BaNi_2As_2 and SrNi_2As_2 to construct solid solutions of composition $\text{Ba}_{1-x}\text{Sr}_x\text{Ni}_2\text{As}_2$. The resulting structural and physical properties are analyzed, including chemical composition, unit cell structure, resistivity, and susceptibility, all of which indicate that this is a bulk superconductor with a maximum T_c of 3.2K.

4.1 Methods

I have grown single crystals via a Pb-flux method using nominal stoichiometries of $(1-x):x:2:20$ for Ba:Sr:NiAs:Pb according to the formula $\text{Ba}_{1-x}\text{Sr}_x\text{Ni}_2\text{As}_2$ with Pb flux[98]. Starting materials were placed inside alumina crucibles and sealed in quartz tubes under partial atmospheric pressure of Ar. The growths were heated and

allowed to slow cool, then centrifuged, resulting in crystals with typical dimensions of $0.5 \times 0.5 \times 0.10 \text{ mm}^3$. I obtained chemical analysis using both energy-dispersive (EDS) and wavelength-dispersive (WDS) X-ray spectroscopy, showing 1:2:2 stoichiometry between (Ba,Sr), Ni, and As concentrations.

C-axis lattice parameters were obtained by Peter Zavalij, University of Maryland Department of Chemistry, on a Bruker Smart Apex2 diffractometer equipped with a CCD detector, graphite monochromator, and monocap collimator. Resistivity and susceptibility measurements were carried out using the techniques described in Chapter 2.

4.2 Chemical and Structural Properties

EDS of the actual concentration of Sr in the $\text{Ba}_{1-x}\text{Sr}_x\text{Ni}_2\text{As}_2$ series reveals that Sr substitution does not follow a simple linear dependence on nominal concentration (Fig. 4.1). Furthermore, the Sr concentration is in general substantially lower than the nominal starting Sr concentration. This suggests that Ba is highly preferred over Sr in the Alkaline Earth site in this series. Additionally, the measured Sr content shows obvious variation in the $0.6 \leq x \leq 0.8$ nominal concentration region. Above this region, Sr content climbs very quickly, making precise control of substitutions in this region difficult.

In order to track the evolution of the *c*-axis with increasing Sr content, x-ray measurements were performed to calculate the *c*-axis lattice parameters of the crystals. Crystals, plate-like in the *ab* plane by nature, were exposed to x-rays normal

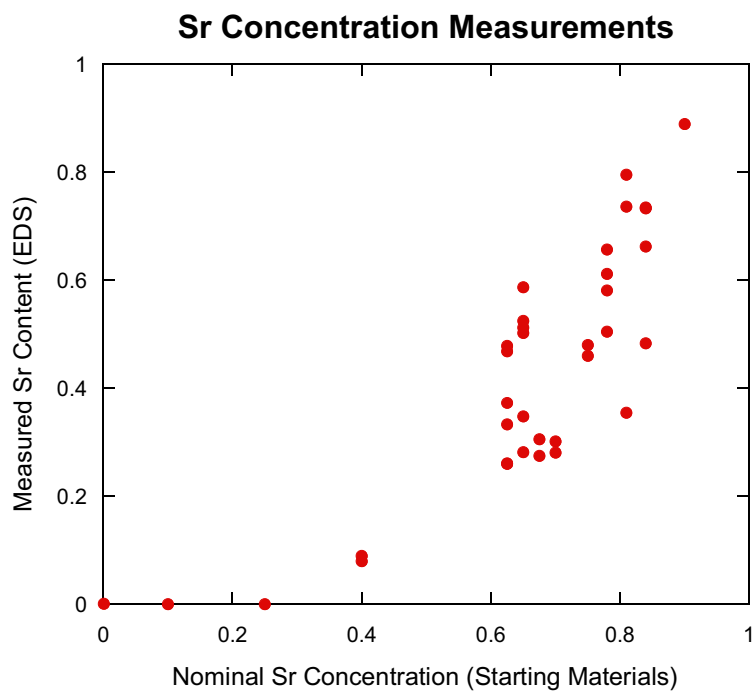


Figure 4.1: EDS measurements of Sr concentrations in Pb-flux grown crystals. The measured Sr does not follow a simple linear relationship. The uncertainty in these measurements are indicated by the size of the markers, based on the nominal limitations of our EDS set-up.

to the surface of the plate and intensities were recorded via CCD camera. Using BaNi_2As_2 and SrNi_2As_2 end-members to find the initial $(00l)$ peaks, we were able to track the movement of the peaks with increasing Sr substitution and determine the c -axis lattice parameters. As shown in Fig. 4.2, plotting the c -axis parameter against the EDS measurement of Sr content gives a very good linear relationship, allowing us to trust the values obtained in EDS with greater confidence. Further, we can determine the Sr content in crystals with Sr concentrations below the threshold of EDS by only measuring the c -axis reflections and fitting to this relationship (blue point in Fig. 4.2).

Plotting c -axis versus Sr content also shows another feature: an abrupt change in the slope of the c -axis lattice parameter, near 70% Sr. On either side of this kink, the lattice parameter evolves with Sr content in good accordance with Vegard's Law; the error also rises strongly near this concentration, indicating a structural phase transition. Below 70% Sr, we can treat our samples to good approximation as Sr-substituted BaNi_2As_2 ; above this concentration they behave as Ba-substituted SrNi_2As_2 .

4.3 Physical Properties

4.3.1 Electrical Transport and Magnetic Susceptibility

In addition to good agreement between EDS and x-ray measurements, we can also see there is good agreement with resistivity profiles (Fig. 4.3). Below 40% Sr, the tetragonal to triclinic phase transition (T_s) is seen to stay remarkably

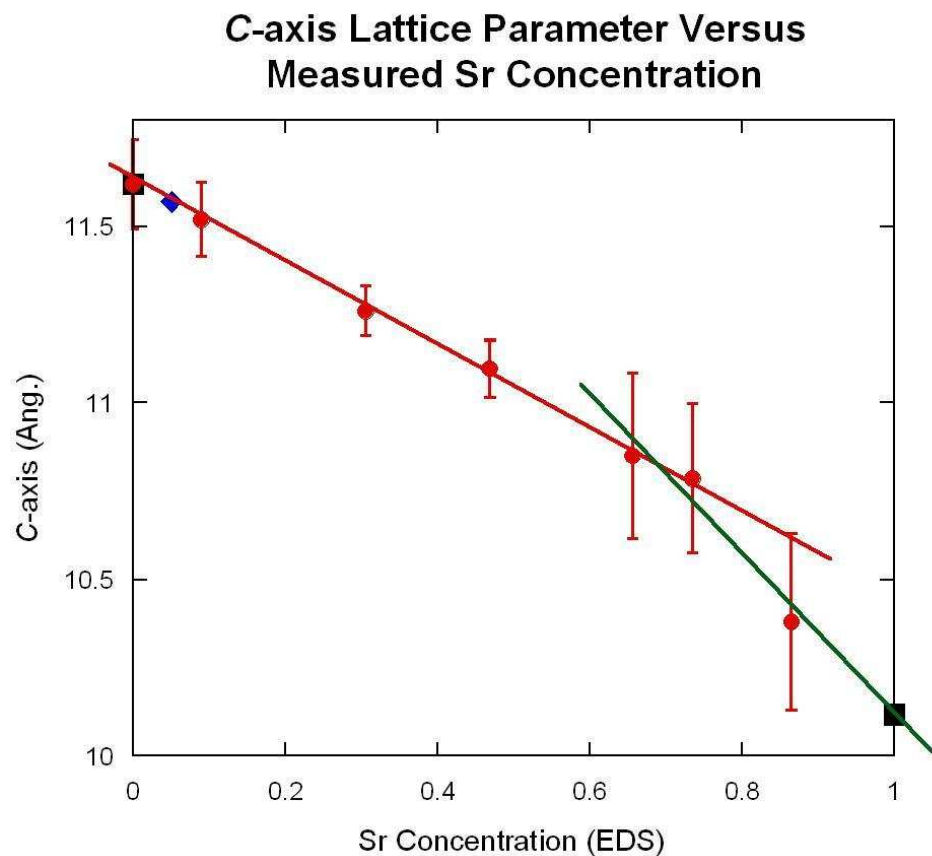


Figure 4.2: *C*-axis lattice parameters obtained via x-ray diffraction versus EDS measurements of Sr concentrations for the same crystals. Red and green lines denote BaNi₂As₂ and SrNi₂As₂ regimes, respectively. The black points are *c*-axis values for BaNi₂As₂[98] and SrNi₂As₂[104]. The blue point is a crystal with Sr content ~ 5%, below the threshold of EDS but able to be fit to x-ray data.

steady, despite a contracting unit cell. Above 60% Sr, this phase transition is no longer observed; instead, we see evidence of the structural collapse (T_{coll}) at ~ 60 K. Beyond 80% Sr, resistivity is consistent with that of SrNi₂As₂, indicating that the material is already in the collapsed state by 300K (the highest temperature used in this experiment). The interesting behavior falls in the region between 40 and 60 % Sr, where three transitions are observed: a higher temperature transition (T_s), a slightly lower temperature transition (T_{coll}), and a transition at roughly 3K. Note that while T_s is somewhat suppressed in this region, T_{coll} remains rather stable.

The 3K transition is seen to arise at $\sim 40\%$ Sr and is seen up to nearly 80% Sr. In Figure 4.4, we present data showing that this is indeed superconductivity, with a Meissner screening volume fraction of $\sim 100\%$, coinciding with the drop in resistivity. Resistivity was also remeasured using Ag-epoxy contacts rather than solder contacts to eliminate the possibility of a solder-based transition. This transition is remarkably stable over this range; rather than rising and disappearing like a dome, the transition appears step-like, with a constant maximum, only disappearing once normal SrNi₂As₂ behavior is recovered. This behavior is similar to that seen with the application of physical or chemical pressure (P-substitution) to this system, appearing at a maximum of 3.2K and then dropping again with further application of pressure[101, 102].

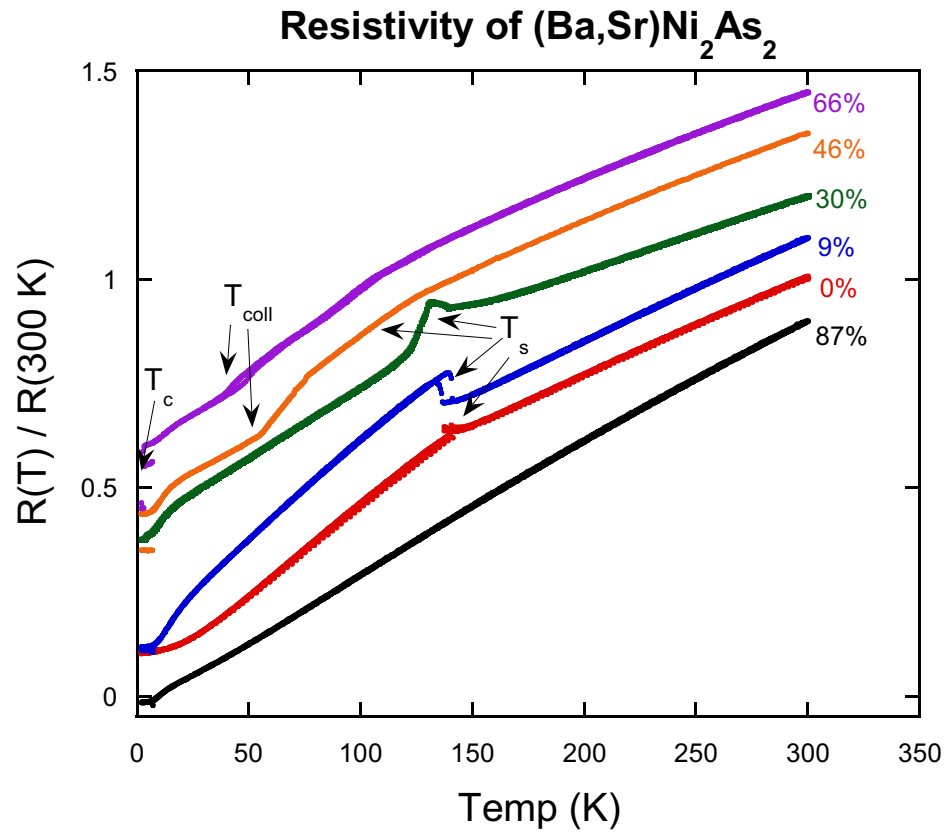


Figure 4.3: Resistivity versus temperature profiles for the key resistive regimes. Data is normalized and shifted for clarity. Sr concentration is the EDS and x-ray value. A consistent signature for T_s is seen for the region from 0 to 40% Sr. Coexistent transitions are seen in the region between 40% and 60% Sr. A T_{coll} signature is observed until 80% Sr. Above this amount, resistivity is in good agreement with that of SrNi_2As_2 .

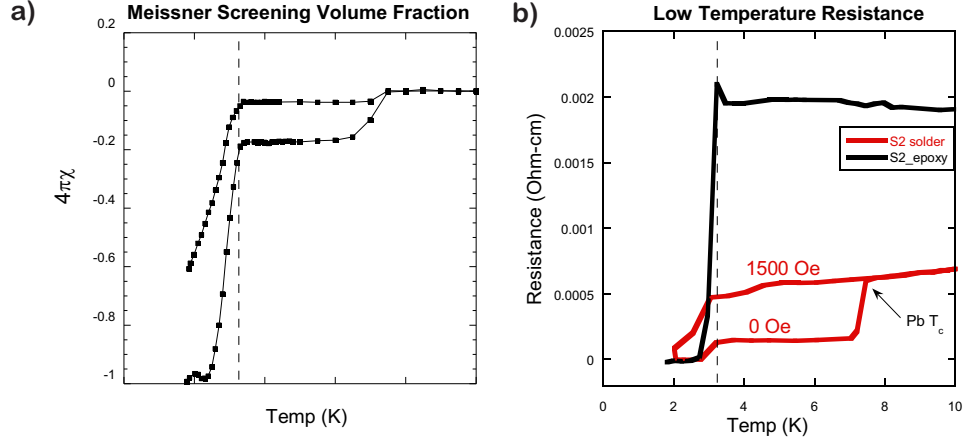


Figure 4.4: **(a)** The Meissner screening volume fraction vs. temperature. The small dip at 7.5 K is from some solder left on the surface after a resistivity measurement. The signal quickly reaches -1 below 3.2 K. **(b)** Resistivity measurements with solder contacts (red) and epoxy contacts (blue). In the case of solder contacts, a 1500 Oe field is used to suppress the superconductivity from the solder contacts, although a transition is still observed at 3.2 K. All measurements are taken on the same crystal.

4.4 Summary

These results are summarized in the phase diagram in Figure 4.5. Although we initially expected T_s to be monotonically suppressed as is seen in the cases of P-substitution and pressure work, we instead see that T_s remains stubbornly stagnant until just over 40% Sr. Another interesting finding is that T_s , T_{coll} , and T_c are seen to coexist in these samples, a feature not seen in other studies of BaNi_2As_2 . The superconductivity observed in this system at 3.2K is very close to the maximum value for all BaNi_2As_2 studies: 3.3K in the P-substituted BaNi_2As_2 [102]. However, the synthesis of these samples is more straight-forward, requiring no P and only adjusting the Ba:Sr starting ratio. The nature of the superconductivity in this

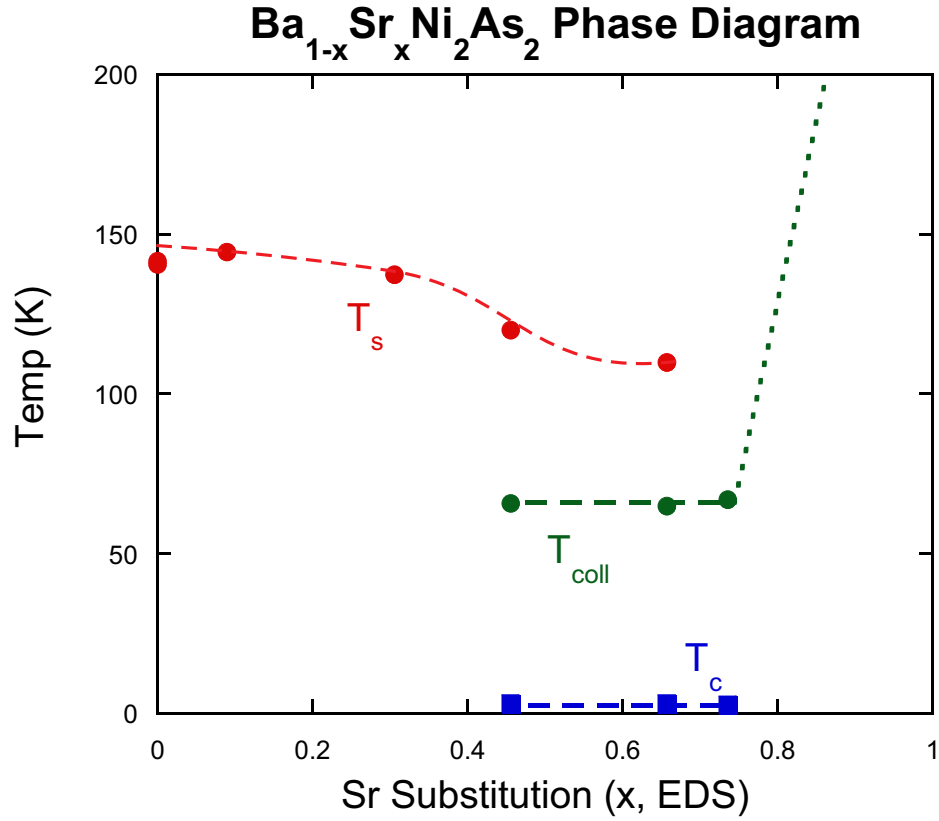


Figure 4.5: Phase Diagram vs. Temperature for the $\text{Ba}_{1-x}\text{Sr}_x\text{Ni}_2\text{As}_2$ solid solution series. T_s (red) is rather constant in temperature until the emergence of T_{coll} (green). A coexistence region is observed with T_s , T_{coll} , and T_c all being observed. At slightly higher Sr, T_s is suppressed and only T_{coll} and T_c remain. At very high Sr concentrations, the Fermi-liquid behavior of SrNi_2As_2 is recovered.

system is assumed to be the same as the phonon-softening seen in the P-substituted materials; however, further study is needed to positively conclude this.

Chapter 5

Rare earth substitution in lattice-tuned $\text{Sr}_{0.3}\text{Ca}_{0.7}\text{Fe}_2\text{As}_2$ solid solutions

Portions of this chapter have been summarized or paraphrased from my publication:

Tyler B Drye, Shanta R Saha, Johnpierre Paglione, and Peter Y Zavalij, “Rare earth substitution in lattice-tuned $\text{Sr}_{0.3}\text{Ca}_{0.7}\text{Fe}_2\text{As}_2$ solid solutions” *Superconductor Science and Technology* **25** 084014 (2012) Ref. [4]

With a deeper understanding of the role that the collapse transition plays in these compounds, I will now turn my attention to the other major problem in the $\text{Ca}_{1-x}\text{R}_x\text{Fe}_2\text{As}_2$ compounds: the low volume fraction of the superconducting phase. One route to increasing this volume fraction is through the inclusion of higher concentrations of rare earth atoms. Previous studies of La substitution into the SrFe_2As_2 system [78], with T_c values up to ~ 22 K, have shown a significant increase in the superconducting volume fraction when La content reaches 40% La for Sr, at which point the volume fraction jumps to nearly 70%. The introduction of

higher concentrations of rare earth in the CaFe_2As_2 series is thus a promising route to achieving bulk superconductivity with high T_c values. Expanding the unit cell via choice of alkaline earth species is one possible method of facilitating an increase in concentration of rare earth, in particular for the $\text{Ca}_{1-x}\text{La}_x\text{Fe}_2\text{As}_2$ series, which exhibits a slight volume increase (*i.e.*, constant c -axis but increasing a -axis) upon increasing La concentration up to the solubility limit of $\sim 30\%$ [1].

In this chapter, I examine the feasibility of increasing the solubility limit of rare earth substitution by doping La into the $(\text{Sr,Ca})\text{Fe}_2\text{As}_2$ solid solution system. To avoid the necessity of stabilizing the substitution via high-pressure synthesis techniques, as required to substitute La into the SrFe_2As_2 system [78], we make use of an intermediate solid solution of $\text{Sr}_{0.3}\text{Ca}_{0.7}\text{Fe}_2\text{As}_2$ where the inclusion of a fraction of Sr expands the unit cell according to Vegard's Law in a controllable manner [66]. The synthesis of such single crystals with La substitution shows widely ranging chemical compositions and suggests a competition between Sr and La. We detail the effects of increasing La content using systematic X-ray, electrical transport, and magnetization measurements, and compare these effects with those observed when La is doped into the CaFe_2As_2 parent material, specifically tracking the suppression of the AFM ordering temperature and signs of superconductivity in the system.

5.1 Methods

I have grown single crystals via a self-flux method using elemental stoichiometries of $(1 - y)(1 - x):y(1 - x):x:4$ for Sr:Ca:La:FeAs according to the formula

$(\text{Sr}_{1-y}\text{Ca}_y)_{1-x}\text{La}_x\text{Fe}_2\text{As}_2$ with FeAs flux [77]. Starting materials were placed inside alumina crucibles and sealed in quartz tubes under partial atmospheric pressure of Ar. The growths were heated and allowed to slow cool, resulting in crystals with typical dimensions of $(5.0 \times 5.0 \times 0.10)$ mm³, which were mechanically separated from the frozen flux. Chemical analysis was obtained using both energy-dispersive (EDS) and wavelength-dispersive (WDS) X-ray spectroscopy, showing 1:2:2 stoichiometry between (Sr,Ca,La), Fe, and As concentrations. EDS was conducted on a large number of samples in order to determine general concentration trends, while WDS was used to determine very accurately the concentrations of elements for samples used in X-ray, resistivity, and magnetization measurements. Single crystal X-ray diffraction was performed by Peter Zavalij (University of Maryland Department of Chemistry).

5.2 Chemical and Structural Properties

EDS of the actual concentration of La in the $(\text{Sr}_{1-y}\text{Ca}_y)_{1-x}\text{La}_x\text{Fe}_2\text{As}_2$ series reveals that at low La values, the actual La content is higher than the nominal content, rising to a limit of $\sim 30\%$ for growths with nominal La higher than 50% as shown in Fig. 5.1a. While it is illustrated that increasing the starting ratio of Ca:Sr leads to higher La concentrations in the final materials, a stronger correlation between the Sr, Ca, and La concentrations can be found by plotting the measured La content against the measured Sr content as shown in Fig. 5.1b. It is evident here that La and Sr are inversely correlated in this material and increasing the Sr

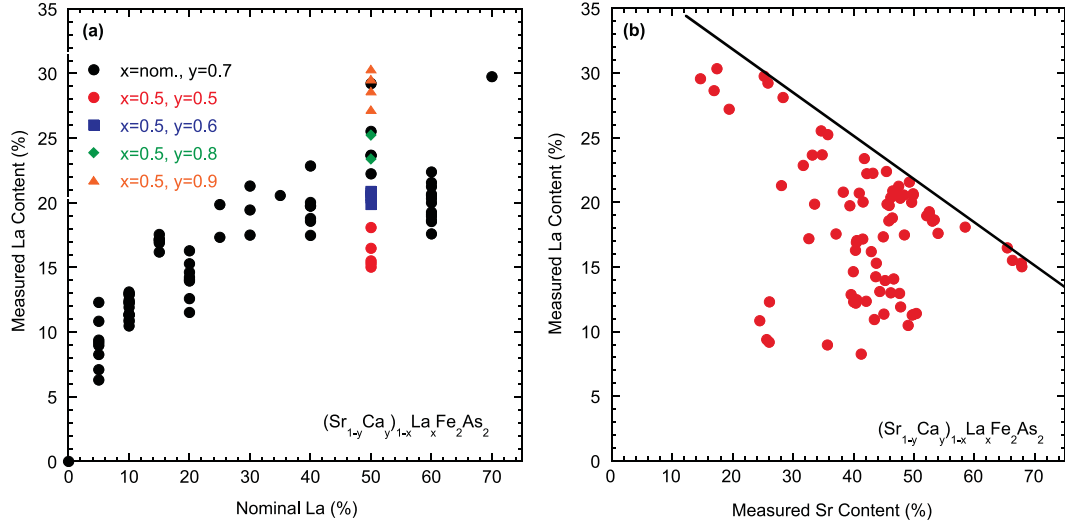


Figure 5.1: Results of energy dispersive spectroscopic (EDS) analysis of the elements occupying the alkaline earth site. (a) Measured (actual) La content vs. Nominal (pre-reaction) La content. Black closed circles represent samples with pre-reaction stoichiometries of $(\text{Sr}_{0.3}\text{Ca}_{0.7})_{1-x}\text{La}_x\text{Fe}_2\text{As}_2$. Colored symbols represent samples with pre-reaction stoichiometries of $(\text{Sr}_{1-y}\text{Ca}_y)_{1-x}\text{La}_x\text{Fe}_2\text{As}_2$, where y is denoted in the legend. (b) Measured La content vs. measured Sr content in the same samples shown in a. All values are taken from EDS analysis. The black solid line serves as the upper bound for the solubility of La.

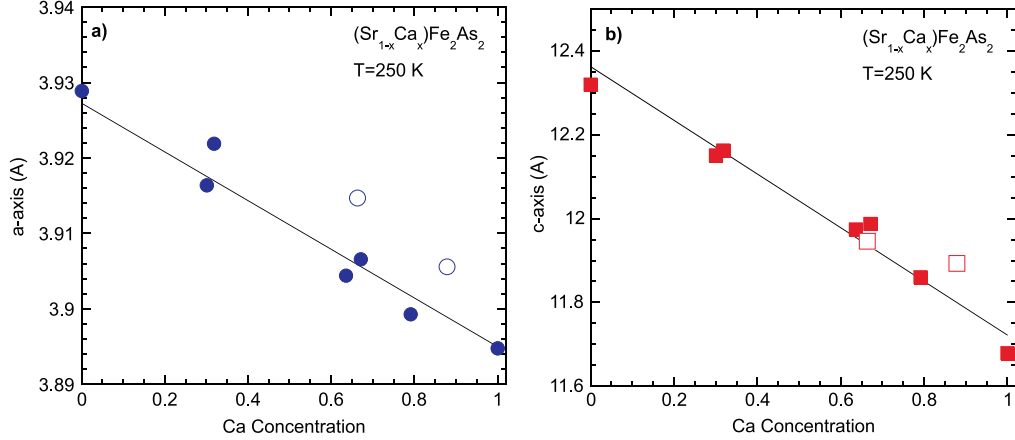


Figure 5.2: Unit cell parameters a and c obtained via single crystal x-ray diffraction of $(\text{Sr,Ca})\text{Fe}_2\text{As}_2$ (filled points) [66] and $(\text{Sr,Ca,La})\text{Fe}_2\text{As}_2$ (open points) are presented in **a** and **b**, respectively. The c -axis lattice parameters are in good agreement, but the a -axis lattice parameters move away from the established trend as the amount of La increases.

concentration seems to strongly limit the amount of La that is able to dope into the sample.

Single crystal x-ray analysis allows us to analyze the progression of the lattice parameters as a function of the concentrations of Sr, Ca, and La in each sample. In Fig. 5.2, we plot the lattice parameters of the samples used in this study alongside the lattice parameters observed for solid solutions of the parent compounds SrFe_2As_2 and CaFe_2As_2 [66]. Previously, it was shown that doping La for Ca in CaFe_2As_2 results in a c -axis lattice parameter that does not change, despite expansion of the a -axis [1]. Taking this into account, we have plotted these points as $\text{Sr}_{1-x}(\text{Ca,La})_x$ — the Ca and La values are taken together in order to determine the composition x , which places our points in good agreement with the c -axis values from the $\text{Sr}_{1-x}\text{Ca}_x\text{Fe}_2\text{As}_2$ study (Fig. 5.2b); however, the a -axis values diverge as

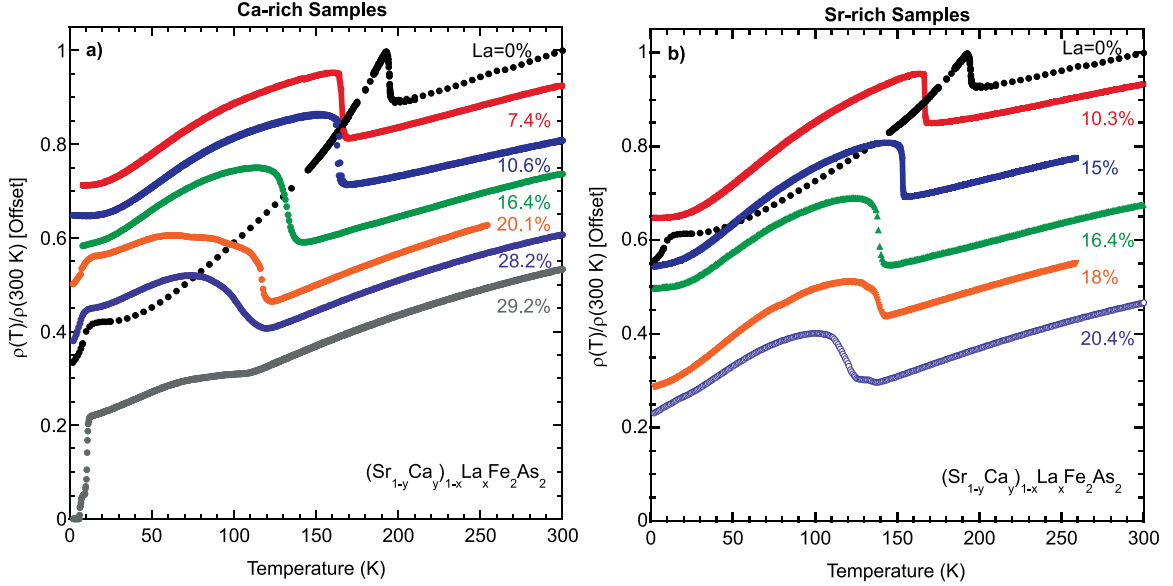


Figure 5.3: Resistivity of $(\text{Sr,Ca,La})\text{Fe}_2\text{As}_2$ samples as a function of temperature, normalized to 300 K and then vertically shifted for clarity; the Ca-rich samples are presented in **a**, while the Sr-rich samples are presented in **b**.

La content increases (Fig. 5.2a). This implies that by selecting the proper Sr, Ca, and La content, we can tune the a -axis and c -axis parameters nearly independently. This is in striking contrast to most doping studies on these materials, which show a strong coupling between a and c -axes lattice parameters [105].

5.3 Transport and Magnetization

As seen in similar doping studies of iron-pnictides [1, 58, 78], it is expected that increasing the La content in these samples will be manifest in resistivity data as a systematic decrease in the Neél ordering temperature T_N . Electrical resistivity

data of these samples (shown in Fig. 5.3) roughly resembles the expected behavior, as it is obvious that T_N is suppressed upon increased doping of La into the system.

A key difference here lies in the ranging chemical compositions obtained using WDS; subtraction of the La content leaves two classes of samples, *i.e.* the Ca-rich (shown in Fig. 5.3a) and the Sr-rich (shown in Fig. 5.3b). In the Sr-rich case, no sample was found to contain less than $\sim 10\%$ La or more than $\sim 22\%$ La, whereas in the Ca-rich case, a much wider range of La concentrations can be found (up to $\sim 30\%$ La). In the Sr-rich samples, T_N is gradually suppressed down to ~ 130 K and no superconductivity is found to exist due to La substitution. In the Ca-rich case, T_N is suppressed to a slightly lower value of ~ 100 K, but there is no trace of a superconducting phase similar to that seen in the $\text{Ca}_{1-x}\text{La}_x\text{Fe}_2\text{As}_2$ case [1], where high- T_c values in the range 30-47 K are indicative of rare earth doping-induced superconductivity. Note that the Ca-rich samples do exhibit traces of a superconductivity onset near $T^* \sim 10$ K, which we attribute to the strain-induced phase often observed under non-hydrostatic pressure conditions [67, 69] and posited to nucleate at AFM domain walls [106]. It is interesting to highlight the fact that this “10 K” phase appears predominantly in Ca-rich samples, suggesting its stability is tied strictly to the CaFe_2As_2 magnetic and/or crystallographic structure.

Temperature dependence of magnetic susceptibility $\chi(T)$ data for Ca-rich samples (shown in Fig. 5.4) corroborates the picture drawn by electrical transport data. As expected from previous studies, T_N is revealed as an antiferromagnetic ordering temperature traced by a kink in $\chi(T)$. The suppression of T_N occurs at the same rate observed in transport data, with ordering at ~ 100 K still present for

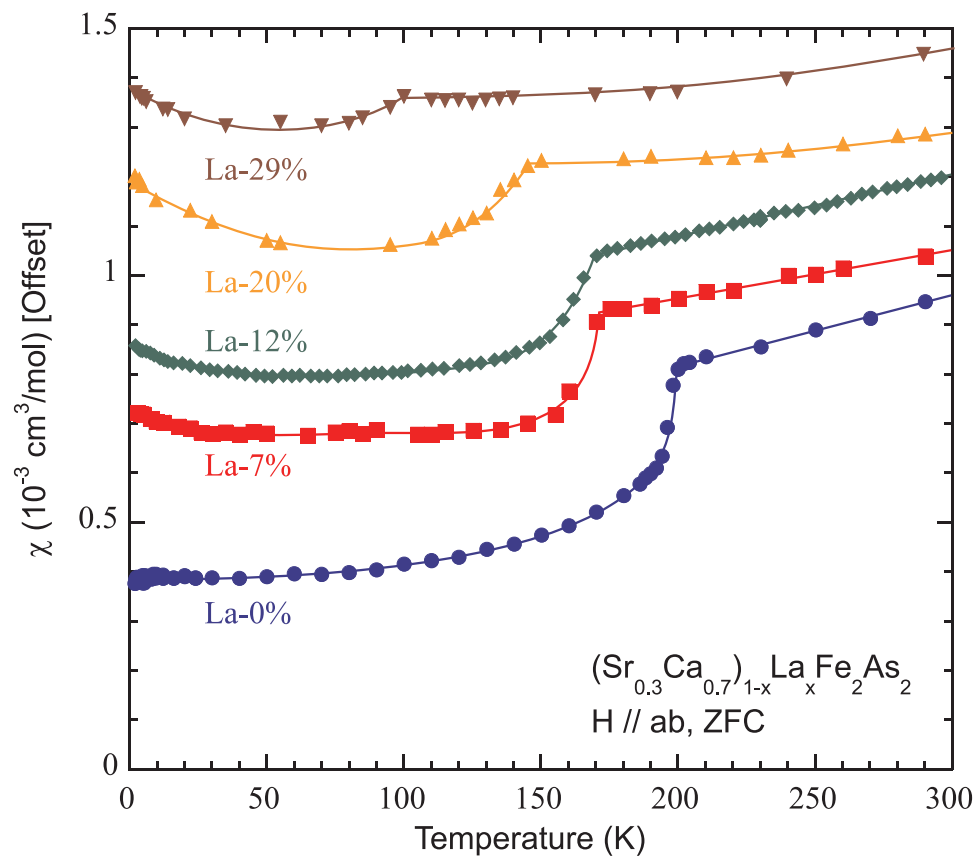


Figure 5.4: Magnetic susceptibility (χ) vs. temperature for several La doped samples. The data are shifted along the vertical axis for clarity. The kink in each curve indicates the temperature of the antiferromagnetic transition, T_N .

samples which show superconductivity at $T^* \sim 10$ K (not shown) at low field. The Meissner screening fraction of the ~ 10 K superconductivity of this sample is still seen to be relatively small, of the order of 10%. A slight Curie tail is observed in the highly-doped La samples at low temperatures, similar to that observed in $\text{Ca}_{1-x}\text{La}_x\text{Fe}_2\text{As}_2$ samples [1], which may arise from paramagnetism associated with the FeAs lattice.

5.4 Summary and Phase Diagram

Fig. 5.5 presents a proposed phase diagram for the $(\text{Sr}_{1-y}\text{Ca}_y)_{1-x}\text{La}_x\text{Fe}_2\text{As}_2$ system in comparison with that of the $\text{Ca}_{1-x}\text{La}_x\text{Fe}_2\text{As}_2$ system [1]. As shown in Fig. 5.5b, a key observation in $(\text{Sr}_{1-y}\text{Ca}_y)_{1-x}\text{La}_x\text{Fe}_2\text{As}_2$ is the absence of the high T_c superconducting phase, which is observed ubiquitously in the rare-earth doped CaFe_2As_2 materials upon suppression of the AFM phase, despite a similar electron doping scheme. The lack of a high- T_c superconducting phase in $(\text{Sr}_{1-y}\text{Ca}_y)_{1-x}\text{La}_x\text{Fe}_2\text{As}_2$ samples with La concentrations more than sufficient to induce superconductivity in $\text{Ca}_{1-x}\text{La}_x\text{Fe}_2\text{As}_2$ (Fig. 5.5a) suggests that a scenario where the superconducting phase arises solely from the presence of sufficient rare earth atoms that presumably cluster or percolate in some manner is improbable. The persistence of AFM order up to high concentrations of La may play a role here, as it seems as though high T_c superconductivity competes with AFM order and does not emerge until the complete suppression of magnetic ordering. Indeed, in every other rare-earth substituted 122 system, 30+ K superconductivity and antiferromagnetism are never

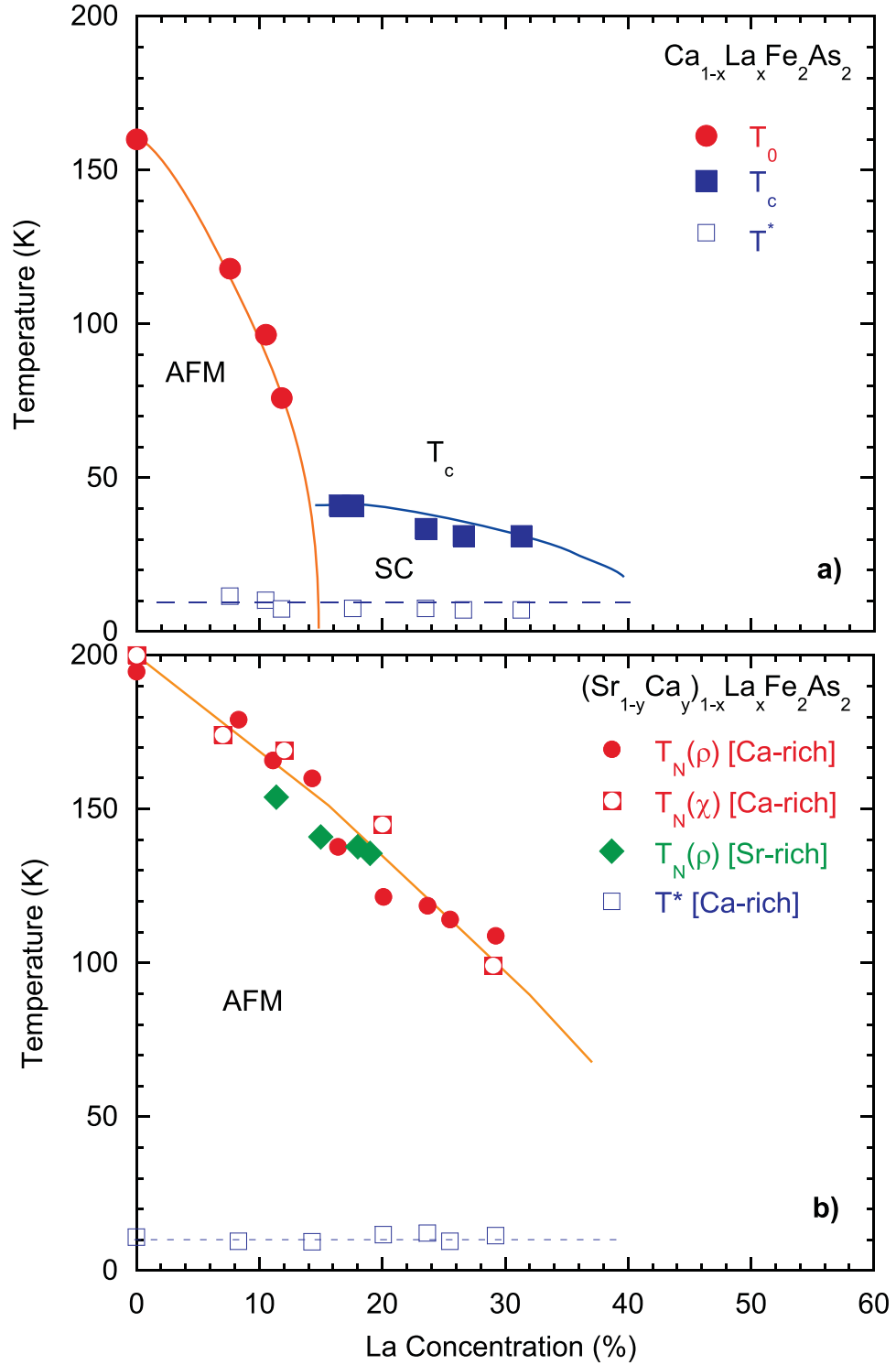


Figure 5.5: (a) The phase diagram for the $\text{Ca}_{1-x}\text{La}_x\text{Fe}_2\text{As}_2$ system [1], where high T_c superconductivity is induced on the border of AFM order and coexists with the $T^* \sim 10$ K superconducting phase. (b) Suggested phase diagram for the $(\text{Sr}_{1-y}\text{Ca}_y)_{1-x}\text{La}_x\text{Fe}_2\text{As}_2$ system. The solid and broken lines are guides to the eye.

found to coexist [1]. This agrees with the occurrence of the highest T_c in the 1111 iron-pnictide family [24, 107], indicating that the highest T_c superconducting phase and magnetic ordering may be mutually exclusive. Of course, further investigation will be necessary to bear out such a result. However, the conspicuous absence here of the high T_c phase, which has been thought to be an impurity phase of ReOFeAs, despite similar growth techniques and materials, lends credence to the idea that it is in fact intrinsic to the rare-earth substituted CaFe_2As_2 system.

In summary, we have studied the effect of electron doping by La substitution on $(\text{Sr}_{1-y}\text{Ca}_y)_{1-x}\text{La}_x\text{Fe}_2\text{As}_2$ solid solutions by growing single crystals. We have constructed a phase diagram based on transport, magnetic susceptibility and structural characterization. Chemical analysis indicates a strong inverse correlation between Sr and La. Nonetheless, independent tunability of the a - and c -axis lattice parameters can be achieved. The Sr-rich and Ca-rich regions show differing behavior; in Ca-rich samples, antiferromagnetic ordering is found to coexist with superconductivity at $T^* \sim 10$ K with a volume fraction $\sim 10\%$. But, in contrast to the CaFe_2As_2 parent compound, in neither case is T_N fully suppressed and no high- T_c superconducting phase is observed, placing the constraint that complete suppression of AFM order is a necessary condition for the latter phase, which may provide an important clue for the superconducting pairing in the iron-superconductors.

Chapter 6

High-Pressure Synthesis and Characterization of Pr-doped CaFe_2As_2

Although the previous experiments involving La-doping a solid solution did provide key insights into the nature of the superconductivity in the $\text{Ca}_{1-x}\text{R}_x\text{Fe}_2\text{As}_2$ system, they did not achieve the key objective: to examine the superconducting characteristics of $\text{Ca}_{1-x}\text{R}_x\text{Fe}_2\text{As}_2$ materials doped beyond the width-of-formation limitation. For this reason, the synthesis of $\text{Ca}_{1-x}\text{R}_x\text{Fe}_2\text{As}_2$ materials under high-pressure conditions proved to be the most likely method to break through the solubility limit, as shown in a previous report [78].

On the other hand, recent investigations offer evidence that the high T_c seen in these materials is the result of Pr defects within the crystal [108]. Their work suggests that a large band gap anomaly, consistent with the superconductivity of this system and other 122 systems, exists in Pr-rich sites throughout the material. Moving away from these sites, a smaller gap is seen nearby to Pr-rich defects, and far enough away from those regions, no band gap exists. If these claims are correct, then increasing the Pr content of $\text{Ca}_{1-x}\text{Pr}_x\text{Fe}_2\text{As}_2$ should result in more Pr defects, creating a higher shielding fraction in these samples while sustaining the high- T_c superconducting phase.

In order to investigate these effects in CaFe_2As_2 , as well as other claims about this system, single crystals of rare earth-doped CaFe_2As_2 have been grown under applied pressures up to 3 GPa. As the previous work asserts that pressure growth was most likely successful due to the smaller ionic radius of La than Sr[78], we chose to use Pr as the dopant because its ionic radius is slightly smaller than Ca, whereas La is slightly larger[79]. These crystals are characterized, and a full phase diagram of the $(\text{Ca,Pr})\text{Fe}_2\text{As}_2$ system is presented.

6.1 Methods

In collaboration with Valentin Taufour and the group of Paul Canfield, single crystals of $\text{Ca}_{1-x}\text{Pr}_x\text{Fe}_2\text{As}_2$ were grown at Iowa State University in Ames, Iowa via self-flux method using a Rockland cubic-anvil press to apply quasi-hydrostatic pressure throughout the growth process. A mixture of elemental Pr, Ca, and FeAs in the stoichiometry $1 - x : x : 4 : 4$ for Ca:Pr:Fe:As was loaded into an alumina crucible and capped with boron nitride. The crucible was loaded into the Rockland furnace, pressure was applied, and the sample was heated to 1500°C . The pressure applied during the growth process reached nearly 3 GPa at maximum temperature. After removing the sample from the furnace, single crystals were mechanically extracted from the solidified flux, with typical dimensions of $0.5 \times 0.5 \times 0.01\text{mm}^3$. For annealing, crystals were sealed in a quartz ampoule and heated to the specified temperature. Afterwards, the ampoule was removed from the furnace and cooled to room temperature in ambient conditions.

Chemical composition was obtained using wave-length dispersive spectroscopy (WDS) and energy-dispersive spectroscopy (EDS). Structural analysis was obtained through X-ray diffraction, measuring the 002 and 008 peaks in order to obtain the c -axis lattice constant, as in previous reports[40]. Single crystal X-ray diffraction was obtained by Peter Zavalij in the Department of Chemistry at the University of Maryland. Resistivity, susceptibility, and Hall Effect measurements were taken as discussed in Chapter 2.

6.2 Chemical and Structural Characterization and Annealing Effects

Table 6.1 shows the crystallographic parameters for an annealed crystal of CaFe_2As_2 doped with 39% Pr for Ca taken via single crystal X-ray diffraction. The internal structure of the unit cell is very similar to what has been found for other $\text{Ca}_{1-x}\text{R}_x\text{Fe}_2\text{As}_2$ crystals[1]. This data is plotted alongside c -axis diffraction data for the as-grown and annealed crystals in Fig. 6.1. The single crystal data (blue) extrapolates linearly from the single crystal X-ray data taken previously on ambient-pressure growth crystals. In addition, X-ray data collected at room temperature on ambient pressure growth crystals falls nicely along the trend established by annealing the high pressure growth crystals (black squares, [1]). These data indicate the good continuity of the studies and reflect the robust nature of the phase to different growth techniques.

The c -axis for the as-grown crystals is far smaller than what is observed in crystals grown under ambient pressure conditions. Importantly, WDS on these

Table 6.1: Full crystallographic data, determined by single-crystal x-ray diffraction, for a sample of $\text{Ca}_{0.61}\text{Pr}_{0.39}\text{Fe}_2\text{As}_2$ annealed at 400°C . Data was taken under nitrogen flow at a temperature of $\sim 250^\circ\text{C}$, with an uncertainty of $\pm 5^\circ\text{C}$.

Space group	I4/mmm
$a(\text{\AA})$	3.9243(17)
$b(\text{\AA})$	= a
$c(\text{\AA})$	11.501(5)
$V(\text{\AA}^3)$	177.12(17)
Z	2
Density(g/cm^3)	6.393
Refl.collected	1175
Independent refl.	100
R_{int} (%)	3.45
wR_2 , all refl.	8.34
R_1 , $I \geq 2\sigma I$	3.88
Atomic parameters:	
Pr occupation factor	0.39
Ca/Pr	$2a(0,0,0)$
Fe	$4d(0,1/2,1/4)$
As	$4e(1/2,1/2,z)$ $z=0.36656(17)$
Atomic displacement parameters U_{eq} (\AA^2):	
Ca1/Pr1	0.0126(8)
Fe1	0.0150(6)
As1	0.0127(5)
Bond lengths (\AA):	
Ca/Pr-As	$3.1711(14) \times 8$
Fe-As	$2.3763(13) \times 4$
Fe-Fe	$2.7749(12) \times 4$
Bond angles (deg):	
As-Fe-As	$111.32(8) \times 2$ $108.55(4) \times 4$
Fe-As-Fe	$71.44(4) \times 4$

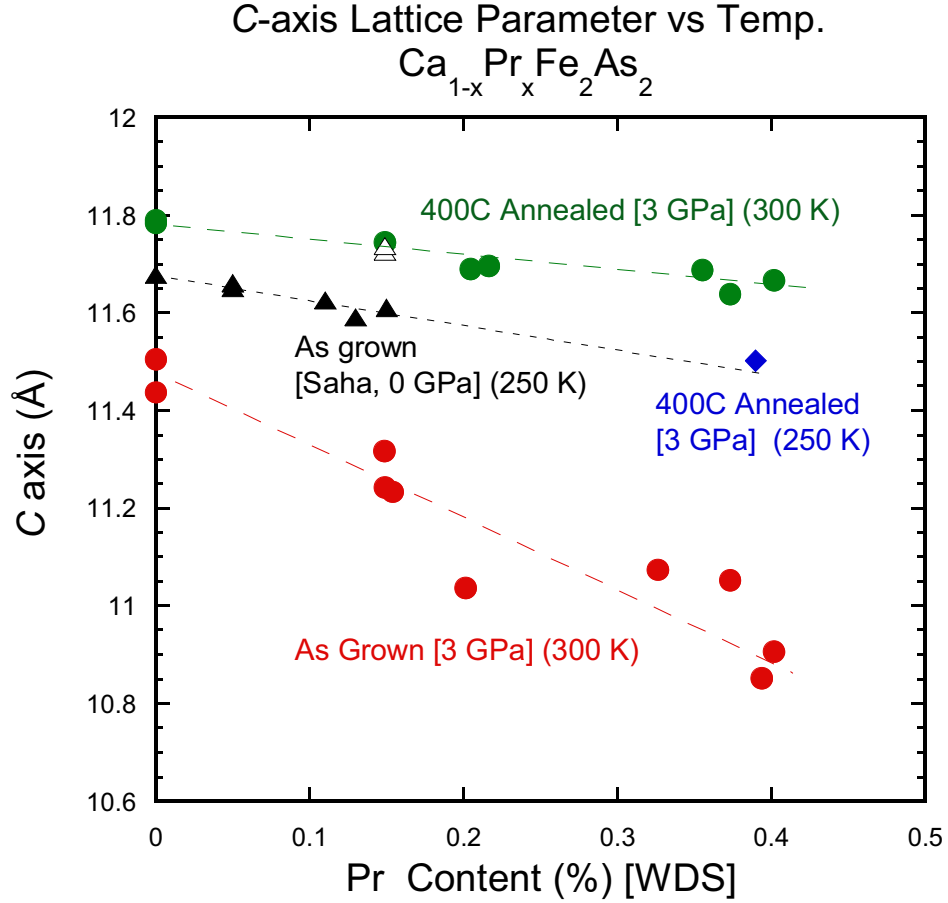


Figure 6.1: c -axis vs. WDS-measured Pr concentration for as-grown (red) and annealed (green) crystals of $\text{Ca}_{1-x}\text{Pr}_x\text{Fe}_2\text{As}_2$ synthesized under high pressure. The blue point represents the single crystal data from Table 6.1. Also plotted are single crystal data from ambient pressure growth crystals, taken at 250 K (black triangles). The open black triangles on the green line are from a batch grown at University of Maryland and then annealed with the pressure-growth samples to make a comparison between crystals used in this study and those used in Chapter 3. The lines serve as guides and are not indicative of a fit.

samples confirms Pr levels up to 40% in several crystals. As shown in Fig. 6.2, the resistivity behavior of the as-grown crystals looks like a simple metal, often with a transition similar to the one seen in FeAs. After annealing at 400°C for 3 days, we recover the resistivity behavior more consistent with the earlier reports on $\text{Ca}_{1-x}\text{Pr}_x\text{Fe}_2\text{As}_2$ [1]. Post-annealing X-ray data also shows that the c -axis lattice constant is recovered and, in fact, becomes larger than the lattice constant of ambient pressure grown crystals. This is important in determining the structural features of the phase diagram.

6.3 Superconductivity

Fig. 6.3 presents the resistivity data of various samples from the series, in the temperature region below 50 K. Here we can see transitions with a maximum of 42 K (onset) at the 14% doping level. As doping increases, the maximum transition decreases in temperature. With doping near 40%, the maximum transition temperature has been suppressed down to an onset temperature of 17 K. An important feature to notice here is that none of these transitions reach 0 Ω , much like the superconducting transitions seen in the ambient pressure grown crystals, attributed to very small volume fractions[1]. H_{c2} (Fig. 6.4) also matches quite well with the ambient pressure grown crystals.

To determine the shielding fraction of these transitions, magnetization was run at low fields (10 Oe), but bulk shielding was not observed. Due to the small size of the crystals, it is not possible to estimate the shielding volume, although

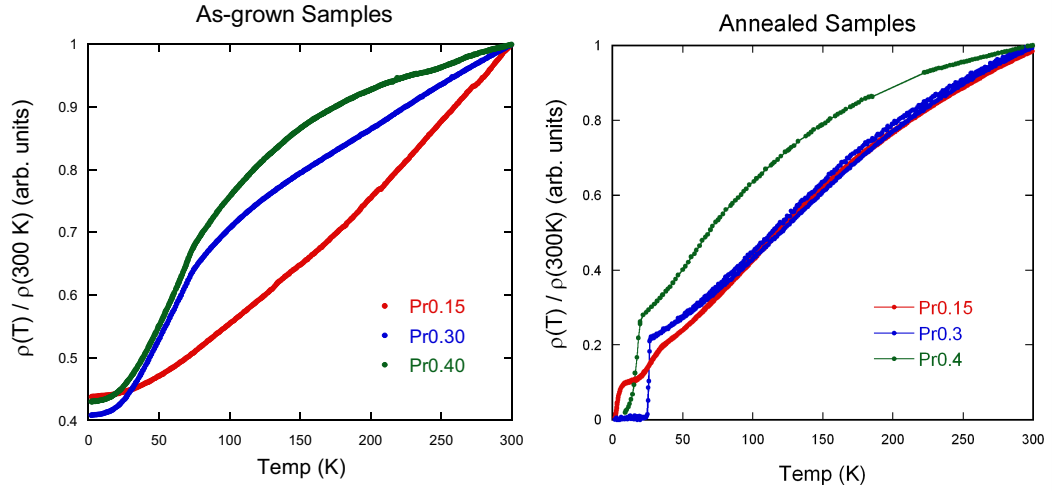


Figure 6.2: Resistivity data of as-grown (left) and annealed (right) crystals. The as-grown crystals indicate metallic-like behavior and some show a transition at 71K, consistent with the resistive anomaly in pure FeAs. Annealed crystals display behavior consistent with the 122 family and also show superconducting transitions. This is consistent with FeAs impurities in quenched samples coalescing during annealing, as presented in reference [40].

Normalized Resistivity of $\text{Ca}_{1-x}\text{Pr}_x\text{Fe}_2\text{As}_2$ Crystals

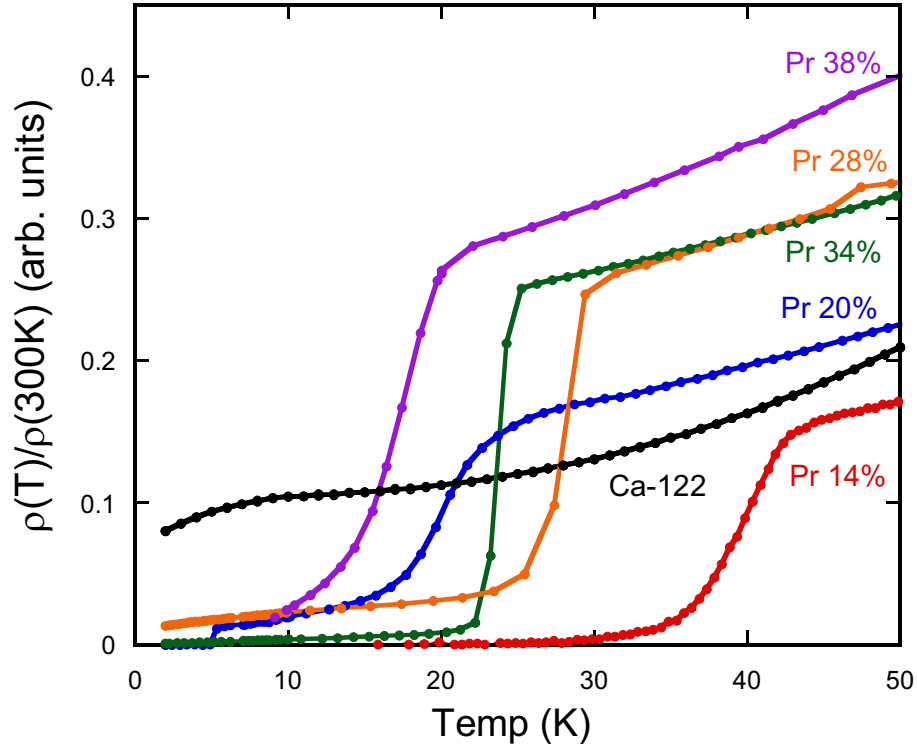


Figure 6.3: Resistivity data of annealed crystals of $\text{Ca}_{1-x}\text{Pr}_x\text{Fe}_2\text{As}_2$ grown under applied pressure. All data is from crystals grown under pressures near 3 GPa, and annealed at 400°C for 3 days. The only sample showing T_c over 40 K contains 14% Pr, consistent with previous studies that high T_c emerges near the 13% – 15% range in the $\text{Ca}_{1-x}\text{Pr}_x\text{Fe}_2\text{As}_2$ series. At higher dopings, no trace of the high T_c phase is evident.

H_{c2} Sweeps and WHH Approximation

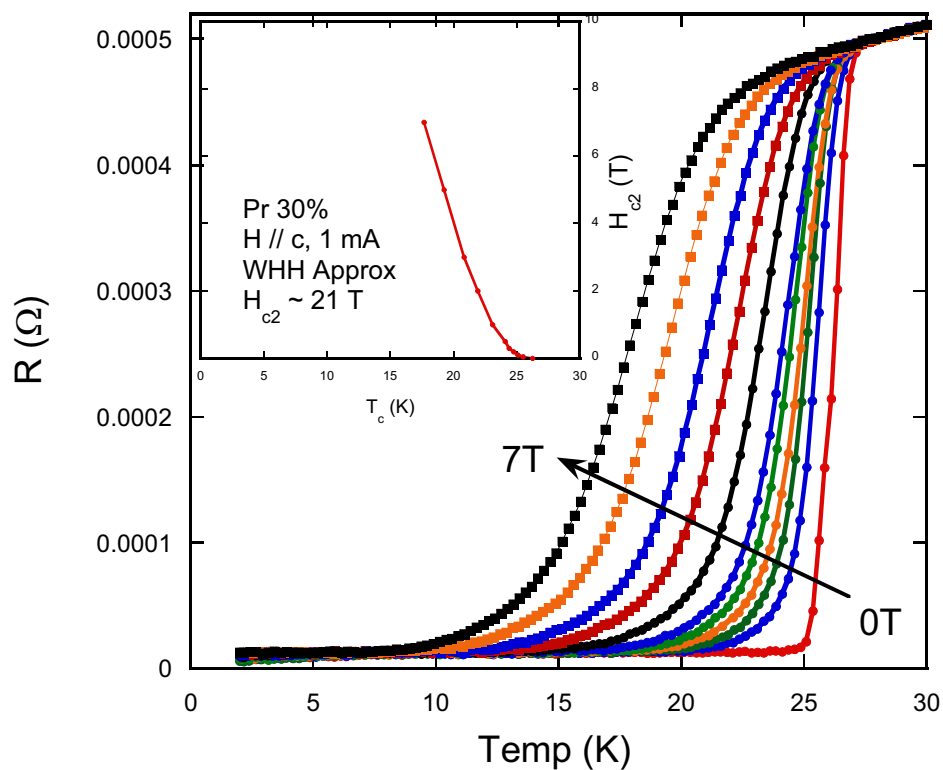


Figure 6.4: H_{c2} sweeps and the WHH approximation (inset) for an annealed $\text{Pr}_{0.3}\text{Ca}_{0.7}\text{Fe}_2\text{As}_2$ crystal grown under high pressure. The WHH approximation gives H_{c2} for this crystal as 21 T, consistent with findings on other $\text{Ca}_{1-x}\text{R}_x\text{Fe}_2\text{As}_2$ systems.

no measurable diamagnetic signal was observed. Due to the similarity in onset temperatures, we attribute these transitions to the same small volume fraction superconductivity originally reported in these materials[1, 109, 110]. However, the lack of any bulk shielding even up to very high doping levels stands in stark contrast to the behavior seen in $\text{Sr}_{1-x}\text{La}_x\text{Fe}_2\text{As}_2$.

6.4 The Collapse Transition

Also important in the $\text{Ca}_{1-x}\text{Pr}_x\text{Fe}_2\text{As}_2$ system is the abrupt transition to a “collapsed” tetragonal state. In ambient growth crystals, this transition is seen to occur upon cooling the crystal below 60 K and displays a large thermal hysteresis (see Fig. 3.10d). Magnetization has proven to be a sensitive probe of this transition. Fig. 6.5 shows the magnetization of several samples at high fields. Only one sample shows any transition. Moreover, these samples show a negative slope throughout the whole temperature scale, quite opposite to what is seen in the ambient pressure growth crystals (which show a positive slope above the collapse transition).

For a more sensitive probe of the collapsed tetragonal state, we conducted Hall effect measurements, which are very sensitive to any electronic reorganization (Fig. 6.6). Two crystals at lower and higher dopings reveal no change in Hall effect at a temperature commensurate with the collapse tetragonal transition. Taking into account the c -axis lattice constants from Fig. 6.1, it appears as though the collapsed tetragonal transition has been annealed away.

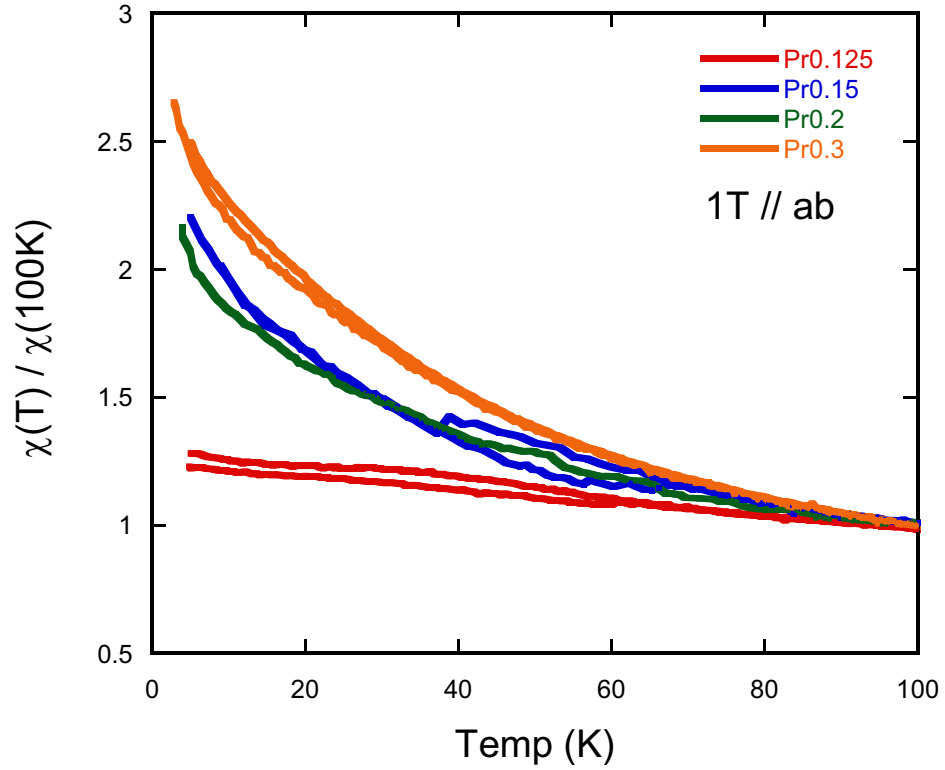


Figure 6.5: High field magnetization data on several crystals. Concentrations of 0.15, 0.2, and 0.3 were all grown under high pressure and subsequently annealed. The 0.125 sample is an ambient pressure growth included for comparison. Samples are all cooled under zero applied magnetic field. The higher doped Pr samples show stronger Curie tails, although Curie-Weiss analysis is not possible due to the extra contribution of the iron moment to this data.

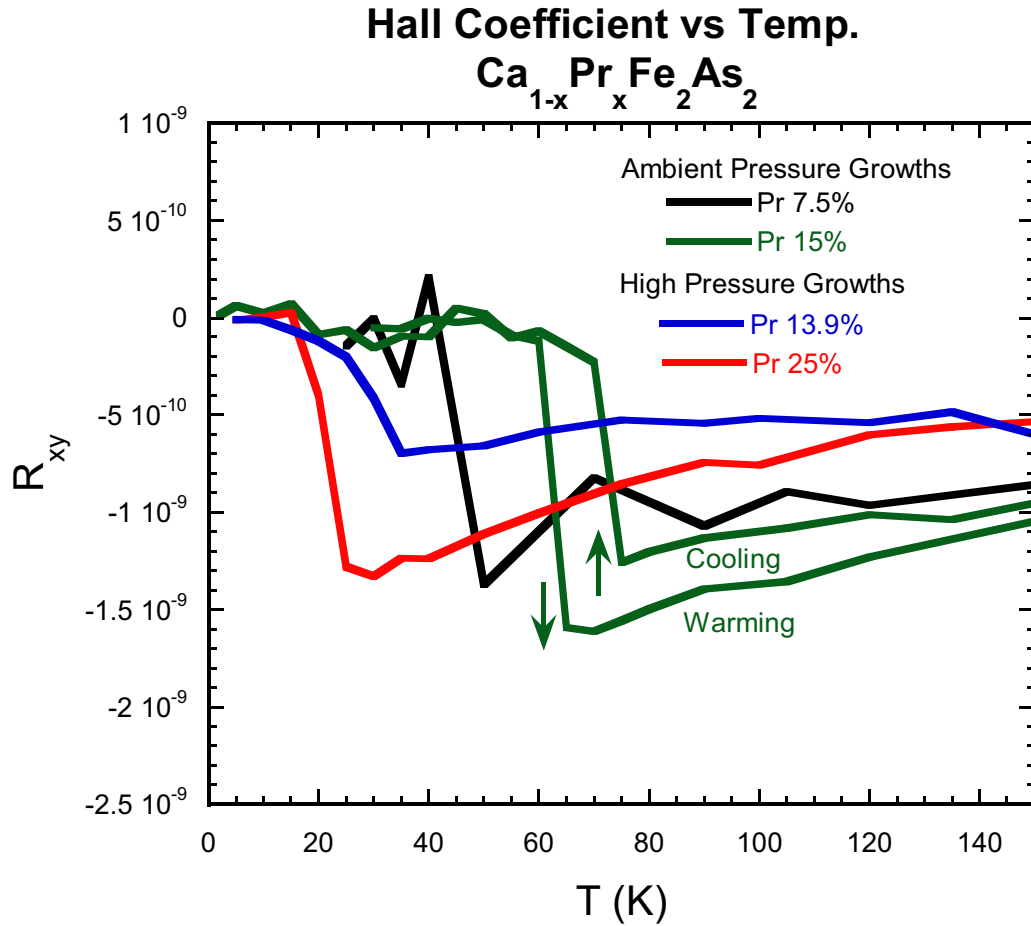


Figure 6.6: Hall effect data on a non-collapsing ambient pressure growth (black), a collapsing ambient pressure growth (green), a 14% Pr crystal grown under pressure (blue), and a 25% Pr crystal grown under pressure (red). The pressure growth crystals were both annealed, and show no trace of the collapse transition in Hall effect. The transitions that do occur are below the respective superconducting transition temperatures for these crystals.

6.5 Extended Phase Diagram and Discussion

In order to establish a full phase diagram, ambient growth crystals were also subjected to the same annealing schedule. With a full range of Pr dopings, we are able to construct a full phase diagram for the $\text{Ca}_{1-x}\text{Pr}_x\text{Fe}_2\text{As}_2$ system, with all crystals annealed at 400°C . Fig. 6.7 reveals the remarkable continuity between the ambient pressure growth crystals and the high pressure growth crystals, once factors like annealing and Pr content are fully accounted for. This opens up a full doping phase space; although it also shows an intriguing “bubble” in superconducting transition temperatures near 15% Pr.

Bulk superconductivity is not observed in this system. Although the annealing schedule is necessary in this study in order to recover typical 122 behavior, it may also be detrimental to the superconductivity, as has proven the case for the collapse transition. However, we now know that all of the behavior reported this far on the $\text{Ca}_{1-x}\text{Pr}_x\text{Fe}_2\text{As}_2$ system samples only a very small portion of the available phase space, and simply adding more Pr does not appear to increase the superconducting volume fraction.

In addition, this study also serves to clarify two popular pictures associated with these materials. The first idea is that the superconductivity in this system is interfacial in nature. This cannot be the case as the superconducting volume fraction does not appear to increase with increasing Pr content. In fact, the highest T_c in these materials is not evident at all beyond the 15% doping mark, suggesting

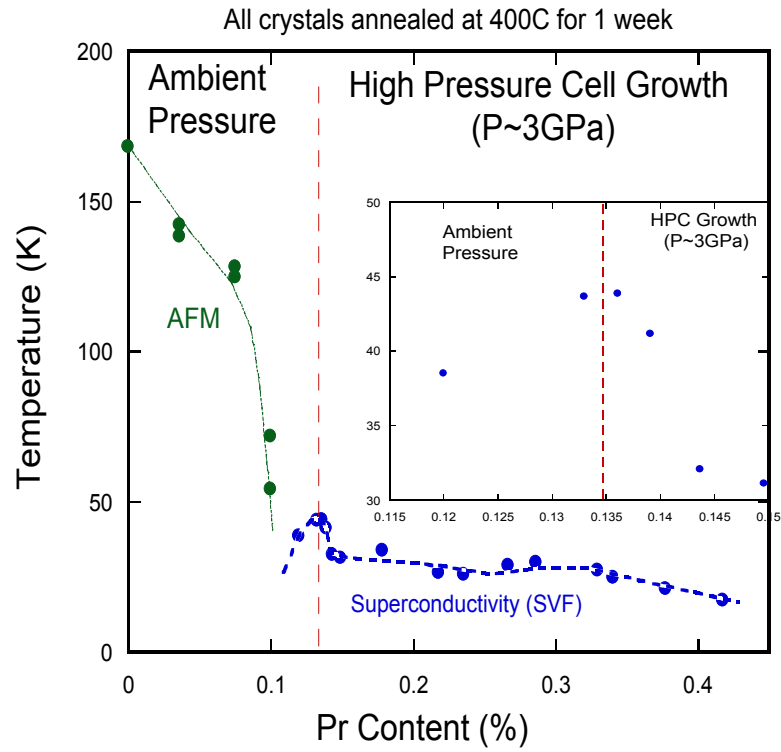


Figure 6.7: Phase diagram over the full range of Pr doping. Data left of the red line indicate crystals grown at ambient pressures and annealed at 400°C. Data right of the red line indicate crystals grown at high pressures and annealed at 400°C. With all crystals receiving the same post-growth thermal treatments, continuity between the two regions is observed near the 15% region. "SVF" indicates Small Volume Fraction, and serves to remind that all of the transitions observed in this study show very low volume fractions.

this is a crucial concentration for the high T_c phase. This model is further explored in Chapter 7.

The second idea is that the high T_c phase is only present in Pr-rich defects in these materials. This claim is partially disputed by other STM measurements which claim no clustering of the Pr dopants in similar crystals[111]. Furthermore, the high- T_c behavior is not seen in any of the higher concentration Pr crystals in this study. Higher Pr content should lead to more Pr defects, or at least a similar number. An important point here is that our crystals have been annealed, whereas the TEM crystals were quenched from high temperatures [108]. Nonetheless, the observance of the high- T_c phase even in annealed crystals near 15% Pr but not at other concentrations is in disagreement with the idea of defect-induced superconductivity. A model consistent with the observed data is discussed in Chapter 8.

Chapter 7

Current-dependent tests of Interfacial Superconductivity in

$\text{Ca}_{1-x}\text{R}_x\text{Fe}_2\text{As}_2$

As eluded to in the previous chapter, the high transition temperatures in $\text{Ca}_{1-x}\text{R}_x\text{Fe}_2\text{As}_2$ crystals, combined with very low volume fractions, has led to several proposals as to the nature of the observed superconducting phase. The presence of the collapse transition in the case of Pr- and Nd-doped crystals further complicates any analysis of this phase; however, in-depth magnetization measurements on these materials have produced interesting results, hinting at the possibility of an unusual superconducting ground state—weak-link superconductivity—a behavior typically only seen in polycrystalline materials[95, 112].

Weak-link, or interfacially enhanced, superconductivity is a well-studied phenomenon in the case of iron-pnictide superconductors[113, 114]. In the F-doped 1111 family of superconductors, a tail-like anomaly is observed in the resistive transitions of several of polycrystalline materials[115]. First studied in remnant magnetization measurements[116], it has also been seen that the transition temperatures of these materials have a large dependence on the current used for the measurement (and, by extension, the current density, since the size of the sample remains constant)[117].

It has been conjectured that this same behavior may be at work in single crystals of $\text{Ca}_{1-x}\text{R}_x\text{Fe}_2\text{As}_2$, which would be the first finding of such behavior in a non-granular system[95].

In this chapter, I will follow a previously established method[117] to probe the weak-link nature of the superconducting state in the R-doped CaFe_2As_2 system. I will present the resistance data of several single crystals of $\text{Ca}_{1-x}\text{La}_x\text{Fe}_2\text{As}_2$ and $\text{Ca}_{1-x}\text{Pr}_x\text{Fe}_2\text{As}_2$ using varying excitation currents. The results of these measurements are inconsistent with the picture of interfacially enhanced superconductivity.

7.1 Methods

Single crystals of $\text{Ca}_{1-x}\text{La}_x\text{Fe}_2\text{As}_2$ and $\text{Ca}_{1-x}\text{Pr}_x\text{Fe}_2\text{As}_2$ were grown using the self-flux method, as previously reported[4]. Large single crystals ($2 \times 2 \times 0.1 \text{ mm}^3$) were removed from the solidified flux. Nominal starting compositions are reported in this paper for simplicity; however, actual chemical concentrations are in agreement with earlier reports[1]. Resistivity measurements were performed using the standard four-probe ac method, via gold wire and Pb/Sn solder contacts (in order to ensure survival through the collapse transition) with typical contact resistances of $\sim 0.5 \Omega$ at room temperature. The excitation current was varied between 0.1 mA and 500 mA.

In order to test the interfacial nature of the superconductivity in these materials, we have followed the methodology of Sun *et. al.*[117] on the F-doped Nd-1111 system. It is instructive, for the sake of comparison, to quantify the effects of their

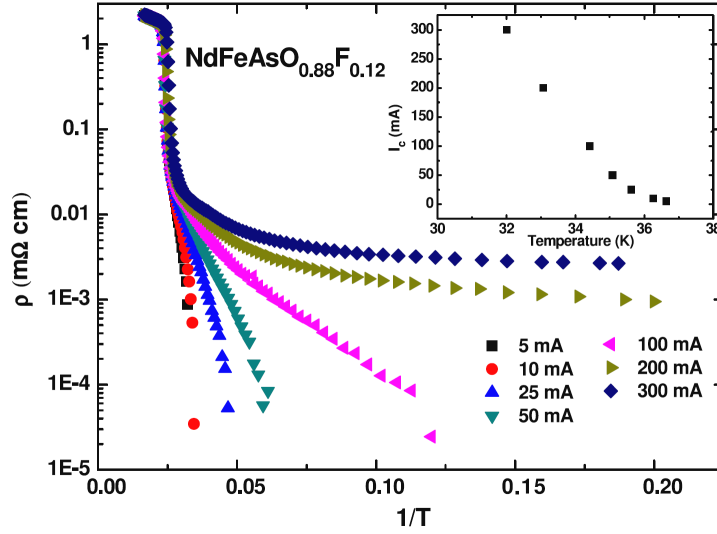


Figure 7.1: Semi-log plot of resistivity vs. inverse temperature for data collected on a polycrystalline sample of $\text{NdFeAsO}_{0.88}\text{F}_{0.12}$. The tail-effect discussed in the reference is obvious as increasing current leads to a strong increase in the measured resistivity. **Inset:** Excitation Current vs. T^* , defined in the reference as the temperature where the resistivity has decreased to 1% of its normal state value. The suppression of T^* with increasing current is evident. From [117].

study. Using the reported maximum critical current density $J_c \sim 4000 \text{ A/cm}^2$ [118] and the crystal dimensions reported in the paper, we can calculate that the critical current for the sample used by Sun *et. al.* is ~ 90 Amps, and the maximum current (300 mA) corresponds to approximately 0.33% of this critical current (which we will refer to as I_c). As shown in Fig. 7.1, applied currents well below 1% of the critical current density are able to suppress T_c by nearly 5 K. Because we are studying similar iron-based superconductors, it is reasonable to expect similar behavior if this same mechanism is responsible for the heightened T_c seen in the 122 family.

In order to investigate this phenomenon, several crystals of $\text{Ca}_{1-x}\text{R}_x\text{Fe}_2\text{As}_2$ (R=La, Pr) with varying concentrations of rare earth dopant were selected. Using the previously reported critical current density $J_c \sim 1000 \text{ A/cm}^2$ for the La-doped system[119] and the dimensions of our various crystals, we are able to determine the critical current I_c needed to return the crystal fully to the normal state. As indicated in the following plots, the far more interesting value in this study is actually 1% of I_c and the behavior of these materials below this threshold. T^* for this study is defined as the point where the resistance reaches 50% of the normal state value, which scales well with $T^*_{1\%}$ in these crystals (assuming the superconducting transition breaches this limit).

7.2 $\text{Ca}_{1-x}\text{Pr}_x\text{Fe}_2\text{As}_2$

As $\text{Ca}_{1-x}\text{Pr}_x\text{Fe}_2\text{As}_2$ is the most directly addressed material when discussing interfacial superconductivity, we turn our attention first to it. Fig. 7.2 shows the data taken on Pr-doped CaFe_2As_2 samples. Our first observation in these plots is of the notable lack of an anomalous tail in the resistive transitions (for comparison, see [117]). Established interfacial behavior typically results in a tail in the Arrhenius plot of the resistive transitions. By contrast, the resistive transitions of these materials drop quickly to a minimum, which remains constant until very high currents, at which point the floor begins to increase. I vs. T plots (Fig. 7.3) of this data help us to clear up the picture.

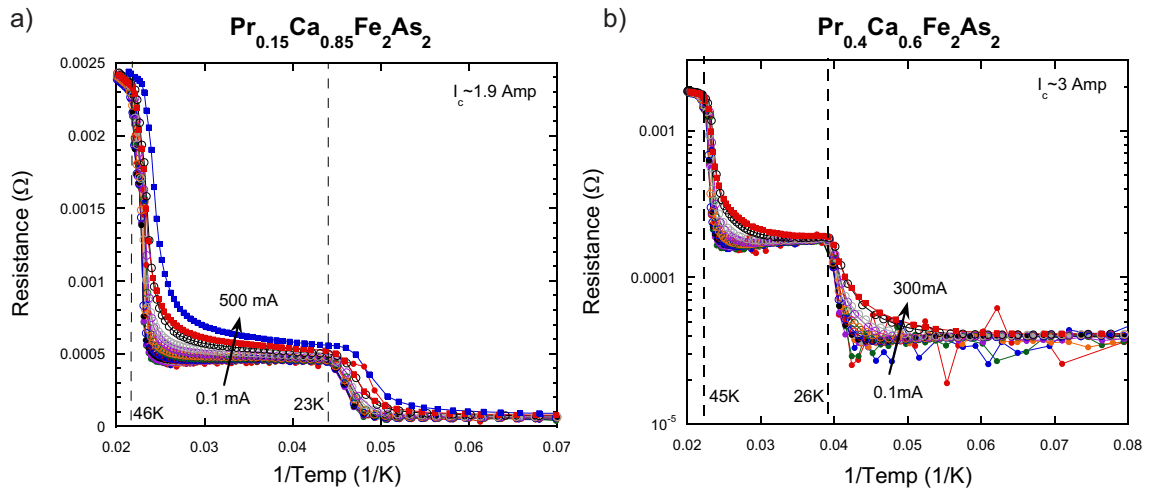


Figure 7.2: (a) Resistance vs. inverse temperature for a sample of nominal $\text{Pr}_{0.15}\text{Ca}_{0.85}\text{Fe}_2\text{As}_2$ (actual concentration of Pr $\sim 12.5\%$), with excitation currents ranging from 0.1 mA up to 500 mA. The transition temperatures of 46K and 23K are delineated for clarity. (b) Similar data on a semi-log scale for a sample of nominally $\text{Pr}_{0.40}\text{Ca}_{0.60}\text{Fe}_2\text{As}_2$ (actual Pr content $\sim 15\%$).

Before continuing, it is important to understand more in-depth the model being discussed. It is proposed that the higher T_c in these materials results from the interaction of weakly-linked superconducting volumes[95]. The lower transition temperature, on the other hand, should be an intrinsic superconducting transition. Thus, we would expect fundamentally different behaviors for the two superconducting transitions seen in $\text{Ca}_{1-x}\text{Pr}_x\text{Fe}_2\text{As}_2$.

Figure 7.3 plots the excitation current used in the above measurements against T^* for the $\text{Ca}_{1-x}\text{Pr}_x\text{Fe}_2\text{As}_2$ samples. Error bars for T^* are given as ± 0.25 K from the calculated temperature, consistent with the maximum distance between data points in the resistance data. Below roughly 1% of I_c , no dramatic change can be seen in T^* . Above this threshold, T^* is suppressed with increasing excitation current. This point can be made even more vividly using a semi-log scale, as shown in Fig. 7.4. Despite several orders of magnitude change in the excitation current, the transition temperature remains constant. At higher excitation currents, all transitions resemble the behavior expected for a J_c vs. T_c plot. This is contrary to the expected behavior in a weak-link system, as described above.

Another important point can be seen by comparing the behavior of these crystals in each of the superconducting states. As explained earlier, it is believed that the 40+ K transition corresponds to interfacially enhanced superconductivity, while the ~ 25 K transition is the intrinsic superconducting transition temperature for this material. In this case, it is reasonable to assume that the responses of the two superconducting states to increasing current density should differ significantly. This comes from the fact that interfacially enhanced superconductors are modeled

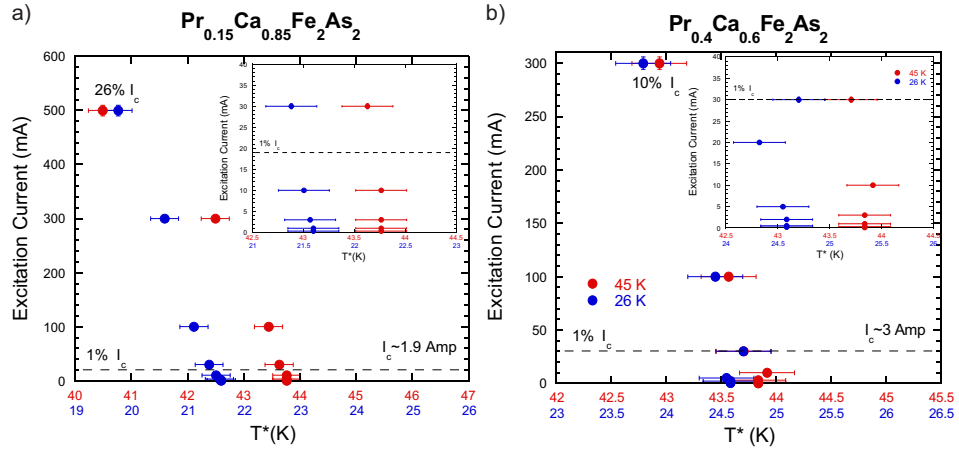


Figure 7.3: Excitation current plotted against T^* with both transitions shown for different dopings of $\text{Ca}_{1-x}\text{Pr}_x\text{Fe}_2\text{As}_2$ (a 15%, b 40%). **Inset a:** Expanded view of the data below the 1% I_c threshold. T^* remains the same, within error, up to 30 mA, which is nearly 16% of I_c . **Inset b:** Again, T^* remains relatively consistent and within error up to 1% of I_c .

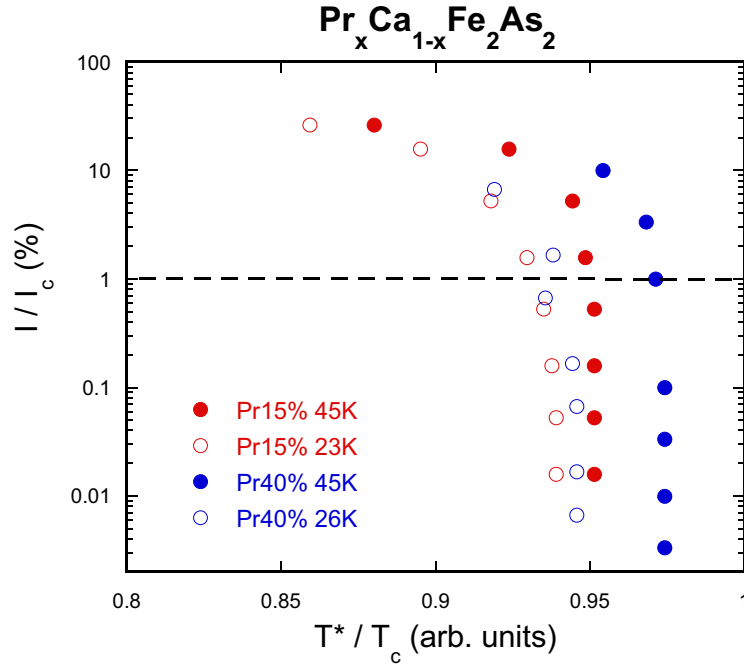


Figure 7.4: Excitation current normalized to I_c plotted against reduced temperature T^*/T_c , using the data from Fig. 7.3. Error bars are withheld for visual clarity; however, it is obvious that the transition temperature remains constant until the current exceeds the 1% I_c threshold.

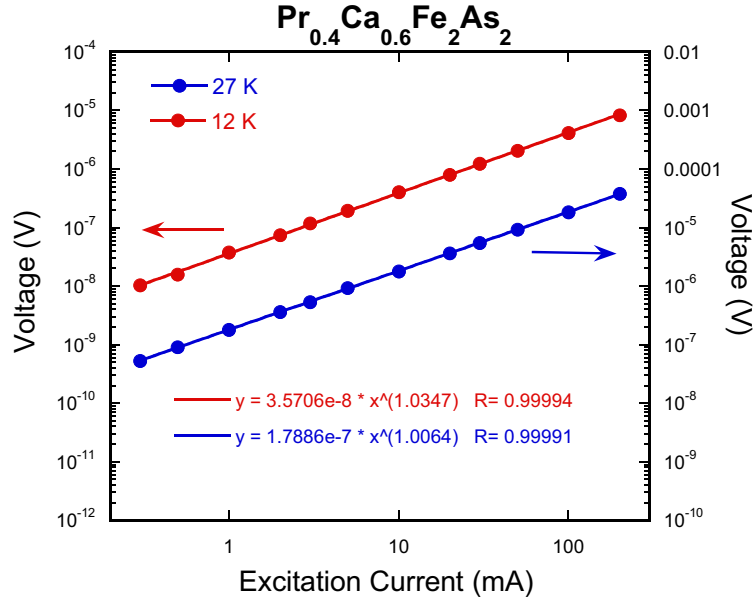


Figure 7.5: Voltage as a function of excitation current for a single crystal of $\text{Pr}_{0.4}\text{Ca}_{0.6}\text{Fe}_2\text{As}_2$. The solid lines indicate power law fits, with the power of both curves coming very close to 1.

as a series of Josephson Junctions, so that the superconductivity of the higher- T_c phase should show Josephson characteristics in the I-V behavior, while the lower transition should resemble the more typical superconducting behavior. As shown in Fig. 7.5, this is not the case. Plotting the I-V characteristics of these crystals in each superconducting state reproduces Ohm's Law and neither shows any Josephson Junction behavior over several orders of magnitude for the excitation current. The Ohm's Law response is to be expected, since the resistivity measurement is actually measuring the parts of the sample that are not superconducting (they are normal metals). The lack of any behavior deviating from Ohm's Law is somewhat surprising given the hypothetically different origins of the two superconducting transitions.

Instead, this points to a similar nature for both of these superconducting transitions, rather than radically different mechanisms. The likely scenario is that we are dealing with two superconducting transitions of similar nature, both of which are small volume fraction in this material due to some combination of doping, strain, and other factors. Indeed, it has been shown repeatedly how sensitive these materials are to strain effects, and this may be yet another reflection of that sensitivity[40, 120].

7.3 $\text{Ca}_{1-x}\text{La}_x\text{Fe}_2\text{As}_2$

To further refine our understanding of the superconductivity in these materials, we have performed similar investigations on $\text{Ca}_{1-x}\text{La}_x\text{Fe}_2\text{As}_2$ materials with different concentrations of La. These materials are essentially simplifications of the $\text{Ca}_{1-x}\text{Pr}_x\text{Fe}_2\text{As}_2$ materials: the lack of a collapse transition and the presence a single superconducting transition, in most cases, make understanding these compounds more straightforward. The raw data collected on several of these samples is shown in Fig. 5.

Figure 7.7 shows the I vs. T^* curves for the measured La-doped samples. Similar to the behavior demonstrated in Pr crystals, T^* for the La compounds remains constant, within the given error bars, despite excitation currents that vary by orders of magnitude. Above the 1% threshold, behavior recovers to the normal J_c vs. T_c result. It is important to note that the measurement of J_c [119] used in the calculation of I_c for all of the crystals in these experiments was performed on similar La crystals. In this case, we can be certain of the accuracy of J_c , and thus

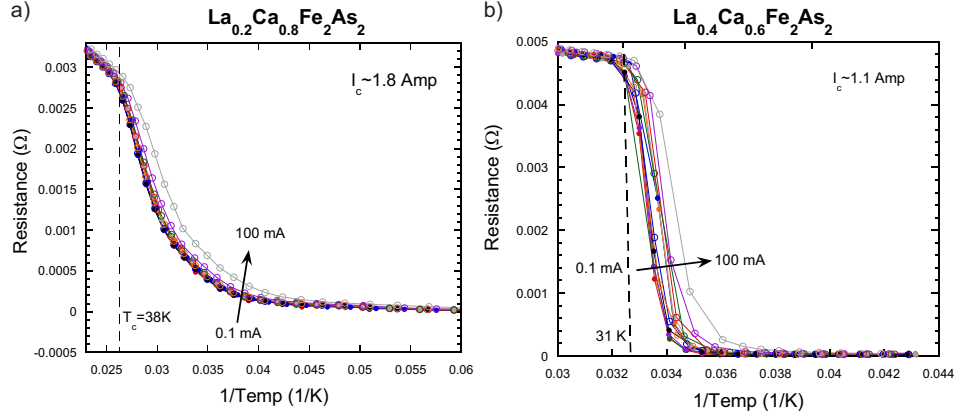


Figure 7.6: (a) Resistance vs. inverse temperature for a sample of nominally $\text{La}_{0.2}\text{Ca}_{0.8}\text{Fe}_2\text{As}_2$ (actual La $\sim 15\%$) The T_c at 38 K is delineated. (b) Resistance vs. inverse temperature for a sample of $\text{La}_{0.4}\text{Ca}_{0.6}\text{Fe}_2\text{As}_2$ (actual La $\sim 20\%$), with T_c of 31 K shown. Excitation currents ranging from 0.1mA up to 100 mA are shown.

our calculations for I_c . And the behavior of the superconducting transitions in both cases matches very well with the behavior observed in the $\text{Ca}_{1-x}\text{Pr}_x\text{Fe}_2\text{As}_2$ materials: there appears to be no variation in T^* despite increasing excitation currents over several orders of magnitude until the 1% I_c limit is reached.

7.4 Summary

Tests for weak-link superconductivity in the $\text{Ca}_{1-x}\text{R}_x\text{Fe}_2\text{As}_2$ systems have demonstrated results inconsistent with the expected behavior for weak-link superconductivity. Direct tests show that the current carrying capacity of the superconducting states in these materials remains stubbornly unchanged up to the level where normal critical current density effects come into play. The two superconduct-

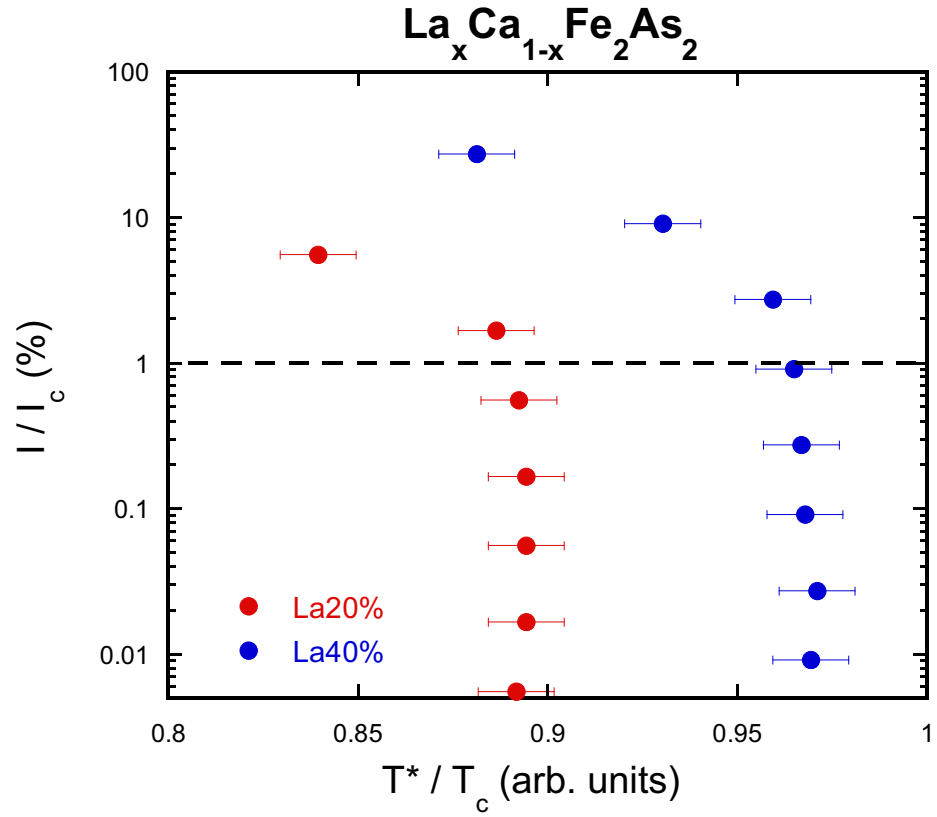


Figure 7.7: Normalized excitation current vs. reduced T^* (a) a sample of nominally $\text{La}_{0.2}\text{Ca}_{0.8}\text{Fe}_2\text{As}_2$ (actual La $\sim 15\%$) (b) a sample of $\text{La}_{0.4}\text{Ca}_{0.6}\text{Fe}_2\text{As}_2$ (actual La $\sim 20\%$). Error bars are $\pm 0.25\text{K}$, as stated previously.

ing transitions in $\text{Ca}_{1-x}\text{Pr}_x\text{Fe}_2\text{As}_2$ actually demonstrate very similar I-V characteristics, strongly implying that the mechanisms for each transition are not as radically different as interfacial superconductivity would necessitate. Furthermore, the general agreement between the different transitions in $\text{Ca}_{1-x}\text{Pr}_x\text{Fe}_2\text{As}_2$ crystals and in $\text{Ca}_{1-x}\text{La}_x\text{Fe}_2\text{As}_2$ crystals implies that the superconductivity of all of these phases is of a similar nature.

If interfacially enhanced superconductivity is not responsible for the strange behavior of these materials, then some other mechanism must be at work. Chapter 8 will present a summary of the properties of the $\text{Ca}_{1-x}\text{R}_x\text{Fe}_2\text{As}_2$ compounds as known to date as well as new ideas about the mechanisms for superconductivity in these materials.

Chapter 8

Summary and Outlook

This chapter attempts to provide a comprehensive overview of the state of the rare earth-doped CaFe_2As_2 compounds as it is known and to provide some context for further experiments that may resolve some of the outstanding issues with these materials. In the first part, I will survey the superconducting properties of these compounds and describe experiments that have aided our understanding of those properties. Where appropriate, I will highlight experiments that are inconsistent in order to demonstrate the areas where our knowledge of the $\text{Ca}_{1-x}\text{R}_x\text{Fe}_2\text{As}_2$ compounds must be improved. Next, I will describe a theoretical work that helps resolve some of these discrepancies and that may further our understanding of some of the unique aspects of these crystals. Finally, I will provide an outlook that aims at highlighting experimental and theoretical investigations that could help us finally gain a firm grasp on the superconductivity in these materials.

8.1 Summary

Extensive evidence indicates an intrinsic but small volume fraction superconducting state that arises as a result of doping CaFe_2As_2 with the rare earth elements La, Ce, Pr, and Nd. Annealing and etching[1] have no effect on the observed transition temperatures of these compounds and have shown no systematic suppression or

enhancement of the superconducting volume fraction. Further magnetization[109] and resistivity[110] measurements have confirmed the presence of the superconducting state in Pr-doped and La-doped CaFe_2As_2 , respectively. Moreover, the rate of suppression of the magnetic ordering is strongly dependent on the ionic radius of the rare-earth dopant[1] as is the solubility limit of the ion, and, interestingly, the smaller ions Pr and Nd are able to experience a thermally-induced transition to the collapsed tetragonal state under ambient pressure conditions. Perhaps not coincidentally, these materials also display higher superconducting temperatures, above 40 K.

The collapsed tetragonal transition displays bulk transition behavior in neutron scattering, Hall effect, and magnetization measurements. X-ray emission[121] and NMR[2] have confirmed the quenching of the iron magnetic moment as Pr-doped crystals transition into the collapsed tetragonal state. However, pressure growth experiments, discussed earlier, with annealed crystals have observed the presence of the high- T_c phase in $\text{Ca}_{1-x}\text{Pr}_x\text{Fe}_2\text{As}_2$ without observing the collapse transition in Hall effect measurements. This suggests that the collapse transition may not be necessary to induce the high- T_c phase.

The nature of the superconducting transition in these materials is a much more conflicted topic. Although it appears to be an intrinsic transition, reproduced by many groups throughout the world, the lack of a large volume fraction has given rise to many doubts. Several proposals have aimed to resolve this discrepancy, but have been thus far unable to completely answer the question. Although interfacially-enhanced superconductivity[95] would explain the low volume fraction, the high

transition temperatures, and is reminiscent of the behavior of other high temperature superconductors, as discussed previously, recent experiments are inconsistent with this picture in that increased doping actually suppresses the high- T_c transition and the superconducting transitions do not appear as sensitive to current as weak-link behavior would suggest.

Another proposal has been that the high- T_c phase comes from the presence of Pr (or other rare earth) defects clustering during synthesis; however, two excellent Scanning Tunnelling Microscopy (STM) experiments have produced very different results. The first, conducted on slow-cooled crystals of $\text{Ca}_{1-x}\text{Pr}_x\text{Fe}_2\text{As}_2$ found that the Pr ions were not clustered and in fact seemed to repulse one another, resulting in a consistent Pr sub-lattice throughout the crystal[111]. A more recent study, however, on crystals quenched from high temperatures, shows convincing evidence that the Pr atoms are clustered and that T_c peaks near these clusters[108]. Interestingly, both experiments observe the high- T_c phase in resistivity measurements. A resolution to this controversy will require in-depth STM experiments on both annealed and quenched crystals.

Further experiments have also shown interesting results when $\text{Ca}_{1-x}\text{R}_x\text{Fe}_2\text{As}_2$ materials are exposed to physical or chemical pressure. In addition to doping, introducing a physical strain on these crystals can suppress the magnetic ordering and induce superconductivity. But even more than that, physical pressure on a superconducting crystal actually increases the transition temperature[3]. On the other hand, experiments doping P for As in the $\text{Ca}_{1-x}\text{La}_x\text{Fe}_2\text{As}_2$ system have shown an increased transition temperature and, most importantly, a large increase in the vol-

ume fraction. Previous experiments that doped CaFe_2As_2 with P have demonstrated that the P atoms produce a chemical pressure effect that mimics very closely the role of physical pressure on these systems. Thus, it seems that the addition of pressure to $\text{Ca}_{1-x}\text{R}_x\text{Fe}_2\text{As}_2$ compounds actually helps to stabilize the superconducting phase. One very interesting experiment would be to measure the volume fraction of a sample under an increasing physical pressure, to determine if indeed it increases. Unfortunately, this experiment would require a hydrostatic pressure medium, and a pressure cell capable of applying high pressures with no magnetic background signal, which would be exceedingly difficult to construct.

8.2 Theoretical Work

Fortunately, theorists have also taken note of the high transition temperatures and peculiar properties of the rare earth doped CaFe_2As_2 materials. Using new computational methods, theoretical investigations are often able to probe parameters that are inaccessible experimentally. One very promising work in particular suggests an answer to some of the problems facing these materials.

Using Wannier functions, Limin Wang and the group of Wei Ku at Brookhaven National Lab have been successful in modeling the behavior of $\text{Ca}_{1-x}\text{Pr}_x\text{Fe}_2\text{As}_2$ materials in the normal and the collapsed tetragonal state[122]. The results indicate an orbital ordering in the normal state that is subsequently suppressed in the collapsed state. The presence of Pr atoms further suppresses this ordering, giving rise to a very localized superconducting phase. In addition, they have shown that small

amounts of pressure can also disrupt the orbital ordering, helping to stabilize the superconducting state. However, with increased Pr doping, the lattice becomes too strained and the superconductivity disappears.

Although very preliminary, this theoretical treatment could resolve several of the problems facing this system. First, it captures the fact that pressure is able to stabilize the superconducting state. It also explains why the high- T_c phase is only seen near the 15% mark in the extended $\text{Ca}_{1-x}\text{Pr}_x\text{Fe}_2\text{As}_2$ phase diagram and not in the higher concentration dopings. One very important detail is that it explains the inconsistencies in STM measurements: superconductivity can only exist near the Pr atoms, regardless of whether they are clustered or evenly dispersed throughout the sample. It also explains the low volume fraction and lack of zero resistivity observed in these samples as the superconductivity occurs only in localized regions.

While all of this is very promising, this treatment is far from complete. It does not describe any superconductivity in the normal tetragonal state, as seen in both the La and Ce compounds. A more complete theory must rectify this and explain the origins of this superconducting transition. Furthermore, it does not explain the second transition seen in resistivity measurements on $\text{Ca}_{1-x}\text{Pr}_x\text{Fe}_2\text{As}_2$ samples. As noted above, both transitions in Pr-doped samples show strikingly similar behaviors, so a complete theory must account for both of them.

8.3 Outlook and Further Work

A great deal of work remains to be done on these materials, experimentally as well as theoretically. Although reports of high volume fraction have surfaced[123], convincing heat capacity data on these samples has yet to be seen. This must be a top priority going forward, as no claims of bulk superconductivity can stand without heat capacity measurements to verify a phase transition.

A more comprehensive understanding of the relationship between the collapsed tetragonal phase and the high- T_c superconducting phase must also be established. Investigations by most groups currently ignore the presence or absence of the collapse transition in their materials; however, this transition is at least imparting some strain to the crystals. The impact of that transition on the superconducting state must be understood in order to develop a full picture of the physics of this system.

Stabilizing a bulk superconducting phase in these materials is paramount to a more refined understanding of the superconducting state. With only a minority superconducting phase, it is very difficult to perform measurements that probe the nature of only the superconducting. Bulk superconductivity would open up the entire pantheon of experimental techniques to probe this unique superconducting state. This is the crucial step in being able to gain a firm understanding of the superconductivity in these materials and building models for other possible systems.

Despite these hurdles, work on these materials will be propelled forward by the hopes of high- T_c intermetallic superconductors. With transition temperatures only slightly lower than the highest iron pnictide superconductors, these materials

are easy to grow and characterize. With moderate gains in T_c accompanying a fuller understanding of the interplay between the magnetic, collapsed, and superconducting states, the $\text{Ca}_{1-x}\text{R}_x\text{Fe}_2\text{As}_2$ materials hold a lot of promise for becoming the dominant materials for superconducting applications.

Appendix A

Summary of Compounds

The natural tendency in scientific investigation is to report our successes. However, the important role that serendipity has always played in the search for new superconductors dictates that our failures must also be repeated, in order that the next scientist can learn from our mistakes as much as our successes. The following is an exhaustive list of the compounds attempted in our search for new superconducting compounds, the type of synthesis we attempted, and the results.

Target Compound	Growth Method	Result	T_c (max)
$\text{BaFe}_2\text{As}_{1.4}\text{P}_{0.6}$	single crystal	Did not form	
BaFe_2AsP	single crystal	Did not form	
$\text{SrFe}_2\text{As}_{1.4}\text{P}_{0.6}$	single crystal	Did not form	
SrFe_2AsP	single crystal	Did not form	
$\text{Fe}_{0.5}\text{Co}_{0.5}\text{As}$	Solid state	Did not form	
$\text{Fe}_{0.95}\text{Co}_{0.05}\text{As}$	Solid state	Did not form	
$\text{Ba}_{0.6}\text{K}_{0.4}\text{Fe}_{1.6}\text{Co}_{0.4}\text{As}_2$	single crystal	Did not form	
$\text{Ba}_{0.8}\text{K}_{0.2}\text{Fe}_{1.8}\text{Co}_{0.2}\text{As}_2$	single crystal	Did not form	
$\text{Ba}_{0.9}\text{K}_{0.1}\text{Fe}_{1.9}\text{Co}_{0.1}\text{As}_2$	single crystal	Did not form	
$\text{Ca}_{0.98}\text{Mg}_{0.02}\text{Fe}_2\text{As}_2$	single crystal	Did not form	
$\text{Ca}_{0.95}\text{Mg}_{0.05}\text{Fe}_2\text{As}_2$	single crystal	Did not form	

Target Compound	Growth Method	Result	T_c (max)
$\text{Ca}_{0.5}\text{Mg}_{0.5}\text{Fe}_2\text{As}_2$	single crystal	Did not form	
$\text{Ca}_{0.25}\text{Mg}_{0.75}\text{Fe}_2\text{As}_2$	single crystal	Did not form	
$\text{SrFe}_{1.92}\text{Pt}_{0.08}\text{As}_2$	single crystal	Large Crystals	19 K
$\text{SrFe}_{1.88}\text{Pt}_{0.12}\text{As}_2$	single crystal	Large Crystals	19 K
$\text{SrFe}_{1.85}\text{Pt}_{0.15}\text{As}_2$	single crystal	Large Crystals	19 K
$\text{SrFe}_{1.83}\text{Pt}_{0.17}\text{As}_2$	single crystal	Large Crystals	19 K
$\text{SrFe}_{1.8}\text{Pt}_{0.2}\text{As}_2$	single crystal	Large Crystals	19 K
$\text{SrFe}_{1.77}\text{Pt}_{0.23}\text{As}_2$	single crystal	Large Crystals	19 K
$\text{BaFe}_{1.85}\text{Pt}_{0.15}\text{As}_2$	single crystal	Large Crystals	23 K
$\text{SrFe}_{0.55}\text{Co}_{0.725}\text{Ni}_{0.725}\text{As}_2$	single crystal	Crystals	No T_c
$\text{SrFe}_{0.60}\text{Co}_{0.7}\text{Ni}_{0.7}\text{As}_2$	single crystal	Crystals	No T_c
$\text{SrFe}_{0.70}\text{Co}_{0.65}\text{Ni}_{0.65}\text{As}_2$	single crystal	Crystals	No T_c
$\text{SrFe}_{0.75}\text{Co}_{0.625}\text{Ni}_{0.625}\text{As}_2$	single crystal	Crystals	No T_c
$\text{SrFe}_{0.66}\text{Co}_{0.66}\text{Ni}_{0.66}\text{As}_2$	single crystal	Crystals	No T_c
SrFeNiAs_2	single crystal	Crystals	No T_c
$\text{Ca}_{0.95}\text{Pr}_{0.05}\text{Fe}_2\text{As}_2$	single crystal	Large Crystals	47 K
$\text{Ca}_{0.925}\text{Pr}_{0.075}\text{Fe}_2\text{As}_2$	single crystal	Large Crystals	47 K
$\text{Ca}_{0.91}\text{Pr}_{0.09}\text{Fe}_2\text{As}_2$	single crystal	Large Crystals	47 K
$\text{Ca}_{0.9}\text{Pr}_{0.1}\text{Fe}_2\text{As}_2$	single crystal	Large Crystals	47 K
$\text{Ca}_{0.875}\text{Pr}_{0.125}\text{Fe}_2\text{As}_2$	single crystal	Large Crystals	47 K
$\text{Ca}_{0.85}\text{Pr}_{0.15}\text{Fe}_2\text{As}_2$	single crystal	Large Crystals	47 K

Target Compound	Growth Method	Result	T_c (max)
$\text{Ca}_{0.85}\text{Pr}_{0.15}\text{Fe}_2\text{As}_2$	Solid state	Did not form	
$\text{Ca}_{0.825}\text{Pr}_{0.175}\text{Fe}_2\text{As}_2$	single crystal	Did not form	
$\text{Ca}_{0.8}\text{Pr}_{0.2}\text{Fe}_2\text{As}_2$	single crystal	Did not form	
$\text{Ca}_{0.7}\text{Pr}_{0.3}\text{Fe}_2\text{As}_2$	single crystal	Did not form	
$\text{Ca}_{0.6}\text{Pr}_{0.4}\text{Fe}_2\text{As}_2$	single crystal	Did not form	
$\text{Ca}_{0.95}\text{Nd}_{0.05}\text{Fe}_2\text{As}_2$	single crystal	Large Crystals	42 K
$\text{Ca}_{0.925}\text{Nd}_{0.075}\text{Fe}_2\text{As}_2$	single crystal	Large Crystals	42 K
$\text{Ca}_{0.91}\text{Nd}_{0.09}\text{Fe}_2\text{As}_2$	single crystal	Large Crystals	42 K
$\text{Ca}_{0.9}\text{Nd}_{0.1}\text{Fe}_2\text{As}_2$	single crystal	Large Crystals	42 K
$\text{Ca}_{0.85}\text{Nd}_{0.15}\text{Fe}_2\text{As}_2$	single crystal	Did not form	
$\text{Ca}_{0.8}\text{Nd}_{0.2}\text{Fe}_2\text{As}_2$	single crystal	Did not form	
$\text{Ca}_{0.7}\text{Nd}_{0.3}\text{Fe}_2\text{As}_2$	single crystal	Did not form	
$\text{Ca}_{0.6}\text{Nd}_{0.4}\text{Fe}_2\text{As}_2$	single crystal	Did not form	
$\text{Ca}_{0.4}\text{Nd}_{0.6}\text{Fe}_2\text{As}_2$	single crystal	Did not form	
$\text{Ca}_{0.85}\text{Sm}_{0.15}\text{Fe}_2\text{As}_2$	single crystal	Did not form	
$\text{Ca}_{0.825}\text{Sm}_{0.175}\text{Fe}_2\text{As}_2$	single crystal	Did not form	
$\text{Ca}_{0.8}\text{Sm}_{0.2}\text{Fe}_2\text{As}_2$	single crystal	Did not form	
$\text{Ca}_{0.75}\text{Sm}_{0.25}\text{Fe}_2\text{As}_2$	single crystal	Did not form	
$\text{Ca}_{0.7}\text{Sm}_{0.3}\text{Fe}_2\text{As}_2$	single crystal	Did not form	
$\text{Ca}_{0.85}\text{Gd}_{0.15}\text{Fe}_2\text{As}_2$	single crystal	Did not form	
$\text{Ca}_{0.825}\text{Gd}_{0.175}\text{Fe}_2\text{As}_2$	single crystal	Did not form	

Target Compound	Growth Method	Result	T_c (max)
$\text{Ca}_{0.8}\text{Gd}_{0.2}\text{Fe}_2\text{As}_2$	single crystal	Did not form	
$\text{Ca}_{0.7}\text{Gd}_{0.3}\text{Fe}_2\text{As}_2$	single crystal	Did not form	
$\text{Ca}_{0.85}\text{La}_{0.15}\text{Fe}_2\text{As}_2$	single crystal	Large Crystals	35 K
$\text{Ca}_{0.8}\text{La}_{0.2}\text{Fe}_2\text{As}_2$	single crystal	Large Crystals	35 K
$\text{Ca}_{0.8}\text{La}_{0.2}\text{Fe}_2\text{As}_2$	Solid state	Did not form	35 K
$\text{Ca}_{0.7}\text{La}_{0.3}\text{Fe}_2\text{As}_2$	single crystal	Large Crystals	35 K
$\text{Ca}_{0.6}\text{La}_{0.4}\text{Fe}_2\text{As}_2$	single crystal	Did not form	
$\text{Ca}_{0.5}\text{La}_{0.5}\text{Fe}_2\text{As}_2$	single crystal	Did not form	
$\text{Ca}_{0.4}\text{La}_{0.6}\text{Fe}_2\text{As}_2$	single crystal	Did not form	
$\text{Ca}_{0.85}\text{Ce}_{0.15}\text{Fe}_2\text{As}_2$	single crystal	Large Crystals	30 K
$\text{Ca}_{0.7}\text{Ce}_{0.3}\text{Fe}_2\text{As}_2$	single crystal	Large Crystals	30 K
$\text{Ca}_{0.6}\text{Ce}_{0.4}\text{Fe}_2\text{As}_2$	single crystal	Did not form	
$\text{Ca}_{0.5}\text{Ce}_{0.5}\text{Fe}_2\text{As}_2$	single crystal	Did not form	
$\text{Ca}_{0.9}\text{Yb}_{0.1}\text{Fe}_2\text{As}_2$	single crystal	Did not form	
$\text{Ca}_{0.8}\text{Yb}_{0.2}\text{Fe}_2\text{As}_2$	single crystal	Did not form	
$\text{CaCe}_{0.15}\text{Sm}_{0.05}\text{Fe}_2\text{As}_2$	single crystal	Did not form	
$\text{CaCe}_{0.1}\text{Sm}_{0.1}\text{Fe}_2\text{As}_2$	single crystal	Did not form	
$\text{CaCe}_{0.05}\text{Sm}_{0.15}\text{Fe}_2\text{As}_2$	single crystal	Did not form	
$\text{CaFe}_2\text{As}_{1.9}\text{Ge}_{0.1}$	single crystal	Did not form	
$\text{CaFe}_2\text{As}_{1.8}\text{Ge}_{0.2}$	single crystal	Did not form	
$\text{CaFe}_2\text{As}_{1.7}\text{Ge}_{0.3}$	single crystal	Did not form	

Target Compound	Growth Method	Result	T_c (max)
$\text{CaFe}_2\text{As}_{1.4}\text{Ge}_{0.6}$	single crystal	Did not form	
$\text{SrFe}_{1.98}\text{Mn}_{0.02}\text{As}_2$	single crystal	Did not form	
$\text{SrFe}_{1.95}\text{Mn}_{0.05}\text{As}_2$	single crystal	Did not form	
$\text{SrFe}_{1.9}\text{Mn}_{0.1}\text{As}_2$	single crystal	Did not form	
CaNi_2As_2	single crystal	Did not form	
CaNi_2As_2	Solid state	Did not form	
CaFeGe	single crystal	Did not form	
BaFeGe	single crystal	Did not form	
LaFe_2Ge_2	single crystal	Did not form	
YFe_2Ge_2	single crystal	Did not form	
$\text{BaFe}_{1.9}\text{Os}_{0.1}\text{As}_2$	single crystal	Did not form	
$\text{BaFe}_{1.75}\text{Os}_{0.25}\text{As}_2$	single crystal	Did not form	
CaCo_2Ge_2	single crystal	Did not form	
CaCo_2Si_2	single crystal	Did not form	
SrCo_2Ge_2	single crystal	Did not form	
SrCo_2Si_2	single crystal	Did not form	
BaCo_2Ge_2	single crystal	Did not form	
BaCo_2Si_2	single crystal	Did not form	
$\text{BaCo}_{1.9}\text{Ni}_{0.1}\text{Si}_2$	single crystal	Did not form	
LaCo_2Ge_2	Solid state	Polycrystalline	No T_c
LaFeCoGe_2	Solid state	Polycrystalline	No T_c

Target Compound	Growth Method	Result	T_c (max)
$\text{Ca}_{0.95}\text{Bi}_{0.05}\text{Fe}_2\text{As}_2$	single crystal	Did not form	
$\text{Ca}_{0.9}\text{Bi}_{0.1}\text{Fe}_2\text{As}_2$	single crystal	Did not form	
$\text{Ca}_{0.8}\text{Bi}_{0.2}\text{Fe}_2\text{As}_2$	single crystal	Did not form	
$(\text{Sr,Ca,L a})\text{Fe}_2\text{As}_2\text{-La}_{0.05}$	single crystal	Large Crystals	No T_c
$(\text{Sr,Ca,L a})\text{Fe}_2\text{As}_2\text{-La}_{0.10}$	single crystal	Large Crystals	No T_c
$(\text{Sr,Ca,L a})\text{Fe}_2\text{As}_2\text{-La}_{0.15}$	single crystal	Large Crystals	No T_c
$(\text{Sr,Ca,L a})\text{Fe}_2\text{As}_2\text{-La}_{0.20}$	single crystal	Large Crystals	No T_c
$(\text{Sr,Ca,L a})\text{Fe}_2\text{As}_2\text{-La}_{0.25}$	single crystal	Large Crystals	No T_c
$(\text{Sr,Ca,L a})\text{Fe}_2\text{As}_2\text{-La}_{0.30}$	single crystal	Did not form	
$(\text{Sr,Ca,L a})\text{Fe}_2\text{As}_2\text{-La}_{0.35}$	single crystal	Did not form	
$(\text{Sr,Ca,L a})\text{Fe}_2\text{As}_2\text{-La}_{0.40}$	single crystal	Did not form	
$(\text{Sr,Ca,L a})\text{Fe}_2\text{As}_2\text{-La}_{0.50}$	single crystal	Did not form	
$(\text{Sr,Ca,L a})\text{Fe}_2\text{As}_2\text{-La}_{0.60}$	single crystal	Did not form	
$(\text{Sr,Ca,L a})\text{Fe}_2\text{As}_2\text{-La}_{0.70}$	single crystal	Did not form	
SrCo_2As_2	single crystal	Crystals	No T_c
$\text{SrCo}_{1.99}\text{Fe}_{0.01}\text{As}_2$	single crystal	Did not form	
$\text{SrCo}_{1.98}\text{Fe}_{0.02}\text{As}_2$	single crystal	Did not form	
$\text{SrCo}_{1.95}\text{Fe}_{0.05}\text{As}_2$	single crystal	Did not form	
BaCo_2As_2	single crystal	Crystals	No T_c
$\text{BaCo}_{1.99}\text{Fe}_{0.01}\text{As}_2$	single crystal	Did not form	
$\text{BaCo}_{1.98}\text{Fe}_{0.02}\text{As}_2$	single crystal	Did not form	

Target Compound	Growth Method	Result	T_c (max)
BaCo _{1.95} Fe _{0.05} As ₂	single crystal	Did not form	
BaFe _{0.66} Co _{0.66} Ni _{0.66} As ₂	single crystal	Large Crystals	No T_c
Ba _{0.9} Sr _{0.1} Ni ₂ As ₂	single crystal	Crystals	3.2 K
Ba _{0.8} Sr _{0.2} Ni ₂ As ₂	single crystal	Crystals	3.2 K
Ba _{0.75} Sr _{0.25} Ni ₂ As ₂	single crystal	Crystals	3.2 K
Ba _{0.6} Sr _{0.4} Ni ₂ As ₂	single crystal	Crystals	3.2 K
Ba _{0.5} Sr _{0.5} Ni ₂ As ₂	single crystal	Crystals	3.2 K
Ba _{0.4} Sr _{0.6} Ni ₂ As ₂	single crystal	Crystals	3.2 K
Ba _{0.375} Sr _{0.625} Ni ₂ As ₂	single crystal	Crystals	3.2 K
Ba _{0.35} Sr _{0.65} Ni ₂ As ₂	single crystal	Crystals	3.2 K
Ba _{0.325} Sr _{0.675} Ni ₂ As ₂	single crystal	Crystals	3.2 K
Ba _{0.3} Sr _{0.7} Ni ₂ As ₂	single crystal	Crystals	3.2 K
Ba _{0.275} Sr _{0.725} Ni ₂ As ₂	single crystal	Crystals	3.2 K
Ba _{0.25} Sr _{0.75} Ni ₂ As ₂	single crystal	Crystals	3.2 K
Ba _{0.2} Sr _{0.8} Ni ₂ As ₂	single crystal	Crystals	3.2 K
Ba _{0.1} Sr _{0.9} Ni ₂ As ₂	single crystal	Crystals	3.2 K
SrNi ₂ As ₂	single crystal	Crystals	
BaMn ₂ As ₂ Ni ₂ As ₂	single crystal	Large Crystals	No T_c
BaNi _{1.98} Co _{0.02} As ₂	single crystal	Crystals	
BaNi _{1.96} Co _{0.04} As ₂	single crystal	Crystals	
BaNi _{1.9} Co _{0.1} As ₂	single crystal	Crystals	

Target Compound	Growth Method	Result	T_c (max)
BaNi _{1.8} Co _{0.2} As ₂	single crystal	Crystals	
BaNi _{1.7} Co _{0.3} As ₂	single crystal	Did not form	
BaNi _{1.6} Co _{0.4} As ₂	single crystal	Did not form	
BaNi _{1.98} Fe _{0.02} As ₂	single crystal	Crystals	
BaNi _{1.96} Fe _{0.04} As ₂	single crystal	Crystals	
BaNi _{1.9} Fe _{0.1} As ₂	single crystal	Crystals	
BaNi _{1.8} Fe _{0.2} As ₂	single crystal	Did not form	
Ca _{0.95} Pr _{0.05} Fe ₂ As _{1.94} P _{0.06}	single crystal	Large Crystals	45 K
Ca _{0.9} Pr _{0.10} Fe ₂ As _{1.94} P _{0.06}	single crystal	Large Crystals	45 K
Ca _{0.85} Pr _{0.15} Fe ₂ As _{1.94} P _{0.06}	single crystal	Large Crystals	45 K
Ca _{0.8} Pr _{0.20} Fe ₂ As _{1.94} P _{0.06}	single crystal	Large Crystals	45 K
Ca _{0.95} Pr _{0.05} Fe ₂ As _{1.88} P _{0.12}	single crystal	Large Crystals	45 K
Ca _{0.90} Pr _{0.10} Fe ₂ As _{1.88} P _{0.12}	single crystal	Large Crystals	45 K
Ca _{0.85} Pr _{0.15} Fe ₂ As _{1.88} P _{0.12}	single crystal	Large Crystals	45 K
Ca _{0.80} Pr _{0.20} Fe ₂ As _{1.88} P _{0.12}	single crystal	Large Crystals	45 K
SrCo ₂ P ₂	single crystal	Did not form	
SrCo _{1.9} Ni _{0.1} P ₂	single crystal	Did not form	
SrCo _{1.8} Ni _{0.2} P ₂	single crystal	Did not form	
SrCo _{1.6} Ni _{0.4} P ₂	single crystal	Did not form	
SrCoNiP ₂	single crystal	Did not form	
SrNi _{1.6} Co _{0.4} P ₂	single crystal	Did not form	

Target Compound	Growth Method	Result	T_c (max)
$\text{SrNi}_{1.8}\text{Co}_{0.2}\text{P}_2$	single crystal	Did not form	
$\text{SrNi}_{1.9}\text{Co}_{0.1}\text{P}_2$ SrNi_2P_2	single crystal	Did not form	
$\text{Ca}_{0.95}\text{La}_{0.05}\text{Fe}_2\text{As}_{1.88}\text{P}_{0.12}$	single crystal	Large Crystals	49 K
$\text{Ca}_{0.90}\text{La}_{0.10}\text{Fe}_2\text{As}_{1.88}\text{P}_{0.12}$	single crystal	Large Crystals	49 K
$\text{Ca}_{0.85}\text{La}_{0.15}\text{Fe}_2\text{As}_{1.88}\text{P}_{0.12}$	single crystal	Large Crystals	49 K
$\text{Ca}_{0.83}\text{La}_{0.17}\text{Fe}_2\text{As}_{1.88}\text{P}_{0.12}$	single crystal	Large Crystals	49 K
$\text{Ca}_{0.80}\text{La}_{0.20}\text{Fe}_2\text{As}_{1.88}\text{P}_{0.12}$	single crystal	Large Crystals	49 K

Bibliography

- [1] S. R. Saha, N. P. Butch, T. Drye, J. Magill, S. Ziemak, K. Kirshenbaum, P. Y. Zavalij, J. W. Lynn, and J. Paglione, “Structural collapse and superconductivity in rare-earth-doped CaFe_2As_2 ,” *Physical Review B*, vol. 85, p. 024525, Jan. 2012.
- [2] L. Ma, G.-F. Ji, J. Dai, S. R. Saha, T. Drye, J. Paglione, and W.-Q. Yu, “Quenched Fe moment in the collapsed tetragonal phase of $\text{Ca}_{1-x}\text{Pr}_x\text{Fe}_2\text{As}_2$,” *Chinese Physics B*, vol. 22, p. 057401, May 2013.
- [3] S. R. Saha, T. Drye, S. K. Goh, L. E. Klintberg, J. M. Silver, F. M. Grosche, M. Sutherland, T. J. S. Munsie, G. M. Luke, D. K. Pratt, J. W. Lynn, and J. Paglione, “Segregation of antiferromagnetism and high-temperature superconductivity in $\text{Ca}_{1-x}\text{La}_x\text{Fe}_2\text{As}_2$,” *Physical Review B*, vol. 89, p. 134516, Apr. 2014.
- [4] T. B. Drye, S. R. Saha, J. Paglione, and P. Y. Zavalij, “Rare earth substitution in lattice-tuned $\text{Sr}_{0.3}\text{Ca}_{0.7}\text{Fe}_2\text{As}_2$ solid solutions,” *Superconductor Science and Technology*, vol. 25, p. 084014, Aug. 2012.
- [5] R. Ouboter, “Heike Kamerlingh Onnes’ discovery of superconductivity,” *Scientific American*, Mar. 1997.
- [6] J. Nobel, “The discovery of superconductivity,” *Physics Today*, vol. 49, no. 9, 1996.
- [7] J. Bardeen, L. N. Cooper, and J. R. Schrieffer, “Theory of superconductivity,” *Physical Review*, vol. 108, p. 1175, 1957.
- [8] C. Kittel, *Introduction to Solid State Physics*. John Wiley and Sons, 1953.
- [9] J. G. Bednorz and K. A. Mller, “Possible high T_c superconductivity in the BaLaCuO system,” *Zietschrift fr Physik B*, vol. 64, p. 189, 1986.
- [10] P. Dai, B. C. Chakoumakos, G. F. Sun, K. W. Wong, Y. Xin, and D. F. Lu, “Synthesis and neutron powder diffraction study of the superconductor $\text{HgBa}_2\text{Ca}_2\text{Cu}_3\text{O}_{8+\delta}$ by Tl substitution,” *Physica C*, vol. 243, p. 201, 1995.
- [11] N. P. Butch, M. C. d. Andrade, and M. B. Maple, “Resource letter scy-3: Superconductivity,” *American Journal of Physics*, vol. 76, p. 106, 2008.
- [12] C. W. Chu, L. Gao, F. Chen, Z. J. Huang, R. L. Meng, and Y. Y. Xue, “Superconductivity above 150K in $\text{HgBa}_2\text{Ca}_2\text{Cu}_3\text{O}_{8+\delta}$ at high pressures,” *Nature*, vol. 365, p. 323, 1993.
- [13] N. W. Ashcroft and N. D. Mermin, *Solid State Physics*. Harcourt College Publishers, 1976.

- [14] M. R. Norman, “The challenge of unconventional superconductivity,” *Science*, vol. 332, p. 196, 2011.
- [15] W. Meissner and R. Ochsenfeld, “Ein neuer effekt bei eintritt der supraleitfähigkeit,” *Naturwissenschaften*, vol. 21, p. 787, 1933.
- [16] J. Bardeen, L. N. Cooper, and J. R. Schrieffer, “Microscopic theory of superconductivity,” *Physical Review*, vol. 106, p. 162, 1957.
- [17] M. Tinkham, *Introduction to Superconductivity*. Dover Publications, 1996.
- [18] D. K. Finnemore, T. F. Stromberg, and C. A. Swenson, “Superconducting properties of high-purity niobium,” *Physical Review*, vol. 149, p. 231, 1966.
- [19] S. K. Adhikari, M. Casas, A. Puente, A. Rigo, M. Fortes, M. A. Sols, M. d. Llano, A. A. Valladares, and O. Rojo, “Superconductivity as a bose-einstein condensation?,” *Physica C*, vol. 233, p. 341, 2000.
- [20] F. Marsiglio and J. P. Carbotte, “Electron-phonon superconductivity,”
- [21] B. Brandow, “Characteristic features of the exotic superconductors,” *Physics Reports*, vol. 296, p. 1, 1998.
- [22] E. W. Carlson, V. J. Emery, S. A. Kivelson, and D. Orgad, “Concepts in high temperature superconductivity,”
- [23] I. I. Mazin, “Superconductivity gets an iron boost,” *Nature*, vol. 464, p. 183, 2010.
- [24] J. Paglione and R. L. Greene, “High-temperature superconductivity in iron-based materials,” *Nature: Physics*, vol. 6, p. 645, 2010.
- [25] M. R. Norman and C. Pepin, “The electronic nature of high temperature cuprate superconductors,” *Reports on Progress in Physics*, vol. 66, p. 1547, 2003.
- [26] D. R. Harshman and J. A. P. Mills, “Concerning the nature of high- T_c superconductivity: Survey of experimental properties and implications for interlayer coupling,” *Physical Review B*, vol. 45, p. 10684, 1992.
- [27] P. W. Anderson, “The resonating valence bond state in LaCuO and superconductivity,” *Science*, vol. 235, p. 1196, 1987.
- [28] W. E. Pickett, “Electronic structure of the high-temperature oxide superconductors,” *Reviews of Modern Physics*, vol. 61, p. 433, 1989.
- [29] T. C. Ozawa and S. M. Kauzlarich, “Chemistry of layered d-metal pnictide oxides and their potential as candidates for new superconductors,” *Science and Technology of Advanced Materials*, vol. 9, p. 033003, 2008.

- [30] J. W. Lynn and P. Dai, “Neutron studies of the iron-based family of high T_c magnetic superconductors,” *Physica C*, vol. 469, p. 469, 2009.
- [31] E. Colombier, S. L. Bud’ko, N. Ni, and P. C. Canfield, “Complete pressure-dependent phase diagrams for SrFe_2As_2 and BaFe_2As_2 ,” *Physical Review B*, vol. 79, p. 224518, 2009.
- [32] J.-H. Chu, J. G. Analytis, C. Kucharczyk, and I. R. Fisher, “Determination of the phase diagram of the electron-doped superconductor $\text{BaFe}_{2-x}\text{Co}_x\text{As}_2$,” *Physical Review B*, vol. 79, p. 014506, Jan. 2009.
- [33] K. Kirshenbaum, S. R. Saha, T. Drye, and J. Paglione, “Superconductivity and magnetism in platinum-substituted SrFe_2As_2 single crystals,” *Physical Review B*, vol. 82, p. 144518, 2010.
- [34] P. C. Canfield, S. L. Bud’ko, N. Ni, A. Kreyssig, A. I. Goldman, R. J. McQueeney, M. S. Torikachvili, D. N. Argyriou, G. Luke, and W. Yu, “Structural, magnetic and superconducting phase transitions in CaFe_2As_2 under ambient and applied pressure,” *Physica C*, vol. 469, p. 313, 2009.
- [35] J. Zaanen, “Specific-heat jump at the superconducting transition and the quantum critical nature of the normal state of pnictide superconductors,” *Physical Review B*, vol. 80, p. 212502, 2009.
- [36] C.-T. Chen, C. C. Tsuei, M. B. Ketchen, Z.-A. Ren, and Z. X. Zhao, “Integer and half-integer flux-quantum transitions in a niobium–iron pnictide loop,” *Nature Physics*, vol. 6, pp. 260–264, Apr. 2010.
- [37] X. Zhang, Y. S. Oh, Y. Liu, L. Yan, K. H. Kim, R. L. Greene, and I. Takeuchi, “Observation of the josephson effect in $\text{Pb}/\text{Ba}_{1-x}\text{K}_x\text{Fe}_2\text{As}_2$ single crystal junctions,” *Physical Review Letters*, vol. 102, p. 147002, Apr. 2009.
- [38] C. W. Hicks, T. M. Lippman, M. E. Huber, Z.-A. Ren, J. Yang, Z.-X. Zhao, and K. A. Moler, “Limits on the superconducting order parameter in $\text{NdFeAsO}_{1-x}\text{F}_y$ from scanning SQUID microscopy,” *Journal of the Physical Society of Japan*, vol. 78, p. 013708, Dec. 2008.
- [39] S. R. Saha, N. P. Butch, K. Kirshenbaum, and J. Paglione, “Evolution of bulk superconductivity in SrFe_2As_2 with Ni substitution,” *Physical Review B*, vol. 79, p. 224519, 2009.
- [40] S. Ran, S. L. Bud’ko, D. K. Pratt, A. Kreyssig, M. G. Kim, M. J. Kramer, D. H. Ryan, W. N. Rowan-Weetaluktuk, Y. Furukawa, B. Roy, A. I. Goldman, and P. C. Canfield, “Stabilization of an ambient-pressure collapsed tetragonal phase in CaFe_2As_2 and tuning of the orthorhombic-antiferromagnetic transition temperature by over 70 k via control of nanoscale precipitates,” *Physical Review B*, vol. 83, p. 144517, Apr. 2011.

- [41] Z. Fisk and J. P. Remeika, “Chapter 81: Growth of single crystals from molten metal fluxes,” *Handbook on the Physics and Chemistry of Rare Earths*, vol. 12, p. 53, 1989.
- [42] P. C. Canfield and Z. Fisk, “Growth of single crystals from metallic fluxes,” *Philosophical Magazine B*, vol. 65, p. 1117, 1992.
- [43] V. K. Pecharsky and P. Zavalij, *Fundamentals of Powder Diffraction and Structural Characterization of Materials*. Springer, 2009.
- [44] F. Ronning, T. Klimczuk, E. D. Bauer, H. Volz, and J. D. Thompson, “Synthesis and properties of CaFe_2As_2 single crystals,” *Journal of Physics: Condensed Matter*, vol. 20, p. 322201, Aug. 2008.
- [45] Y. Nakajima, T. Taen, and T. Tamegai, “Possible superconductivity above 25K in single-crystalline co-doped BaFe_2As_2 ,” *Journal of the Physical Society of Japan*, vol. 78, p. 2, 2009.
- [46] S. Bud’ko and P. Canfield, “Specific heat jump at the superconducting transition temperature in $\text{BaFe}_{2-x}\text{Co}_x\text{As}_2$ and $\text{BaFe}_{2-x}\text{Ni}_x\text{As}_2$ single crystals,” *Physical Review B*, vol. 79, p. 220516, 2009.
- [47] Y. Kamihara, T. Watanabe, M. Hirano, and H. Hosono, “Iron-based layered superconductor $\text{La}(\text{O}_{1-x}\text{F}_x)\text{FeAs}$ ($x = 0.05\text{--}0.12$) with $T_c = 26\text{K}$,” *Journal of the American Chemical Society*, vol. 130, p. 3296, 2008.
- [48] M. J. Pitcher, D. R. Parker, P. Adamson, S. J. C. Herkelrath, A. T. Boothroyd, and S. J. Clarke, “Structure and superconductivity of LiFeAs ,” *Chemical Communications*, p. 5918, 2008.
- [49] T. M. McQueen, Q. Huang, V. Ksenofontov, C. Felser, Q. Xu, H. W. Zandbergen, Y. S. Hor, J. Allred, A. J. Williams, D. Qu, J. Checkelsky, N. P. Ong, and R. J. Cava, “Extreme sensitivity of superconductivity to stoichiometry in $\text{Fe}_{1+\delta}\text{Se}$,” *Physical Review B*, vol. 79, p. 014522, 2009.
- [50] X. Zhu, F. Han, G. Mu, P. Cheng, B. Shen, B. Zeng, and H.-H. Wen, “Transition of stoichiometric $\text{Sr}_2\text{VO}_3\text{FeAs}$ to a superconducting state at 37.2 K,” *Physical Review B*, vol. 79, p. 220512, 2009.
- [51] G. Just and P. Paufler, “On the coordination of ThCr_2Si_2 (BaAl_4 -type compounds) within the field of free parameters,” *Journal of Alloys and Compounds*, vol. 232, pp. 1–25, Jan. 1996.
- [52] M. Rotter, M. Tegel, and D. Johrendt, “Superconductivity at 38 K in the iron arsenide $\text{Ba}_{1-x}\text{K}_x\text{Fe}_2\text{As}_2$,” *Physical Review Letters*, vol. 101, p. 107006, 2008.
- [53] K. Sasmal, B. Lv, B. Lorenz, A. M. Guloy, F. Chen, Y. Y. Xue, and C. W. Chu, “Superconducting Fe-based compounds $(\text{A}_{1-x}\text{Sr}_x)\text{Fe}_2\text{As}_2$ with $\text{A}=\text{K}$ and Cs with transition temperatures up to 37 K,” *Physical Review Letters*, vol. 101, p. 107007, 2008.

- [54] G. F. Chen, Z. Li, G. Li, W. Z. Hu, J. Dong, X. D. Zhang, P. Zheng, N. L. Wang, and J. L. Luo, “Superconductivity in hole-doped $(\text{Sr}_{1-x}\text{K}_x)\text{Fe}_2\text{As}_2$,” *Chinese Physics Letters*, vol. 25, p. 3403, 2008.
- [55] J. Gillett, S. D. Das, P. Syers, A. K. T. Ming, J. I. Espeso, C. M. Petrone, and S. E. Sebastian, “Dimensional tuning of the magnetic-structural transition in $\text{A}(\text{Fe}_{1-x}\text{Co}_x)_2\text{As}_2$ ($\text{A}=\text{Sr},\text{Ba}$),” *ArXiv*, p. 1005.1330, 2010.
- [56] A. S. Sefat, R. Jin, M. A. McGuire, B. C. Sales, D. J. Singh, and D. Mandrus, “Superconductivity at 22 K in Co-doped BaFe_2As_2 crystals,” *Physical Review Letters*, vol. 101, p. 117004, 2008.
- [57] N. Ni, M. E. Tillman, J.-Q. Yan, A. Kracher, S. T. Hannahs, S. L. Budko, and P. C. Canfield, “Effects of Co substitution on thermodynamic and transport properties and anisotropic H_{c2} in $\text{Ba}(\text{Fe}_{1-x}\text{Co}_x)_2\text{As}_2$ single crystals,” *Physical Review B*, vol. 78, p. 214515, Dec. 2008.
- [58] A. Leithe-Jasper, W. Schnelle, C. Geibel, and H. Rosner, “Superconducting state in $\text{SrFe}_{2-x}\text{Co}_x\text{As}_2$ by internal doping of the iron arsenide layers,” *Physical Review Letters*, vol. 101, p. 207004, 2008.
- [59] L. J. Li, Y. K. Luo, Q. B. Wang, H. Chen, Z. Ren, Q. Tao, Y. K. Li, X. Lin, M. He, Z. W. Zhu, G. H. Cao, and Z. A. Xu, “Superconductivity induced by Ni doping in BaFe_2As_2 single crystals,” *New Journal of Physics*, vol. 11, p. 025008, 2009.
- [60] N. P. Butch, S. R. Saha, X. H. Zhang, K. Kirshenbaum, R. L. Greene, and J. Paglione, “Effective carrier type and field-dependence of the reduced- T_c superconducting state in $\text{SrFe}_{2-x}\text{Ni}_x\text{As}_2$,” *Physical Review B*, vol. 81, p. 024518, 2010.
- [61] F. Han, X. Zhu, P. Cheng, G. Mu, Y. Jia, L. Fang, Y. Wang, H. Luo, B. Zeng, B. Shen, L. Shan, C. Ren, and H.-H. Wen, “Superconductivity and phase diagrams of the 4d- and 5d-metal-doped iron arsenides $\text{SrFe}_{2x}\text{M}_x\text{As}_2$ ($\text{M}=\text{Rh}, \text{Ir}, \text{Pd}$),” *Physical Review B*, vol. 80, p. 024506, 2009.
- [62] N. Ni, A. Thaler, A. Kracher, J. Q. Yan, S. L. Bud’ko, and P. C. Canfield, “Phase diagrams of $\text{Ba}(\text{Fe}_{1-x}\text{TM}_x)_2\text{As}_2$ ($\text{TM} = \text{Rh}, \text{Pd}$) single crystals,” *Physical Review B*, vol. 80, p. 024511, 2009.
- [63] S. R. Saha, T. Drye, K. Kirshenbaum, N. P. Butch, P. Y. Zavalij, and J. Paglione, “Superconductivity at 23 K in Pt doped BaFe_2As_2 single crystals,” *Journal of Physics: Condensed Matter*, vol. 22, p. 072204, 2010.
- [64] X. Zhu, F. Han, G. Mu, P. Cheng, J. Tang, J. Ju, K. Tanigaki, and H.-H. Wen, “Superconductivity induced by doping platinum in BaFe_2As_2 ,” *Physical Review B*, vol. 81, p. 104525, 2010.

- [65] R. Hoffmann and C. Zheng, “Making and breaking bonds in the solid state: the thorium chromium silicide (ThCr_2Si_2) structure,” *The Journal of Physical Chemistry*, vol. 89, pp. 4175–4181, Sept. 1985.
- [66] S. R. Saha, K. Kirshenbaum, N. P. Butch, J. Paglione, and P. Y. Zavaliy, “Uniform chemical pressure effect in solid solutions $\text{Ba}_{1-x}\text{Sr}_x\text{Fe}_2\text{As}_2$ and $\text{Sr}_{1-x}\text{Ca}_x\text{Fe}_2\text{As}_2$,” *Journal of Physics: Conference Series*, vol. 273, p. 012104, Jan. 2011.
- [67] A. Kreyssig, M. A. Green, Y. Lee, G. D. Samolyuk, P. Zajdel, J. W. Lynn, S. L. Budko, M. S. Torikachvili, N. Ni, S. Nandi, J. B. Leo, S. J. Poulton, D. N. Argyriou, B. N. Harmon, R. J. McQueeney, P. C. Canfield, and A. I. Goldman, “Pressure-induced volume-collapsed tetragonal phase of CaFe_2As_2 as seen via neutron scattering,” *Physical Review B*, vol. 78, p. 184517, Nov. 2008.
- [68] A. I. Goldman, A. Kreyssig, K. Proke, D. K. Pratt, D. N. Argyriou, J. W. Lynn, S. Nandi, S. A. J. Kimber, Y. Chen, Y. B. Lee, G. Samolyuk, J. B. Leo, S. J. Poulton, S. L. Budko, N. Ni, P. C. Canfield, B. N. Harmon, and R. J. McQueeney, “Lattice collapse and quenching of magnetism in CaFe_2As_2 under pressure: A single-crystal neutron and x-ray diffraction investigation,” *Physical Review B*, vol. 79, p. 024513, Jan. 2009.
- [69] M. S. Torikachvili, S. L. Budko, N. Ni, and P. C. Canfield, “Pressure induced superconductivity in CaFe_2As_2 ,” *Physical Review Letters*, vol. 101, p. 057006, July 2008.
- [70] T. Park, E. Park, H. Lee, T. Klimczuk, E. D. Bauer, F. Ronning, and J. D. Thompson, “Pressure-induced superconductivity in CaFe_2As_2 ,” *Journal of Physics: Condensed Matter*, vol. 20, p. 322204, Aug. 2008.
- [71] K. Proke, A. Kreyssig, B. Ouladdiaf, D. K. Pratt, N. Ni, S. L. Budko, P. C. Canfield, R. J. McQueeney, D. N. Argyriou, and A. I. Goldman, “Evidence from neutron diffraction for superconductivity in the stabilized tetragonal phase of CaFe_2As_2 under uniaxial pressure,” *Physical Review B*, vol. 81, p. 180506, May 2010.
- [72] W. Yu, A. A. Aczel, T. J. Williams, S. L. Budko, N. Ni, P. C. Canfield, and G. M. Luke, “Absence of superconductivity in single-phase CaFe_2As_2 under hydrostatic pressure,” *Physical Review B*, vol. 79, p. 020511, Jan. 2009.
- [73] S. Kasahara, T. Shibauchi, K. Hashimoto, Y. Nakai, H. Ikeda, T. Terashima, and Y. Matsuda, “Abrupt recovery of fermi-liquid transport following the collapse of the c -axis in $\text{CaFe}_2(\text{As}_{1-x}\text{P}_x)_2$ single crystals,” *Physical Review B*, vol. 83, p. 060505, Feb. 2011.

- [74] T. Yildirim, “Strong coupling of the Fe-spin state and the As-As hybridization in iron-pnictide superconductors from first-principle calculations,” *Physical Review Letters*, vol. 102, p. 037003, Jan. 2009.
- [75] J. Paglione, “Structural tuning of superconductivity and magnetism in intermetallic iron-pnictide materials,” in *Bulletin of the American Physical Society*, vol. Volume 56, Number 1, American Physical Society, Mar. 2011.
- [76] R. D. Shannon, “Revised effective ionic radii and systematic studies of interatomic distances in halides and chalcogenides,” *Acta Crystallographica Section A*, vol. 32, pp. 751–767, Sept. 1976.
- [77] S. R. Saha, N. P. Butch, K. Kirshenbaum, J. Paglione, and P. Y. Zavalij, “Superconducting and ferromagnetic phases induced by lattice distortions in stoichiometric SrFe_2As_2 single crystals,” *Physical Review Letters*, vol. 103, p. 037005, July 2009.
- [78] Y. Muraba, S. Matsuishi, S.-W. Kim, T. Atou, O. Fukunaga, and H. Hosono, “High-pressure synthesis of the indirectly electron-doped iron pnictide superconductor $\text{Sr}_{1-x}\text{La}_x\text{Fe}_2\text{As}_2$ with maximum $T_c=22$ K,” *Physical Review B*, vol. 82, p. 180512, Nov. 2010.
- [79] D. R. Lide, *CRC handbook of chemistry and physics: a ready-reference book of chemical and physical data : 2007-2008*. Boca Raton; London; New York: CRC Press, 2008.
- [80] D. Das, T. Jacobs, and L. J. Barbour, “Exceptionally large positive and negative anisotropic thermal expansion of an organic crystalline material,” *Nature Materials*, vol. 9, pp. 36–39, Jan. 2010.
- [81] A. I. Goldman, D. N. Argyriou, B. Ouladdiaf, T. Chatterji, A. Kreyssig, S. Nandi, N. Ni, S. L. Budko, P. C. Canfield, and R. J. McQueeney, “Lattice and magnetic instabilities in CaFe_2As_2 : a single-crystal neutron diffraction study,” *Physical Review B*, vol. 78, p. 100506, Sept. 2008.
- [82] C. Huhnt, G. Michels, M. Roepke, W. Schlabitz, A. Wurth, D. Johrendt, and A. Mewis, “First-order phase transitions in the ThCr_2Si_2 -type phosphides ARh_2P_2 ($A = \text{Sr}, \text{Eu}$),” *Physica B: Condensed Matter*, vol. 240, pp. 26–37, Sept. 1997.
- [83] S. Kawasaki, T. Tabuchi, X. F. Wang, X. H. Chen, and G.-q. Zheng, “Pressure-induced unconventional superconductivity near a quantum critical point in CaFe_2As_2 ,” *Superconductor Science and Technology*, vol. 23, p. 054004, May 2010.
- [84] S.-H. Baek, N. J. Curro, T. Klimczuk, E. D. Bauer, F. Ronning, and J. D. Thompson, “First-order magnetic transition in single-crystalline CaFe_2As_2 detected by ^{75}As nuclear magnetic resonance,” *Physical Review B*, vol. 79, p. 052504, Feb. 2009.

- [85] W. Ji, X.-W. Yan, and Z.-Y. Lu, “Pressure- and temperature-induced structural phase transitions of CaFe_2As_2 and BaFe_2As_2 studied in the hunds rule correlation picture,” *Physical Review B*, vol. 83, p. 132504, Apr. 2011.
- [86] D. K. Pratt, Y. Zhao, S. A. J. Kimber, A. Hiess, D. N. Argyriou, C. Broholm, A. Kreyssig, S. Nandi, S. L. Budko, N. Ni, P. C. Canfield, R. J. McQueeney, and A. I. Goldman, “Suppression of antiferromagnetic spin fluctuations in the collapsed phase of CaFe_2As_2 ,” *Physical Review B*, vol. 79, p. 060510, Feb. 2009.
- [87] N. Ni, S. Nandi, A. Kreyssig, A. I. Goldman, E. D. Mun, S. L. Budko, and P. C. Canfield, “First-order structural phase transition in CaFe_2As_2 ,” *Physical Review B*, vol. 78, p. 014523, July 2008.
- [88] P. Cheng, B. Shen, G. Mu, X. Zhu, F. Han, B. Zeng, and H.-H. Wen, “High- T_c superconductivity induced by doping rare-earth elements into CaFeAsF ,” *EPL (Europhysics Letters)*, vol. 85, p. 67003, Mar. 2009.
- [89] K. Kirshenbaum, S. R. Saha, S. Ziemak, T. Drye, and J. Paglione, “Universal pair-breaking in transition metal-substituted iron-pnictide superconductors,” *Physical Review B*, vol. 86, p. 140505(R), 2012.
- [90] L. E. Klintberg, S. K. Goh, S. Kasahara, Y. Nakai, K. Ishida, M. Sutherland, T. Shibauchi, Y. Matsuda, and T. Terashima, “Chemical pressure and physical pressure in $\text{BaFe}_2(\text{As}_{1-x}\text{P}_x)_2$,” *Journal of the Physical Society of Japan*, vol. 79, p. 123706, Dec. 2010.
- [91] S. A. J. Kimber, A. Kreyssig, Y.-Z. Zhang, H. O. Jeschke, R. Valent, F. Yokaichiya, E. Colombier, J. Yan, T. C. Hansen, T. Chatterji, R. J. McQueeney, P. C. Canfield, A. I. Goldman, and D. N. Argyriou, “Similarities between structural distortions under pressure and chemical doping in superconducting BaFe_2As_2 ,” *Nature Materials*, vol. 8, pp. 471–475, June 2009.
- [92] M. D. Johannes, I. I. Mazin, and D. S. Parker, “Effect of doping and pressure on magnetism and lattice structure of iron-based superconductors,” *Physical Review B*, vol. 82, p. 024527, July 2010.
- [93] H. Luetkens, H.-H. Klauss, M. Kraken, F. J. Litterst, T. Dellmann, R. Klingeler, C. Hess, R. Khasanov, A. Amato, C. Baines, M. Kosmala, O. J. Schumann, M. Braden, J. Hamann-Borrero, N. Leps, A. Kondrat, G. Behr, J. Werner, and B. Bchner, “The electronic phase diagram of the $\text{LaO}_{1-x}\text{F}_x\text{FeAs}$ superconductor,” *Nature Materials*, vol. 8, pp. 305–309, Apr. 2009.
- [94] J. Zhao, Q. Huang, C. de la Cruz, S. Li, J. W. Lynn, Y. Chen, M. A. Green, G. F. Chen, G. Li, Z. Li, J. L. Luo, N. L. Wang, and P. Dai, “Structural and magnetic phase diagram of $\text{CeFeAsO}_{1-x}\text{F}_x$ and its relation to high-temperature superconductivity,” *Nature Materials*, vol. 7, pp. 953–959, Dec. 2008.

- [95] F. Y. Wei, B. Lv, L. Z. Deng, J. K. Meen, Y. Y. Xue, and C. W. Chu, “Why is the superconducting T_c so high in rare-earth-doped CaFe_2As_2 ?,” *arXiv:1309.0034 [cond-mat]*, Aug. 2013.
- [96] D. Kasinathan, A. Ormeci, K. Koch, U. Burkhardt, W. Schnelle, A. Leithe-Jasper, and H. Rosner, “ AFe_2As_2 ($A = \text{Ca, Sr, Ba, Eu}$) and $\text{SrFe}_{2-x}\text{TM}_x\text{As}_2$ ($\text{TM} = \text{Mn, Co, Ni}$): crystal structure, charge doping, magnetism and superconductivity,” *New Journal of Physics*, vol. 11, p. 025023, Feb. 2009.
- [97] J.-Q. Yan, A. Kreyssig, S. Nandi, N. Ni, S. L. Budko, A. Kracher, R. J. McQueeney, R. W. McCallum, T. A. Lograsso, A. I. Goldman, and P. C. Canfield, “Structural transition and anisotropic properties of single-crystalline SrFe_2As_2 ,” *Physical Review B*, vol. 78, p. 024516, July 2008.
- [98] F. Ronning, N. Kurita, E. D. Bauer, B. L. Scott, T. Park, T. Klimczuk, R. Movshovich, and J. D. Thompson, “The first order phase transition and superconductivity in $\text{BaFe}_{2-x}\text{Ni}_x\text{As}_2$ single crystals,” *Journal of Physics: Condensed Matter*, vol. 20, p. 342203, Aug. 2008.
- [99] A. Subedi and D. J. Singh, “Density functional study of BaNi_2As_2 : electronic structure, phonons, and electron-phonon superconductivity,” *Physical Review B*, vol. 78, p. 132511, Oct. 2008.
- [100] Z. G. Chen, G. Xu, W. Z. Hu, X. D. Zhang, P. Zheng, G. F. Chen, J. L. Luo, Z. Fang, and N. L. Wang, “Origin of the structural phase transition in BaNi_2As_2 at 130 K: A combined study of optical spectroscopy and band structure calculations,” *Physical Review B*, vol. 80, p. 094506, Sept. 2009.
- [101] T. Park, H. Lee, E. D. Bauer, J. D. Thompson, and F. Ronning, “Pressure dependence of BaNi_2As_2 ,” *Journal of Physics: Conference Series*, vol. 200, p. 012155, Jan. 2010.
- [102] K. Kudo, M. Takasuga, Y. Okamoto, Z. Hiroi, and M. Nohara, “Giant phonon softening and enhancement of superconductivity by phosphorus doping of BaNi_2As_2 ,” *Physical Review Letters*, vol. 109, p. 097002, Aug. 2012.
- [103] I. R. Shein and A. L. Ivanovskii, “Electronic and structural properties of low-temperature superconductors and ternary pnictides ANi_2Pn_2 ($A=\text{Sr,Ba}$ and $\text{Pn}=\text{P,As}$),” *Physical Review B*, vol. 79, p. 054510, Feb. 2009.
- [104] E. D. Bauer, F. Ronning, B. L. Scott, and J. D. Thompson, “Superconductivity in SrNi_2As_2 single crystals,” *Physical Review B*, vol. 78, p. 172504, Nov. 2008.
- [105] P. C. Canfield, S. L. Budko, N. Ni, J. Q. Yan, and A. Kracher, “Decoupling of the superconducting and magnetic/structural phase transitions in electron-doped BaFe_2As_2 ,” *Physical Review B*, vol. 80, p. 060501(R), 2009.

- [106] H. Xiao, T. Hu, A. P. Dioguardi, N. apRoberts-Warren, A. C. Shockley, J. Crocker, D. M. Nisson, Z. Viskadourakis, X. Tee, I. Radulov, C. C. Almasan, N. J. Curro, and C. Panagopoulos, “Evidence for filamentary superconductivity nucleated at antiphase domain walls in antiferromagnetic CaFe_2As_2 ,” *Physical Review B*, vol. 85, p. 024530, Jan. 2012.
- [107] R. Zhi-An, L. Wei, Y. Jie, Y. Wei, S. Xiao-Li, Zheng-Cai, C. Guang-Can, D. Xiao-Li, S. Li-Ling, Z. Fang, and Z. Zhong-Xian, “Superconductivity at 55 K in iron-based F-doped layered quaternary compound $\text{Sm}[\text{O}_{1-x}\text{F}_x]\text{FeAs}$,” *Chinese Physics Letters*, vol. 25, pp. 2215–2216, June 2008.
- [108] K. Gofryk, M. Pan, C. Cantoni, B. Sapiro, J. E. Mitchell, and A. S. Sefat, “Local inhomogeneity and filamentary superconductivity in pr-doped CaFe_2As_2 ,” *Physical Review Letters*, vol. 112, p. 047005, Jan. 2014.
- [109] B. Lv, L. Deng, M. Gooch, F. Wei, Y. Sun, J. K. Meen, Y.-Y. Xue, B. Lorenz, and C.-W. Chu, “Unusual superconducting state at 49 K in electron-doped CaFe_2As_2 at ambient pressure,” *Proceedings of the National Academy of Sciences*, vol. 108, pp. 15705–15709, Sept. 2011. PMID: 21911404.
- [110] Z. Gao, Y. Qi, L. Wang, D. Wang, X. Zhang, C. Yao, C. Wang, and Y. Ma, “Synthesis and properties of La-doped CaFe_2As_2 single crystals with $T_c=42.7$ K,” *EPL (Europhysics Letters)*, vol. 95, p. 67002, Sept. 2011.
- [111] I. Zeljkovic, D. Huang, C.-L. Song, B. Lv, C.-W. Chu, and J. E. Hoffman, “Nanoscale surface element identification and dopant homogeneity in the high- T_c superconductor $\text{Pr}_x\text{Ca}_{1-x}\text{Fe}_2\text{As}_2$,” *Physical Review B*, vol. 87, p. 201108, May 2013.
- [112] E. Samuel Reich, “Interface superconductivity found in single crystal,” *Nature*, vol. 501, pp. 474–475, Sept. 2013.
- [113] S. Lee, J. Jiang, J. D. Weiss, C. M. Folkman, C. W. Bark, C. Tarantini, A. Xu, D. Abaimov, A. Polyanskii, C. T. Nelson, Y. Zhang, S. H. Baek, H. W. Jang, A. Yamamoto, F. Kametani, X. Q. Pan, E. E. Hellstrom, A. Gurevich, C. B. Eom, and D. C. Larbalestier, “Weak-link behavior of grain boundaries in superconducting $\text{Ba}(\text{Fe}_{1-x}\text{Co}_x)_2\text{As}_2$ bicrystals,” *Applied Physics Letters*, vol. 95, p. 212505, Nov. 2009.
- [114] A. Yamamoto, J. Jiang, C. Tarantini, N. Craig, A. A. Polyanskii, F. Kametani, F. Hunte, J. Jaroszynski, E. E. Hellstrom, D. C. Larbalestier, R. Jin, A. S. Sefat, M. A. McGuire, B. C. Sales, D. K. Christen, and D. Mandrus, “Evidence for electromagnetic granularity in the polycrystalline iron-based superconductor $\text{LaO}_{0.89}\text{F}_{0.11}\text{FeAs}$,” *Applied Physics Letters*, vol. 92, p. 252501, June 2008.
- [115] Y. Ding, Y. Sun, X. D. Wang, H. C. Wang, Z. X. Shi, Z. A. Ren, J. Yang, and W. Lu, “Comparative study of type-II superconducting properties in polycrystalline $\text{NdFeAsO}_{0.88}\text{F}_{0.12}$ prepared by different methods,” *Physica C: Superconductivity*, vol. 470, pp. 2051–2056, Dec. 2010.

- [116] A. Yamamoto, A. A. Polyanskii, J. Jiang, F. Kametani, C. Tarantini, F. Hunte, J. Jaroszynski, E. E. Hellstrom, P. J. Lee, A. Gurevich, D. C. Larbalestier, Z. A. Ren, J. Yang, X. L. Dong, W. Lu, and Z. X. Zhao, “Evidence for two distinct scales of current flow in polycrystalline Sm and Nd iron oxypnictides,” *Superconductor Science and Technology*, vol. 21, p. 095008, Sept. 2008.
- [117] Y. Sun, Y. Ding, J. C. Zhuang, L. J. Cui, X. P. Yuan, Z. X. Shi, and Z. A. Ren, “An anomalous tail effect in the resistivity transition and weak-link behavior of superconducting NdFeAsO_{0.88}F_{0.12},” *Superconductor Science and Technology*, vol. 24, p. 085011, Aug. 2011.
- [118] A. Yamamoto, J. Jiang, F. Kametani, A. Polyanskii, E. Hellstrom, D. Larbalestier, A. Martinelli, A. Palenzona, M. Tropeano, and M. Putti, “Evidence for electromagnetic granularity in polycrystalline sm1111 iron-pnictides with enhanced phase purity,” *Superconductor Science and Technology*, vol. 24, p. 045010, Apr. 2011.
- [119] T. Tamegai, Q. P. Ding, T. Ishibashi, and Y. Nakajima, “Superconducting properties of Ca_{1-x}RE_xFe₂As₂ (RE: Rare earths),” *Physica C: Superconductivity*, vol. 484, pp. 31–34, Jan. 2013.
- [120] S. K. Goh, L. E. Klintberg, J. M. Silver, F. M. Grosche, S. R. Saha, T. Drye, J. Paglione, and M. Sutherland, “Enhancement of the superconducting transition temperature under pressure in rare-earth doped Ca_{1-x}Pr_xFe₂As₂ (x=0.27),” *arXiv:1107.0689 [cond-mat]*, July 2011.
- [121] H. Gretarsson, S. R. Saha, T. Drye, J. Paglione, J. Kim, D. Casa, T. Gog, W. Wu, S. R. Julian, and Y.-J. Kim, “Spin-state transition in the Fe pnictides,” *Physical Review Letters*, vol. 110, p. 047003, Jan. 2013.
- [122] W. K. L. Wang. Presentation at University of Maryland, May 2014.
- [123] K. Kudo, K. Iba, M. Takasuga, Y. Kitahama, J.-i. Matsumura, M. Danura, Y. Nogami, and M. Nohara, “Emergence of superconductivity at 45 K by lanthanum and phosphorus co-doping of CaFe₂As₂,” *Scientific Reports*, vol. 3, Mar. 2013.